

**Fabrication and characterization of SiO₂
microcantilevers for Relative Humidity sensing**

By

BALASUBRAMANIAN S

Enrolment No: PHYS 02 2015 04 018

**Indira Gandhi Centre for Atomic Research, Kalpakkam,
Tamil Nadu, India, 603102**

*A thesis submitted to the
Board of Studies in Physical Sciences*

*In partial fulfillment of requirements
for the Degree of*

DOCTOR OF PHILOSOPHY

of

HOMI BHABHA NATIONAL INSTITUTE



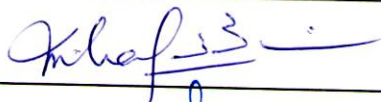
September 2020

Homi Bhabha National Institute

Recommendations of the Viva Voce Committee

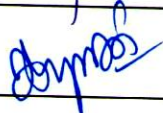
As members of the Viva Voce Committee, we certify that we have read the dissertation prepared by Balasubramanian. S entitled, "Fabrication and characterization of SiO₂ microcantilevers for Relative Humidity sensing" and recommend that it may be accepted as fulfilling the thesis requirement for the award of Degree of Doctor of Philosophy.

Chairman – Dr. M. Kamruddin



Date 15/12/2020

Guide / Convener – Dr. K. Prabakar



Date 15/12/20

Examiner - Dr. Isabelle Dufour

By Vc. For. P. S. J. (Dean, PS)

Date 15/12/2020

Member 1- Dr. T. R. Ravindran



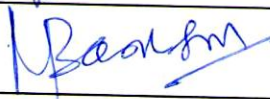
Date 15/12/2020

Member 2- Dr. V. Jayaraman



Date 15/12/2020

Technology Advisor- Sri R. Baskaran



Date 15/12/2020.

Final approval and acceptance of this thesis is contingent upon the candidate's submission of the final copies of the thesis to HBNI.

I/We hereby certify that I/we have read this thesis prepared under my/our direction and recommend that it may be accepted as fulfilling the thesis requirement.

Date: 15/12/20

Place: Kalpak Kam.



Dr. K. Prabakar

Guide

Homi Bhabha National Institute

Recommendations of the Viva Voce Committee

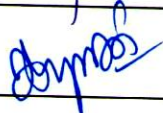
As members of the Viva Voce Committee, we certify that we have read the dissertation prepared by Balasubramanian. S entitled, "Fabrication and characterization of SiO₂ microcantilevers for Relative Humidity sensing" and recommend that it may be accepted as fulfilling the thesis requirement for the award of Degree of Doctor of Philosophy.

Chairman – Dr. M. Kamruddin



Date 15/12/2020

Guide / Convener – Dr. K. Prabakar



Date 15/12/20

Examiner - Dr. Isabelle Dufour

By Vc. For. P. K. J. (Dean, PS)

Date 15/12/2020

Member 1- Dr. T. R. Ravindran



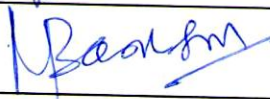
Date 15/12/2020

Member 2- Dr. V. Jayaraman



Date 15/12/2020

Technology Advisor- Sri R. Baskaran



Date 15/12/2020.

Final approval and acceptance of this thesis is contingent upon the candidate's submission of the final copies of the thesis to HBNI.

I/We hereby certify that I/we have read this thesis prepared under my/our direction and recommend that it may be accepted as fulfilling the thesis requirement.

Date: 15/12/20

Place: Kalpak Kam.



Dr. K. Prabakar

Guide

STATEMENT BY AUTHOR

This dissertation has been submitted in partial fulfillment of requirements for an advanced degree at Homi Bhabha National Institute (HBNI) and is deposited in the Library to be made available to borrowers under rules of the HBNI.

Brief quotations from this dissertation are allowable without special permission, provided that accurate acknowledgement of source is made. Requests for permission for extended quotation from or reproduction of this manuscript in whole or in part may be granted by the Competent Authority of HBNI when in his or her judgment the proposed use of the material is in the interests of scholarship. In all other instances, however, permission must be obtained from the author.


Balasubramanian. S

DECLARATION

I, hereby declare that the investigation presented in the thesis has been carried out by me. The work is original and has not been submitted earlier as a whole or in part for a degree / diploma at this or any other Institution / University.

S Balasubramanian

Balasubramanian. S

List of Publications arising from the thesis

Journal

1. “Ultrahigh sensitive and ultrafast relative humidity sensing using surface enhanced SiO₂ microcantilevers”, **S. Balasubramanian**, S. R. Polaki and K. Prabakar, *Smart Mater. Struct.*, **2020**, 29, 095006 (13 pp).
2. “Effect of biaxial curvature on the resonance frequency of uncoated microcantilevers”, **S. Balasubramanian**, K. Prabakar, Aditi, Ravindra Mukhiya, and Tripura Sundari, *Sensors and Actuators A: Physical*, **2020**, 304, 111857 (8 pp).
3. “Fabrication and characterization of SiO₂ microcantilevers by direct laser writing and wet chemical etching methods for relative humidity sensing”, **S. Balasubramanian** and K. Prabakar, *Microelectronic Engineering*, **2019**, 212, 61–69.
4. “Effect of high-temperature annealing on the mean and gradient residual stress evolution in SiO₂ microcantilevers”, **S. Balasubramanian** and K. Prabakar, **(Manuscript under preparation)**.
5. “Role of surface micro-patterns on the static and dynamic characteristics of SiO₂ microcantilevers”, **S. Balasubramanian** and K. Prabakar, **(Manuscript under preparation)**.

Conference Proceedings

1. “Effect of annealing induced residual stress on the resonance frequency of SiO₂ microcantilevers”, **S. Balasubramanian**, K. Prabakar and S. Tripura Sundari, *AIP Conference Proceedings*, **2018**, 1951, 030018.

Conference Presentations

1. “Surface enhanced microcantilever for ultrasensitive humidity sensing”, **S. Balasubramanian**, K. Prabakar and S.R. Polaki, *International Conference on Nano Science and Technology (ICONSAT - 2020)*, 5 - 7 March 2020, S. N. Bose National Centre for Basic Sciences, Kolkata, India **(Poster Presentation – BEST POSTER Award)**.

2. “Humidity sensing using uncoated micro-patterned SiO₂ microcantilevers”, **S. Balasubramanian** and K. Prabakar, *4th International Conference on Emerging Electronics (IEEE ICEE)*, 16 – 19 Dec 2018, Indian Institute of Science, Bangalore, India (**Poster Presentation**).
3. “An effective method to avoid stiction in SiO₂ microcantilevers released by wet chemical etching technique”, **S. Balasubramanian** and K. Prabakar, *Research Scholars Meet on Material Science and Engineering of Nuclear Materials (RSM-MSENM)*, 7-9 May 2018, Indira Gandhi Centre for Atomic Research, Kalpakkam, India (**Oral Presentation**).
4. “Effect of annealing induced residual stress on the resonance frequency of SiO₂ microcantilevers”, **S. Balasubramanian**, K. Prabakar and S. Tripura Sundari, *National Conference on Thermophysical properties (NCTP)*, 06-08 Nov 2017, Indira Gandhi Centre for Atomic Research, Kalpakkam, India (**Poster Presentation**).

Publications not included in the thesis

1. “Residual stress in underlying silicon at the fixed end of SiO₂ microcantilevers — A micro-Raman study”, K. Prabakar, M. Raghuramaiah, **S. Balasubramanian**, Sagnik Midhya, P. Avinash and Tripura Sundari, *Modern Physics Letters B*, **2019**, Vol. 33 (1), 1850419 (9 pp).
2. “Effect of residual stress induced curvature on the stiffness of SiO₂ microcantilevers”, K. Prabakar and **S. Balasubramanian**, *10th ISSS National Conference on micro and smart systems (NCMSS)*, 21 – 23 Oct 2019, Nitte Mahalinga Adyanthaya Memorial Institute of Technology, Nitte, Karnataka, India.
3. “Photostriction in Si microcantilevers: Laser Power and Position Dependence”, M. Raghuramaiah, **S. Balasubramanian**, and K. Prabakar, *DAE – BRNS National Laser Symposium (NLS - 25)*, 20 - 23 Dec 2016, KIIT University, Bhubaneswar.


Balasubramanian. S

*Dedicated to the Almighty, my
parents, my wife and all my teachers*

ACKNOWLEDGEMENTS

I would like to thank all the people who have been instrumental in shaping this thesis to completion and help me to evolve as a researcher. In the first place, I would like to express my deep sense of gratitude to my thesis supervisor **Dr. K. Prabakar**, for his untiring support and constant encouragement, both academically and personally, throughout the tenure of my thesis works. I admire his utmost patience in correcting the manuscripts and I truly enjoyed the freedom of research given in the lab. The thesis would not have been in its present shape without his constant support.

Besides my advisor, I am also thankful to my Doctoral Committee (DC) members, **Dr. M. Kamruddin** (Chairman), **Dr. T. R. Ravindran**, **Dr. V. Jayaraman** and **Sri R. Baskaran**, and ex-DC chairman **Dr. A. K. Tyagi** for the fruitful discussions, constructive criticisms, insightful comments and constant encouragement which helped me move forward and widen my research from various perspectives.

I would like to thank my research collaborators **Dr. Ravindra Mukhiya** and **Dr. Aditi** from Central Electronics Engineering Research Institute (CSIR-CEERI), Pilani, Rajasthan for Laser Doppler Vibrometry measurements and scientific inputs. I am thankful to **Dr. S. R. Polaki**, and **Dr. R. Ramaseshan** and **Dr. Padmalochan Panda** from SND, IGCAR for FESEM, and Dektak profilometry measurements. I would also like to thank my senior **Mr. Anil Kumar Behera** for helping me in annealing studies. I also thank **Dr. Nitya Ravindran** for providing crucibles and **Dr. P. Mano Ravi** for helping in RH chamber fabrication.

My sincere thanks to all the members of Electronics and Instrumentation section (EIS), **Dr. S. Tripura Sundari**, **Mr. M. Raghuramaiah**, **Mrs. O. K. Sheela**, **Mr. Venkateswara Reddy Karrevula** and past EIS members **Dr. J. Jayapandian**, **Mrs.**

Usharani, Dr. Manoj Kumar Parida, and Dr. G. Prasanna for their constant support and encouragement. I always enjoyed the friendly atmosphere and personal bonding among all the section members. I also thank all the project students, **Mr. Stav Haldar, Ms. Varsha, Ms. Poorani, Mr. Sumit Bansal and Ms. Subhashree**. I would like to express my sincere thanks to **Dr. S. Tripura Sundari, Mr. Raghuramaiah and Mr. Venkateswara Reddy** for critically going through and providing valuable suggestions to improve my thesis.

I am privileged to thank **Dr. A. K. Bhaduri**, Director, IGCAR and **Dr. S. A. V. Satya Murthy** (former Director, IGCAR) for providing an opportunity to carry out my research at IGCAR. I would also like to thank **Dr. Shaju K. Albert**, Director, MSG & MMG and **Dr. G. Amarendra** (former Director, MSG & MMG), **Sri. M. P. Janawadkar** (former Director, MSG) for their constant support and encouragement. I thank **Dr. R. Rajaraman**, Dean, Physical Sciences, **Dr. N. V. Chandra Shekar** and **Dr. B. V. R. Tata** (former Deans, Physical Sciences) for their constant support in all my academic endeavors at IGCAR. I also thank the IGCAR management for providing the accommodation and for all the other help and support during the tenure of my thesis. I sincerely thank the **Department of Atomic Energy (DAE)**, Government of India for providing fellowship.

I thank all my seniors **Dr. Karthickeyan, Dr. Srinivasan, Dr. Lakshmanan, Dr. Irshad, Dr. Radhikesh, Dr. Raghavendra, Dr. Nilakantha Meher, Dr. Vairavel,** and **Mr. Sivakumar** for creating a friendly environment. I thank all my batch mates **Reshmi Mohan, Dhilipan, Rajitha, Velraj, Akshaya Devi and Jakathamani** for making the stay at IGCAR and JRF enclave cheerful. I am deeply indebted to **Mrs. Reshmi Mohan**, my best friend, for her friendly nature, love and affection, and for

being the constant source of encouragement during the ups and downs of my life. I would also like to thank all my juniors and other friends at JRF enclave for creating a conducive environment during my stay at JRF enclave. I take this opportunity to thank my close friend **Mrs. Anu Priya** for being a constant source of encouragement from my school days.

I thank all the members of **JRF Enclave Residence committee (JRC)** for the collective role they played in representing our issues to higher authorities. I also thank all the players of **Intra Enclave Cricket league (IECL)**, **Enclave Badminton League** and **Team MSG in Interlab Cricket Tournament** for providing the most memorable and entertaining moments during my stay at IGCAR.

Words would not be sufficient to express my heartfelt gratitude to my beloved parents **Mr. B. Srinivasan** and **Mrs. S. Gayathri**, for their unconditional love, care and affection. It is because of the understanding and confidence they had in me I could focus on my research endeavors. I always appreciate and acknowledge the love and affection shown by my brother **Mr. S. Sankaran**, who guided me to take up science as my career. I thank my sister-in-law **Mrs. S. Divya** for her joyful and friendly nature. I thank **Ms. S. Mathangi** and **Ms. B. Muthulakshmi** for their unconditional love towards me. I take this opportunity to thank **Shri. A. V. Raghuprasad**, former Mridangam and Painting teacher at Kalakshetra and former Graphic artist at Doordarshan, for molding my personality and for teaching me the art of Mridangam. I would like to thank all my teachers including my music teachers **Shri A. S. Murali**, **Ms. A. P. Komala**, etc. for playing significant role in my life. It will be incomplete without asserting the role of my wife **V. Sruthi** whose love, understanding and patience made me overcome the difficult situations and made this thesis possible.

CONTENTS

| | Page No. |
|---|---------------------|
| THESIS ABSTRACT | xiv |
| LIST OF FIGURES | xvii |
| LIST OF TABLES | xxvii |
| LIST OF SYMBOLS | xxviii |
| LIST OF ABBREVIATIONS | xxxix |
| CHAPTER 1 INTRODUCTION TO MICROCANTILEVERS | 1 |
| 1.1. Introduction to MEMS | 1 |
| 1.2. Introduction to microcantilever (MC) based sensors | 4 |
| 1.2.1. Modes of operation | 6 |
| 1.2.2. Materials and microfabrication | 7 |
| 1.2.3. Excitation and read-out methods | 9 |
| 1.2.4. Microcantilever theory | 11 |
| 1.2.4.1. Stoney's equation | 11 |
| 1.2.4.2. Expression for resonance frequency of MCs | 14 |
| 1.2.4.3. Energy dissipation in MCs - Quality Factor | 16 |
| 1.3. Brief literature survey on SiO ₂ Microcantilevers | 18 |
| 1.4. Influence of functionalization and surface modifications on MC response | 19 |
| 1.5. Motivation and Objectives of the present thesis | 23 |
| 1.6. References | 26 |
| CHAPTER 2 EXPERIMENTAL METHODS | 37 |
| 2.1. Direct Laser Writer | 37 |
| 2.2. Chemical wet bench | 40 |
| 2.3. 3D optical microscope | 41 |
| 2.4. Nano Vibration Analyzer | 42 |
| 2.5. Laser Doppler Vibrometer | 44 |

| | | |
|------------------|--|-----------|
| 2.6. | Atomic Force Microscopy (AFM) | 46 |
| 2.7. | Finite Element Modeling (FEM) simulations | 47 |
| 2.8. | Estimation of mean and gradient residual stress of films from MC bending | 50 |
| 2.9. | Annealing experiments on released SiO ₂ MCs | 52 |
| 2.10. | Experimental setup for RH sensing | 53 |
| 2.10.1. | Fabrication of mini air-tight chamber | 53 |
| 2.10.2. | Resonance frequency measurements | 54 |
| 2.10.3. | Setup for breath monitoring studies | 56 |
| 2.11. | References | 57 |
| CHAPTER 3 | FABRICATION AND CHARACTERIZATION OF SiO₂ MICROCANTILEVERS | 59 |
| 3.1. | Introduction | 59 |
| 3.2. | SiO ₂ microcantilever fabrication steps | 62 |
| 3.2.1. | MC orientation with respect to Si | 66 |
| 3.2.2. | Laser dose optimization | 67 |
| 3.2.3. | Photoresist post baking temperature and time optimization | 69 |
| 3.2.4. | Effective method to avoid ‘stiction’ during wet release of SiO ₂ MCs | 72 |
| 3.3. | Fabrication of surface micro-patterned SiO ₂ MCs | 73 |
| 3.4. | Characterization of SiO ₂ MCs | 76 |
| 3.4.1. | Curvature measurements using 3D optical microscope | 76 |
| 3.4.2. | Resonance frequency measurements using nano vibration analyzer | 79 |
| 3.5. | Summary | 85 |
| 3.6. | References | 86 |
| CHAPTER 4 | EFFECT OF BIAXIAL CURVATURE ON THE RESONANCE FREQUENCY AND HIGH-TEMPERATURE ANNEALING ON THE BENDING PROPERTIES OF MICROCANTILEVERS | 91 |
| 4.1. | Effect of biaxial curvature on the resonance frequency of SiO ₂ MCs | 92 |
| 4.1.1. | Introduction | 92 |
| 4.1.2. | Results and discussion | 94 |
| 4.1.3. | Role of biaxial curvature on the resonance frequency of MCs | 98 |

| | | |
|------------------|--|------------|
| 4.1.4. | Comparison with previously reported experimental and theoretical studies | 101 |
| 4.2. | Effect of high-temperature annealing on the bending properties of SiO ₂ MCs | 108 |
| 4.2.1. | Introduction | 108 |
| 4.2.2. | Results and Discussion | 109 |
| 4.2.2.1. | Effect of annealing temperature | 109 |
| 4.2.2.2. | Effect of annealing environment | 111 |
| 4.2.2.3. | Effect of MC length | 112 |
| 4.2.2.4. | Effect of annealing on the resonance frequency of MCs | 114 |
| 4.3. | Summary | 116 |
| 4.4. | References | 117 |
| CHAPTER 5 | RELATIVE HUMIDITY SENSING STUDIES USING SiO₂ MICROCANTILEVERS | 123 |
| 5.1. | Introduction | 123 |
| 5.2. | RH sensing using as-fabricated SiO ₂ MCs | 127 |
| 5.2.1. | Sensitivity, Resolution and Hysteresis | 127 |
| 5.3. | RH sensing experiments using micro-patterned SiO ₂ MCs | 130 |
| 5.3.1. | Sensitivity | 131 |
| 5.3.2. | Response/recovery times | 138 |
| 5.3.3. | Human respiratory monitoring | 139 |
| 5.3.4. | Hysteresis and Stability | 141 |
| 5.4. | Discussion | 144 |
| 5.5. | Summary | 147 |
| 5.6. | References | 147 |
| CHAPTER 6 | CONCLUSIONS AND SCOPE FOR FUTURE WORK | 155 |
| 6.1. | Scope for future work | 159 |
| 6.2. | References | 160 |

LIST OF FIGURES

| Figure No. | Figure Captions | Page No. |
|--------------------|---|----------|
| Figure 1.1. | Schematic showing the basic components of MEMS and their important functionalities. | 2 |
| Figure 1.2. | Schematic showing an overview of general processes involved in microfabrication of a MEMS device. | 4 |
| Figure 1.3. | (a) Schematic of a microcantilever (MC) where, L, W and T stands for its length, width and thickness, respectively. (b) A typical SEM image of a released MC structure. | 5 |
| Figure 1.4. | Schematic of MC working modes. (a) In static mode, one face is usually functionalized () and the deflection of MCs due to surface stress change when analytes () adsorb, is measured. (b) In dynamic mode the MCs are usually operated at its resonance frequency and the shift in resonance due to added analytes () is measured. This image is adapted from reference [32]. | 7 |
| Figure 1.5. | Schematic of a (a) typical optical read-out method where the deflection of the MCs is detected by a laser and photo-diode arrangement and (b) piezo-resistive MC with embedded piezoresistive layers (at the fixed end) and contact pads for electrical output. | 10 |
| Figure 1.6. | Schematic of MC to relate the radius of curvature R to its deflection. | 11 |
| Figure 2.1. | Block diagram of Direct Laser Writer (Adapted from User Manual, LB405B, M/s Microtech, Italy). | 39 |
| Figure 2.2. | (a) Photograph and (b) schematic of the direct laser writer used in the present work. (c) Typical soft mask used to transfer the MC patterns on PR coated wafers. Mask file is divided into strips and is written in a serial fashion. Strip width and number depends on the selected lens and its overlap (D-step) can be adjusted by the user interface. | 39 |

| | | |
|---------------------|---|----|
| Figure 2.3. | Setup inside wet chemical bench for performing Si etching using TMAH solution followed by rinsing in DI water. | 40 |
| Figure 2.4. | (a) Block diagram and (b) photograph of 3D OM used in the present work. Inset in (b) shows the magnified image of the interferometric microscope objective focused on the sample placed on the X-Y stage. | 42 |
| Figure 2.5. | (a) Photograph and (b) block diagram of NVA used in the present work. | 43 |
| Figure 2.6. | Resonance spectrum of a typical 210 μm long SiO_2 MC recorded using NVA, from which resonance frequency and Q-factor values were extracted. | 44 |
| Figure 2.7. | (a) Photograph and (b) block diagram of LDV used in the present work for microcantilever resonance frequency measurements. | 45 |
| Figure 2.8. | (a) High-resolution LDV scan at resonance and its (b) Lorentzian fit on a typical released 130 μm long MC. | 46 |
| Figure 2.9. | (a) Photograph of the AFM used in the present work. (b) Surface morphology of a typical SiO_2 surface imaged through AFM. From this, the RMS roughness of the surface was estimated to be ~ 4.1 nm. | 47 |
| Figure 2.10. | MC structure designed and simulated using FEM software with a mesh size of $1 \mu\text{m}^3$. The color code represents the amplitude of vibration and it can be clearly seen that the amplitude is maximum at its free end. | 48 |

| | | |
|---------------------|---|----|
| Figure 2.11. | <p>(a) Relative shift in the resonance frequency of SiO₂ MCs due to the presence of surface patterns, with varying pattern depth, estimated using FEM simulations. Inset shows the relative shift in the resonance frequency of SiO₂ MCs as a function of surface pattern size. (b) Static deflection of the MCs estimated using FEM simulation along with experimentally reported values from literature, while RH is varied between 6 to 50%. Inset shows the schematic diagram of MC and the loading scenario used in FEM simulations based on Zhang et al. [6] model. The surface stress is modeled as the uniformly distributed axial stress $\sigma = sW$ and a uniformly distributed bending moment $m = sWT/2$ where s is the uniformly distributed area stress and W and T are the width and the thickness of the MC.</p> | 49 |
| Figure 2.12. | <p>Deconvolution of mean and gradient residual stress components from initial bending profile of MCs. (a) Deflection profile of a typical released SiO₂ MC across its length. From this, (b) mean and (c) gradient residual stress values were estimated using Fang's et al. model [8].</p> | 52 |
| Figure 2.13. | <p>Typical temperature profile used for high temperature annealing of SiO₂ MCs in O₂ environment.</p> | 53 |
| Figure 2.14. | <p>(a) Top and side views of the custom-made air-tight environmental chamber designed for RH sensing experiments. Photograph of the (b) environmental chamber and (c) RH sensing setup where it is mounted on the XY stage of NVA. In these photographs, electrical connection for piezo actuator and gas inlet ports are also clearly seen.</p> | 54 |
| Figure 2.15. | <p>(a) Schematic and (b) photograph of the experimental setup used for measuring the shift in the resonance frequency of the MCs using NVA when the RH is varied between 20% and 90%.</p> | 55 |
| Figure 2.16. | <p>Typical calibration plot showing the variation of RH (red line) and temperature (blue line) inside the chamber, with time. These measurements were performed using a commercial RH sensor while RH inside the chamber was varied.</p> | 56 |

| | | |
|---------------------|--|----|
| Figure 2.17. | Experimental setup for monitoring human respiration during inhale/exhale breath cycles. | 57 |
| Figure 3.1. | Various process steps involved in the fabrication of SiO ₂ MCs. (a) Starting material: Si <100> wafer with 0.98 μm thick thermal SiO ₂ . (b) 1.4 μm thick photoresist (PR) is coated using spin coater. (c) MC pattern is transferred on PR using DLW followed by buffered oxide etching of SiO ₂ . (d) PR is stripped using acetone and cleaned with IPA. (e) Underlying Si is etched in TMAHw solution to finally release the SiO ₂ MC. | 64 |
| Figure 3.2. | FESEM images of the typical SiO ₂ MCs fabricated in the present work. A tip at the free end is added to avoid the stiction while releasing the MCs by wet chemical etching method. | 66 |
| Figure 3.3. | (a) Schematic of different crystallographic orientations in Si {100} wafer with respect to the wafer prime flat. (b) Typical mask layout showing MCs oriented along <110> and <100> directions. Evolution of Si undercutting when SiO ₂ MCs are oriented along (c) <100> and (d) <110> directions with respect to underlying Si {100} wafer [1]. In (c) and (d) the black dotted lines represent the progressing direction of Si etching in TMAH solution, with time. (e) Typical optical microscope image of a SiO ₂ MC oriented in <100> direction after 50 minutes of Si etching. Underlying Si, along the width of the MC is clearly seen in this image. | 67 |
| Figure 3.4. | (a) MC test pattern used for estimating the critical laser dose “D _c ”. (b) – (g) shows the optical microscope images of the transferred MC pattern on PR using DLW at various laser doses from 160 mJ/cm ² to 320 mJ/cm ² . From this study, D _c for optimum pattern transfer was estimated to be 272 mJ/cm ² . | 68 |

| | | |
|---------------------|--|----|
| Figure 3.5. | <p>Photoresist post-baking temperature optimization. (a) Optical microscope image of the transferred MC pattern on SiO₂ after post-baking the PR at 120°C followed by BOE (b) along with the mask pattern used. (c) Dektak line profile of the transferred pattern along the width of the MC. The dotted line shows the actual mask pattern for comparison. From this data undercut ratio, U_R was estimated.</p> | 69 |
| Figure 3.6. | <p>Role of PR adhesion on the SiO₂ undercutting during BOE (cross-section schematic). White (r) and black (s) dotted lines depict the resultant transferred pattern in SiO₂ due to resist peel off and inevitable undercutting in BOE.</p> | 71 |
| Figure 3.7. | <p>Plot between post-bake temperature and undercutting ratio, U_R. The inset shows the optical microscope image of the MC pattern after post-baking at 150°C with minimum undercutting.</p> | 72 |
| Figure 3.8. | <p>Typical mask file (a) without and (c) with anti-stiction tip along with the (b) stuck and (d) fully released MCs (L = 90 μm), respectively, after TMAH etching of Si and immediate rinsing in DI water.</p> | 73 |
| Figure 3.9. | <p>Schematic of the process steps involved in the fabrication of surface micro-patterned SiO₂ MCs along with the corresponding optical microscope images. (a) Starting material: Si {100} wafer with ~0.98 μm thick SiO₂, (b) MC pattern and (c) ordered surface micro-patterns (4 μm² with a pitch of 6 μm) transferred on SiO₂ layer using two-layer lithography process, (d) TMAHw etching of underlying Si to finally release MCs.</p> | 74 |
| Figure 3.10. | <p>Typical optical microscope images of released MCs with controlled micro-patterns on their surface. From left to right depth of micro-patterns is increasing from 15 nm to 75 nm.</p> | 74 |

| | | |
|---------------------|---|----|
| Figure 3.11. | (a) FESEM image of a typical surface micro-patterned SiO ₂ MC. Inset shows the magnified view of the free end of MC, where the micro-patterns are clearly seen. (b) Typical micro-pattern on a MC surface recorded using AFM. From this image depth of the pattern was estimated to be ~15 nm. | 75 |
| Figure 3.12. | (a) Typical 3D profile of a released 110 μm × 37 μm × 0.98 μm SiO ₂ MC. (b) Line profile of the same MC across its length (shown as a white line in (a)). Out of plane deflection seen in this figure indicates the presence of inherent gradient residual stress in the SiO ₂ film. (c) Peak deflection vs. square of the length of the MCs fabricated in the present work. From the slope of the linear fit of this data, gradient stress in the film was estimated to be 15.14 ± 0.32 MPa. | 77 |
| Figure 3.13. | (a) Typical deflection profiles across the length of the micro-patterned MCs. For comparison, profile recorded on unpatterned MC is also shown. (b) Plot of peak bending magnitude estimated from the bending profiles as a function of pattern depth. | 79 |
| Figure 3.14. | Typical resonance spectrum of a MC recorded using NVA and from the Lorentzian fit resonance frequency and Q-factor values were extracted. | 80 |
| Figure 3.15. | Analytical and the experimental resonance frequency of MCs with the inverse square of length (L) (error bar is of the symbol size in the experimental data). | 81 |
| Figure 3.16. | (a) Schematic of MC with non-rectangular cross-section and (b) cross-sectional view of the MC patterned by isotropic wet etching. The magnitude of asymmetry is exaggerated for clarity. (c) Optical microscope image of a typical SiO ₂ MC released in the present work. Undercut region at the fixed end is shown by a triangle. | 82 |

| | | |
|---------------------|--|----|
| Figure 3.17. | <p>(a) Experimental resonance frequency with the length of MCs and is fitted to $f(x) = m/(L + \Delta L)^2 + c$ by the least square method to estimate the ΔL. (b) Experimental and analytical resonance frequency with the inverse square of corrected effective length. Collapse of these two data on each other indicates that the leading correction in resonance frequency estimation comes from extra length introduced due to undercutting.</p> | 83 |
| Figure 3.18. | <p>Experimentally estimated Quality factor of the released MCs as a function of their respective resonance frequencies.</p> | 84 |
| Figure 3.19. | <p>(a) Typical resonance frequency spectra of micro-patterned MCs. For comparison, resonance spectrum of an unpatterned MC is also shown. From the Lorentzian fit, resonance frequency and Q-factor values were estimated. (b) Mean resonance frequency (blue solid line) and Q-factor (green dotted line) of MCs as a function of pattern depth. In this figure 0 nm pattern depth denotes the frequency of unpatterned MCs.</p> | 85 |
| Figure 4.1. | <p>Experimentally measured resonance frequency of MCs versus their length. Here error bar is of the size of the symbol. Inset shows the similar plot with FEM simulated values. Inset also shows the snapshot of meshed ($1 \mu\text{m}^3$) MC structure used for simulations. The color code represents the amplitude of vibration and it can be clearly seen that the amplitude is maximum at its free end.</p> | 95 |
| Figure 4.2. | <p>The relative difference between experimental (f_1) and FEM simulated (f_2) resonance frequency ($\Delta f/f$) ($= (f_1 - f_2)/f_1 \times 100$) plotted against W/L of MCs.</p> | 96 |
| Figure 4.3. | <p>The relative shift in resonance frequency of MCs in air and vacuum (FEM) computed using Sader's model [23] as a function of W/L of MCs.</p> | 98 |
| Figure 4.4. | <p>Variation of principal (K_x) and transverse (K_y) curvature values with the W/L ratio of MCs. Equivalent surface stress estimated using eq. 4.2 is shown on the right axis.</p> | 99 |

| | | |
|---------------------|--|-----|
| Figure 4.5. | Variation of relative frequency shift with (a) longitudinal (K_x) and (b) transverse (K_y) curvature present in SiO_2 MCs. The dotted line is a guide to the eye. It is evident from (b) that in region-I, the frequency shift is independent of K_y whereas it linearly increases in region-II and reduces marginally in region-III. | 100 |
| Figure 4.6. | (a) Comparison of the experimental frequency shift in the present work with various available theoretical models. Theoretical frequency shifts were suitably scaled to superimpose with our experimental data. (b) Square of dimensionless curvature ($K_{x,y}L$) as a function of W/L (c) Comparison of experimental frequency shift as a function of W/L along with Ruz et al [19] model for both x and y components of curvature. | 106 |
| Figure 4.7. | (a) Typical bending profiles of the MCs before and after annealing (at 800°C and 1000°C) in O_2 . (b) Typical line profiles of the MCs before and after pre-release annealing in O_2 at 800°C. | 110 |
| Figure 4.8. | Typical line profiles of the MCs before and after annealing in O_2 and N_2 atmospheres at a constant temperature of 1000°C. | 112 |
| Figure 4.9. | Peak deflection as a function of square of the length of the MCs before and after annealing at 800°C and 1000°C in O_2 . | 113 |
| Figure 4.10. | (a) Mean (σ_0) and (b) gradient(σ_1) residual stress values before and after 800°C annealing as a function of MC length. σ_0, σ_1 values were estimated by fitting the corresponding line profiles of MCs to a second-order polynomial function. | 114 |
| Figure 4.11. | (a) Resonance spectrum of a typical 110 μm long MC before and after annealing along with Lorentzian fit. (b) Relative difference in resonance frequencies of MCs before and after annealing ($\Delta f/f \%$) plotted as a function of MC length. | 115 |

| | | |
|--------------------|---|-----|
| Figure 5.1. | <p>(a) Relative resonance frequency shift ($(\Delta f/f)\%$) in a typical SiO_2 MC ($210 \times 37 \times 0.98 \mu\text{m}^3$) and (c) estimated Q-factor as a function of time during one RH increase and decrease cycle between 44% to 58%. The green dotted line shows the variation in RH inside the chamber as a function of time, measured independently, keeping the temperature constant at 24°C. (b) The relative shift in the resonance frequency of MC as a function of RH. From the shift in frequency, the adsorbed/desorbed mass is estimated using equation 5.3 and is shown on the right axis.</p> | 128 |
| Figure 5.2. | <p>The statistical data of resonance frequency values independently measured on unpatterned and 15 nm deep micro-patterned MCs.</p> | 131 |
| Figure 5.3. | <p>(a) Relative resonance frequency shift ($(\Delta f/f)\%$) and (b) Q-factor of typical micro-patterned and unpatterned MCs when RH is increased from 20% to 90%, respectively. From the shift in frequency, adsorbed mass is estimated using equation (5.3) and is shown on the right axis of (a). In these graphs, the error bar is of the size of the symbol used.</p> | 132 |
| Figure 5.4. | <p>Mechanism of water adsorption on micro-patterned MC surface in three different regions shown in figure 5.2. (a) In Region – I (i.e. $20\% < \text{RH} < 40\%$), the water molecule adsorption occurs on exposed hydroxylated SiO_2 surface (b) In the region – II ($40\% < \text{RH} < 60\%$), presence of gel-like structure of water molecules in the micro-patterned regions increases the effective uptake of water by several times and (c) In Region- III ($\text{RH} > 60\%$), closed water films are formed due to random hydrogen bonding between the water molecules as shown by light cyan region on top.</p> | 134 |

| | | |
|---------------------|--|-----|
| Figure 5.5. | Relative resonance frequency shift ($(\Delta f/f)\%$) of 15 and 75 nm deep surface micro-patterned MCs when the RH is increased from 20% to 90%. In this graph, the error bar is of the size of the symbol used. | 137 |
| Figure 5.6. | (a) The shift in peak amplitude at resonance as a function of time when RH is switched between ~23% and 57%, on a typical micro-patterned MC. From this data (b) response and (c) recovery times of these devices were estimated. | 139 |
| Figure 5.7. | Response of a typical micro-patterned MC for slow and normal breathing inhale-exhale cycles of a healthy male adult. The right axis shows the variation in RH during breath cycles. | 140 |
| Figure 5.8. | Response of commercial RH sensor which is placed inside the environmental chamber during the human breath monitoring experiment. | 141 |
| Figure 5.9. | Relative resonance frequency shift of a typical surface micro-patterned MC during one RH increase and decrease cycle from 20% to 90%. From this figure, hysteresis value was estimated to be <3 %RH for all the three RH regions defined. | 142 |
| Figure 5.10. | Relative resonance frequency shift of a typical surface micro-patterned MC when the RH is varied from 20% to 90% after 1 day, 5 days, and 30 days of device fabrication. From this figure, the long-term stability of the MCs and the degree of fluctuation was estimated to be < 5% for the entire RH range studied. Inset shows the variation in sensor response over a period of time when RH is maintained at 80%. | 143 |

LIST OF TABLES

| Table No. | Table Caption | Page No. |
|-------------------|--|----------|
| Table 3.1. | Various process parameters set in DLW for pattern transfer on PR coated wafer and details about the soft-mask file. | 63 |
| Table 3.2. | Various process parameters optimized at each stage of the fabrication process for the successful released of SiO ₂ MCs. | 65 |
| Table 3.3. | Details of micro-patterned MCs with varied pattern-depths released in the present work. | 76 |
| Table 3.4. | Comparison of gradient residual stress values reported in SiO ₂ films, obtained from MC bending measurements. | 78 |
| Table 4.1. | Various experimental studies reported in the literature along with the present work for surface stress induced resonance frequency shifts. | 103 |
| Table 4.2. | Various analytical models for estimating the surface stress induced resonance frequency shift. In this table, $\Delta f/f$ is the relative frequency shift, σ_y is the equivalent differential surface stress estimated from eq. 4.2, ν and E are Poisson's ratio and Young's modulus of SiO ₂ , respectively and L, W and T are the length, width and thickness of the MCs, respectively. | 105 |
| Table 4.3. | Details about the annealing experiments carried out on various samples. | 109 |
| Table 4.4. | The slope values extracted from z_{max} Vs. L^2 plot for the samples shown in table 4.3. | 113 |
| Table 5.1. | RH and mass sensitivities of unpatterned and micro-patterned MCs in three different RH regions shown in Fig. 5.3 (a). | 133 |
| Table 5.2. | Comparison of RH sensing characteristics of various nanostructured materials coated on MCs reported in the literature along with the present work. | 146 |

LIST OF SYMBOLS

| | | |
|----------------|---|--|
| L | : | Length of microcantilever |
| W | : | Width of microcantilever |
| T | : | Thickness of microcantilever |
| E | : | Young's Modulus |
| ν | : | Poisson's Ratio |
| K | : | Curvature |
| K_x | : | Principal curvature |
| K_y | : | Transverse curvature |
| R | : | Radius of curvature |
| U | : | Displacement |
| I | : | Geometric moment of Inertia |
| M | : | Bending moment |
| θ | : | Deflection angle |
| σ | : | Surface stress |
| $\Delta\sigma$ | : | Differential surface stress |
| γ | : | Cross-sectional area of microcantilever |
| $\varphi(z,t)$ | : | Displacement of microcantilever in the z-direction |
| ρ | : | Mass density |
| f_n | : | Frequency of motion of microcantilever |
| k_f | : | Effective stiffness of microcantilever |
| m^* | : | Effective mass of microcantilever |
| S | : | Mass sensitivity of microcantilever |

| | | |
|--------------------|---|---|
| P | : | Pressure |
| λ | : | Wavelength |
| $\Delta f/f$ | : | Relative shift in frequency of microcantilever |
| σ_{tot} | : | Uniaxial residual stress in a thin film |
| σ_0 | : | Mean residual stress of a thin film |
| σ_1 | : | Gradient residual stress of a thin film |
| θ_0 | : | Curvature of microcantilever due to gradient stress |
| θ_1 | : | Curvature of microcantilever due to mean stress |
| D_c | : | Critical laser dose |
| I | : | Intensity of laser |
| a | : | Absorption coefficient |
| h | : | Thickness of photoresist |
| U_R | : | Undercut ratio |
| d | : | Thickness of SiO ₂ |
| d_l | : | Width of the MC measured at the top after etching |
| z_{max} | : | Peak deflection magnitude of microcantilever |
| σ_{max} | : | Peak gradient residual stress of microcantilever |
| ΔL | : | Extra length of microcantilever due to undercutting |
| ρ_f | : | Density of air |
| ρ_c | : | Mass density of SiO ₂ |
| $\Gamma_r(\omega)$ | : | Real part of the hydrodynamic function |
| c | : | Mode-dependent constant |
| $K_s L$ | : | Dimensionless curvature |
| P_p | : | Partial pressure of water vapor |

| | | |
|--------------------|---|--|
| P_s | : | Saturation vapor pressure of the air |
| f_i | : | Initial resonance frequency of the microcantilever |
| f_f | : | Final resonance frequency of the microcantilever |
| n | : | Geometric factor of microcantilever |
| M_{H_2O} | : | Molecular mass of water |
| ρ_{H_2O} | : | Density of water |
| N_A | : | Avogadro's number |
| A_{MC} | : | Surface area of microcantilever |
| H | : | Hysteresis |
| μ^s, λ^s | : | Isotropic surface moduli |
| g | : | Average surface slope |

LIST OF ABBREVIATIONS

| | | |
|----------|---|---|
| MEMS | : | MicroElectroMechanical Systems |
| MC(s) | : | Microcantilever(s) |
| DLW | : | Direct Laser Writer |
| IR | : | Infra-Red |
| UV | : | Ultra-Violet |
| RH | : | Relative Humidity |
| AH | : | Absolute Humidity |
| CVD | : | Chemical Vapor Deposition |
| FESEM | : | Field Emission Scanning Electron Microscope |
| 3D OM | : | 3D Optical Microscope |
| NVA | : | Nano Vibration Analyzer |
| LDV | : | Laser Doppler Vibrometer |
| FEM | : | Finite Element Modeling |
| AFM | : | Atomic Force Microscope |
| CCD | : | Charge-Coupled Device |
| VSI | : | Vertical Scanning Interferometry |
| USB | : | Universal Serial Bus |
| NA | : | Numerical Aperture |
| TEM | : | ThermoElectroMechanical |
| W/L | : | Width to Length ratio |
| W/T | : | Width to Thickness ratio |
| PSD | : | Position-sensitive Detector |
| Q-factor | : | Quality Factor |

| | | |
|---------|---|---------------------------------------|
| FWHM | : | Full Width at Half Maximum |
| SAM | : | Self Assembled Monolayer |
| DI | : | De-ionized |
| PR | : | Photoresist |
| TMAH(w) | : | Tetramethylammonium Hydroxide (water) |
| KOH | : | Potassium Hydroxide |
| EDP | : | Ethylenediamine Pyrocatechol |
| IPA | : | Iso Propyl Alcohol |
| BOE | : | Buffered Oxide Etchant |
| PMMA | : | Poly methyl methacrylate |
| DMMP | : | Dimethyl methylphosphonate |
| TNT | : | Trinitrotoluene |
| VOC(s) | : | Volatile Organic Compound(s) |
| LED | : | Light Emitting Diode |
| QCM | : | Quartz Crystal Microbalance |
| SAW | : | Surface Acoustic Wave |
| IDT | : | Interdigital Transducer |

Chapter 6

Conclusions and Scope for Future work

Present thesis principally described the fabrication and characterization of SiO₂ MCs in detail and explored them for ultra-high sensitive RH sensing application. Certain important aspects of MC based sensors, such as the effect of biaxial curvature on the resonance frequency of the MCs and high-temperature annealing on the residual stress evolution, are also studied. An innovative method to enhance the RH sensitivity of SiO₂ MCs by introducing controlled surface micropatterns on their surface is proposed and the same devices were successfully put to use for human breath monitoring study/application. Major findings and conclusions of the present thesis are summarized now.

a) Fabrication of SiO₂ microcantilevers:

- SiO₂ MCs of various dimensions were successfully fabricated using DLW unit and wet chemical etching methods. Various micro-fabrication process parameters were optimized and are summarized (Table 3.1 & Table 3.2). It is shown that, even for fabricating simple structures like MCs, DLW can be a valuable tool if optimizations at design level are desired.
- An effective method to avoid stiction in SiO₂ MCs while releasing them by wet chemicals, is proposed. It is shown that introduction of a sharp convex tip at the free end of the MC along with a post-etch rinsing in boiling DI water, which are otherwise considered separately, reduces the stiction substantially, even in the longest MCs (L = 330 μm) studied in the present work.

- From the initial bending measurements on the released MCs of various lengths, we found that there exists a linear relationship between MC length and its peak deflection. Using this relation gradient residual stress present in the SiO₂ film was estimated and found to be 15.14 ± 0.32 MPa.
- Experimentally measured resonance frequencies of MCs were compared to the analytically estimated values and it was found that compared to the role of non-rectangular cross-section of these MCs, the presence of undercutting, which increases the effective length, influences the resonance frequency estimation most, especially at smaller lengths. From the resonance frequency measurements, Q-factor was estimated and found to increase with reducing MC dimensions.

b) Characterization of SiO₂ microcantilevers:

- Through systematic experiments, it is demonstrated that the presence of biaxial curvature in as-fabricated (uncoated) MCs directly increases their stiffness when their Width to Length ratio (W/L) is between 0.16 and 0.35. Nonlinear stiffening and clamping geometric effect present in MCs are shown to be the reasons for the observed positive frequency shift (due to increase in stiffness) and compared to principal curvature (K_x), transverse curvature (K_y) seems to play a dominant role on the observed frequency shift.
- Also, for the first time, it is shown that the competing plate softening effect due to the presence of unrelaxed transverse curvature along with the nonlinear plate stiffening effect as the reason for the decrease in frequency shift with increasing curvature, for $W/L > 0.35$, validating Ruz et al. [1] model.

- Comparison of various experimental studies and analytical models reported in the literature on the role of surface stress/ curvature on the resonance frequency of MCs revealed the following.
 - ❖ When W/L of MCs is < 0.2 , the observed frequency shift is $< 1\%$ and is independent of the magnitude of surface stress. Whereas, when W/L ratio > 0.2 , no correlation exists between these two parameters.
 - ❖ Most of the reported analytical models seem to only predict the dimensional dependence and not the absolute value of the experimentally observed frequency shift. This discrepancy is believed to be due to the presence of unspecified effects such as variation in surface morphology of MCs and no single method being adopted for the generation of surface stress.
- Post-release high-temperature annealing of SiO₂ MCs increases their curvature and is attributed to the onset of plastic deformation of these structures at elevated temperatures.
- Mean (σ_0) and gradient (σ_1) residual stress values increase with annealing temperature and b) the magnitude of increase depends on the annealing environment and MC length. These are explained based on stress accumulation resulting from the additional oxide layer growth at the SiO₂/Si interface below the fixed end and clamping constraints of SiO₂ MCs.
- Increase in curvature due to high-temperature annealing was also found to increase the resonance frequency of MCs validating the hypothesis of biaxial curvature induced stiffness changes in these devices.

c) Relative humidity sensing studies using SiO₂ microcantilevers

- An air-tight environmental chamber to be used with NVA was indigenously designed and fabricated for RH sensing and human breath monitoring studies using SiO₂ MCs.
- It is shown that as fabricated SiO₂ MCs can be effectively used as RH sensors, in dynamic mode, without any functionalization, with maximum sensitivity and resolution of 4.08 Hz/%RH and < 1% RH, respectively.
- In order to enhance the RH sensitivity, SiO₂ MCs with controlled micro-patterns were fabricated. Resonance frequency measurements on micro-patterned MCs revealed that both resonance frequency and Q-factor values reduce only marginally with respect to unpatterned ones when pattern depth is ~ 15 nm.
- It is shown that introduction of controlled micro-patterns on the MC surface provides a simple and efficient way to enhance the sensitivity of MC based sensors without compromising other sensor characteristics such as response and recovery times. Micro-patterned sensors were found to have an unprecedented RH sensitivity (10.45 Hz/% RH), very low hysteresis value (< 3 %RH), fast response/recovery times (~1 s) and excellent stability (variation <5%) over a wide range of RH variation from 20% to 90%.
- The enhancement in RH sensitivity in the case of micro-patterned MCs is explained with a model, where it is shown that the formation of *gel-like* water layer inside the cavities facilitates enhanced uptake of water molecules.
- Finally, the micro-patterned MCs are demonstrated for human breath monitoring with excellent response and recovery times during both slow and fast breath cycles.

6.1. Scope for future work

- In the present thesis, an effective method is proposed to avoid stiction during the fabrication of SiO₂ MCs of various lengths. It is well known that thickness [2] and width [3,4] of MCs equally influence the stability of MCs. Therefore, it will be interesting to study the role of MC thickness and width on the effectiveness of the anti-stiction tip.
- In the present work, it is shown that the presence of controlled micro-patterns will enhance the RH sensitivity of MCs without compromising other sensor characteristics. More systematic studies on the effect of micro-pattern dimensions vis-à-vis MC dimensions will provide more insights into the mechanism of enhanced RH sensitivity.
- The effect of adsorption induced surface stress on the stiffness of MCs is extensively studied in the literature [1,5,6]. But most of the theoretical works either under or over predict the observed experimental results. This discrepancy could be due to several unspecified effects such as surface morphology, surface preparation mechanisms, and inherent biaxial curvature as pointed out in the present thesis. Efforts should be made to fabricate MCs with precise control over the parameters such as physical dimension, surface morphology, etc. so that their influence on the stiffness can be studied independently.
- MCs used in the present work are uncoated and therefore inherently lack selectivity [7,8]. Recently, Iglesias et al. [8] proposed a method to improve the selectivity of uncoated MCs by simultaneously measuring the Q-factor (viscosity) and resonance frequency (mass density) for discriminating and quantifying different gases present in a binary gas mixture. It will be interesting to explore micro-patterned MCs

developed in the present work for this purpose. In the future, robust methods to improve the selectivity of uncoated MCs by modifying the pattern dimensions and geometry (to vary the surface inclination angle of the patterns) need to be explored. Also, the role of temperature on the RH sensitivity of these devices to be studied.

- For RH sensing studies, the resonance frequency of MCs is measured using NVA. However, for real-time field applications, MCs should be integrated with piezoresistive read-out and is scope for future work.

6.2. References

- [1] J.J. Ruz, V. Pini, O. Malvar, P.M. Kosaka, M. Calleja, J. Tamayo, Effect of surface stress induced curvature on the eigenfrequencies of microcantilever plates, *AIP Adv.* 8 (2018) 105213.
- [2] Z. Li, Y. He, J. Lei, S. Han, S. Guo, D. Liu, Experimental investigation on size-dependent higher-mode vibration of cantilever microbeams, *Microsyst. Technol.* 25 (2019) 3005–3015.
- [3] X.L. Peng, L. Zhang, Z.X. Yang, Z.Y. Feng, B. Zhao, X.F. Li, Effect of the gradient on the deflection of functionally graded microcantilever beams with surface stress, *Acta Mech.* (2020).
- [4] F. Bayram, D. Gajula, D. Khan, S. Gorman, G. Koley, Nonlinearity in piezotransistive GaN microcantilevers, *J. Micromechanics Microengineering.* 29 (2019).
- [5] M.J. Lachut, J.E. Sader, Effect of surface stress on the stiffness of thin elastic plates and beams, *Phys. Rev. B - Condens. Matter Mater. Phys.* 85 (2012) 1–11.
- [6] A.N. Sohi, P.M. Nieva, Frequency response of curved bilayer microcantilevers with applications to surface stress measurement, *J. Appl. Phys.* 119 (2016).

- [7] I. Dufour, F. Josse, S.M. Heinrich, C. Lucat, C. Ayela, F. Ménil, O. Brand, Unconventional uses of microcantilevers as chemical sensors in gas and liquid media, *Sensors Actuators, B Chem.* 170 (2012) 115–121.
- [8] L. Iglesias, M.T. Boudjiet, I. Dufour, Discrimination and concentration measurement of different binary gas mixtures with a simple resonator through viscosity and mass density measurements, *Sensors Actuators, B Chem.* 285 (2019) 487–494.

Thesis Abstract

In the present work, SiO₂ Microcantilevers (MCs) of various dimensions (length (L) = 50 – 330 μm; width (W) = 40 μm; thickness (T) = 0.98 μm), were successfully fabricated using Direct Laser Writer (DLW) and wet chemical etching methods and explored for Relative Humidity (RH) sensing. Various microfabrication process parameters such as laser dose (in DLW), pre/post backing temperatures were optimized. An innovative method is proposed to avoid “stiction” in these devices while releasing them using wet chemicals. It is shown that introducing a sharp convex tip at the free end of the MC along with a post-etch rinsing in boiling de-ionized (DI) water, which are otherwise considered separately, reduces the stiction substantially. Successfully released MCs were characterized using 3D optical microscope and Nano Vibration Analyser (NVA), for curvature and resonance frequency measurements, respectively. From the curvature measurements, gradient residual stress in SiO₂ film was estimated and found to be 15.14 ± 0.32 MPa. Experimentally measured resonance frequency values were found to be lower than the analytically estimated ones (especially at smaller lengths) and is explained based on increase in the effective length of the MCs due to undercutting.

As a prelude to RH sensing studies, the effect of i) inherent biaxial curvature on the resonance frequency and ii) high-temperature post-release annealing on the residual stress evolution of SiO₂ MCs, are studied. Through systematic experiments, it is shown that the presence of biaxial curvature in SiO₂ MCs directly increases their resonance frequency when their Width to Length ratio (W/L) is between 0.16 and 0.35. Also, it is shown that, compared to principal curvature, transverse curvature plays a dominant role

on the observed frequency shift. Similarly, post-release high-temperature annealing (800°C and 1000°C in O₂ and N₂) studies on SiO₂ MCs revealed that these devices undergo an irreversible increase in static deflection (plastic deformation) with annealing and this effect is more when the annealing environment is O₂. Based on these studies, it was decided to use as-fabricated SiO₂ MCs with W/L < 0.16, in dynamic mode, for RH sensing studies.

RH sensing experiments were performed by measuring the shift in resonance frequency of SiO₂ MCs using NVA (at ambient conditions) when RH is varied between 20% and 90%. For this purpose, an air-tight chamber was indigenously designed, fabricated and calibrated in the entire RH range. The resonance frequency of MCs was found to decrease (increase) during the RH increase (decrease) cycle and is attributed to the physisorption of water molecules on the SiO₂ surface. These experiments revealed that, as fabricated SiO₂ MCs can be effectively used as RH sensors in dynamic mode, without any functionalization, with maximum sensitivity and resolution of 4 Hz/%RH and < 1% RH, respectively. To increase the RH sensitivity, MCs are usually coated with nanomaterials, which is known to deteriorate other sensor characteristics such as response/recovery times. As an alternative to this, in the present thesis, it is shown that the introduction of controlled micro-patterns (4 x 4 x 0.015 μm³) on the MC surface can enhance their RH sensitivity without compromising the response/recovery times and hysteresis. For this purpose, SiO₂ MCs with controlled micro-patterns were fabricated using two-layer lithography. Presence of micro-patterns on the MC surface was found to increase their RH sensitivity by two times (10 Hz/% RH) while retaining the response/recovery (~ 1 s) and hysteresis error (< 3%RH) along with outstanding stability (variation < 5%) of uncoated MCs. An increase in sensitivity in these devices

is explained with the help of a model, where it is shown that the formation of gel-like water layer inside the cavities facilitates the enhanced uptake of water molecules. Finally, real-time monitoring of human respiration during fast and slow cycles using micro-patterned MCs is demonstrated. The findings of the present thesis are expected to be of great value to the design and fabrication of SiO₂ MCs for various sensing applications, in dynamic mode.

Chapter 1

Introduction to Microcantilevers

Chapter 1 begins with a brief introduction to MicroElectroMechanical Systems (MEMS) technology, its components, application, and microfabrication technology. This is followed by a detailed introduction to Microcantilever (MC) based sensors, their modes of operation (static and dynamic), common materials used and typical process flow for MC fabrication. Various excitation and read-out techniques are also discussed. Subsequently, the basic equations governing the static and dynamic modes of operation, i.e. Stoney's equation for surface stress-induced bending of MCs and Euler-Bernoulli beam equation for resonance frequency are derived and a brief note on energy dissipation mechanism in MCs and its experimental quantification are given. The advantages of SiO₂ MCs compared to conventional Si and Si₃N₄ MCs along with a literature survey on some of the recent physical, chemical, and biological sensing studies using SiO₂ MCs are presented. Followed by this, a brief note on the influence of functionalization and surface modification on the response of the MCs are discussed. Finally, motivation and the methodology adopted to achieve them are given.

1.1. Introduction to MEMS

Miniaturization science is the science to manufacture ever smaller mechanical, electrical, and optical devices to attain unprecedented functionality compared to devices in macro-scale with added advantages of compactness, portability, reliability, low power consumption, and low cost of production [1,2]. The resulting structures form the key elements i.e., basic electronics, sensors, and actuators of today's modern computers, mobile phones, automobiles, medical diagnostic instruments, etc. [3]. Miniaturization is

practically executed through a rapidly growing technology called MicroElectroMechanical Systems or MEMS. These are systems which comprise of miniaturized mechanical elements, sensors, actuators, and electronic components that are integrated and packaged on a single silicon substrate [4,5]. Schematic of basic components present in a typical MEMS is shown in figure 1.1. The microsensors gather the desired physical quantity from the environment as the input through the mechanical deformation of microfabricated components such as fixed-free beams (MCs), fixed-fixed beams (bridges), or suspended membranes [6] and feeds this data to microelectronics for processing. The transduced signal from microelectronics is then fed to actuating elements to give the desired mechanical output.

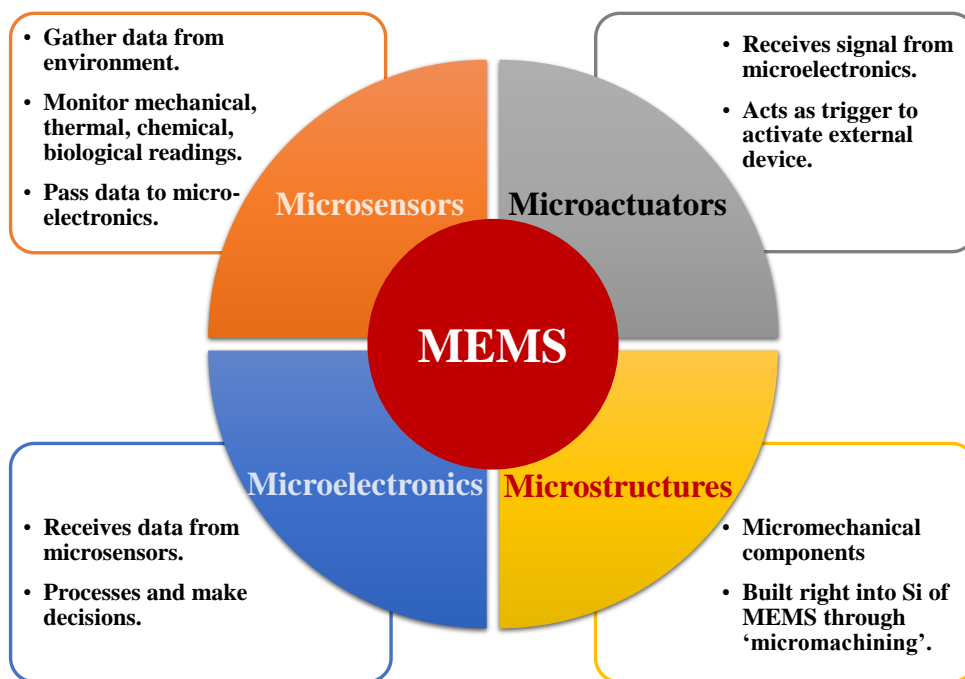


Figure 1.1. Schematic showing the basic components of MEMS and their important functionalities.

MEMS have a wide range of applications in a variety of fields such as physical/chemical/biological sensing, biomedical industries, climatology, communication, agriculture, food processing industries, and automobile industries [2,4,7]. Some of the widely studied MEMS sensors in these application fields are inertial sensors

(accelerometers, gyroscopes), gas sensors, humidity sensors, pressure sensors, temperature sensors, and force sensors. Examples of actuators include microlenses/mirrors, micro-motors, micro-grippers, fluidic valves, inkjet printer heads, pumps, thermal bimorph actuators, and comb-drive electrostatic actuators [3,8].

MEMS are conventionally fabricated using single crystal silicon (c-Si). It is used as a platform to build as well as combine various MEMS components shown in figure 1.1. Si is advantageous due to its thermal and mechanical stability, well-developed fabrication techniques (acquired from the microelectronics industry), and ease of integration with electronics [5,9]. However, apart from Si, a number of other materials such as Si compounds (SiO_2 , Si_3N_4 , SiC), polysilicon, conductive polymers, GaAs, biological elements, are also explored for realizing MEMS components [6].

MEMS are conventionally fabricated using two methods namely, bulk and surface micromachining techniques. Bulk micro-manufacturing involves the removal of materials from bulk substrates to achieve the desired 3-D geometry of the microstructures whereas surface micromachining involves building the structure by adding materials layer by layer on top of the substrate. The basic processes involved in both these techniques include, i) Lithography, ii) Deposition, iii) Oxidation / diffusion, iv) Etching and v) Dicing and Packaging [2,3]. Figure 1.2 summarizes the typical flow of these processes.

Lithography is a process to transfer the desired micropattern onto the surface of a substrate. UV photolithography is one of the important and popular technique used for IC and MEMS fabrication, where micropatterns are transferred on photoresist (a photo-sensitive polymer) coated wafers, with good resolution. However, depending upon the required resolution, certain other lithography techniques such as laser lithography, imprint lithography, E-beam lithography, X-ray lithography, and Ion-beam lithography are also

commonly used in the fabrication of MEMS / NEMS devices [10,11]. Deposition is another vital process in MEMS fabrication to deposit foreign metals, organic materials, metal-oxides, etc on the surface of the base substrate. The widely used deposition techniques in MEMS are Chemical Vapour Deposition (CVD), sputtering and

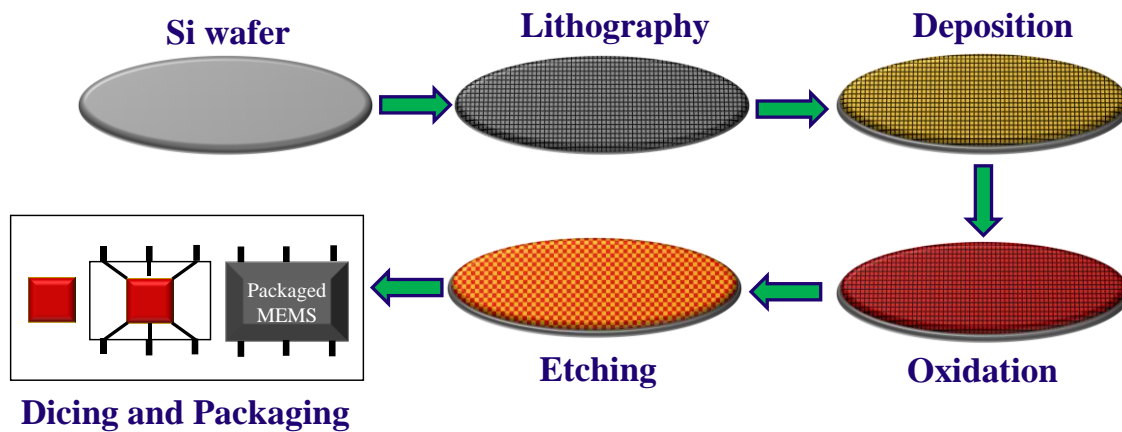


Figure 1.2. Schematic showing an overview of general processes involved in the microfabrication of a MEMS device.

pulsed laser deposition. Oxidation/diffusion is an important process used mainly for generating thermal/ electric insulation, as etch stop/masking layers, and for defining piezo resistive elements in MEMS devices. SiO_2 is a popular material for these purposes and is generally grown by thermal oxidation of the Si wafer. Etching is the process for releasing the desired 3-D microstructures by selectively removing the underlying substrate using either energy plasma (dry etching) or chemical solvents (wet etching). Once the devices are released, it is important to dice and package them for providing mechanical protection, thermal management, efficient interface with the external environment (for sensing), hermetic sealing (ex. Accelerometers), and complex electrical and signal interconnections.

1.2. Introduction to microcantilever based sensors

Microcantilevers (MCs) are the simplest MEMS structures and can be visualized as miniaturized fixed-free beams. They are capable of measuring ultra-small

displacements (10^{-12} m) [12,13], masses (\sim zg) [14,15], surface stresses (μ N/m) [13] and can detect IR/UV photons [16,17], when integrated with a suitable readout technique. Due to this versatility, MCs are extensively studied for a wide variety of applications in recent times, which include environmental monitoring, thermal and gravimetric sensing, explosive detection, point of care diagnostics, therapeutic drug delivery systems, etc [13]. MCs are also explored as fundamental research tools as they offer the possibility of measuring the phenomena that are otherwise very difficult by conventional methods. For example, Allocca et al. [18] studied the Casimir force across a Lifshitz transition in a spin-orbit-coupled material using a metal-coated sphere suspended from a MC. Similarly, Etayash et al. [19] demonstrated the real-time detection of bacteria and their interactions with antibiotics using a bi-material MC with an embedded microfluidic channel.

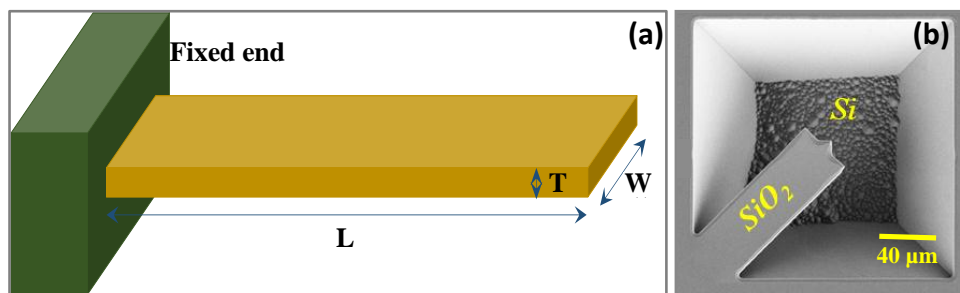


Figure 1.3. (a) Schematic of a MC where, L , W and T stands for its length, width and thickness, respectively. (b) A typical FESEM image of a released MC structure.

Fig 1.3 shows the schematic of a MC and a typical FESEM image of the MC structure. Typical dimensions of an MC are in the order of $100 \mu\text{m}$ (L) \times $10 \mu\text{m}$ (W) \times $1 \mu\text{m}$ (T). Depending on the measured parameter i.e., deflection or resonance frequency shift, MCs are usually operated either in static or dynamic mode and are discussed in more detail now.

1.2.1. Modes of operation

MCs are usually operated either in static or dynamic mode. In static mode, typically one side of the MC is rendered sensitive to a specific target molecule, physically [20] or chemically [21], while the opposite surface is passivated. When target molecules interact with the sensitized surface of the MC, differential surface stress is generated, resulting in a measurable mechanical deflection of the MC as shown in figure 1.4 (a). The magnitude of bending amplitude is dictated by the change in surface stress and the spring constant of the MC used. Therefore, chemical or physical modification of the MC surface and optimization of physical dimensions of MCs that could generate significant changes in surface stress and spring constant are studied extensively [22,23]. When MCs are coated with metallic thin films, they undergo deformation when subjected to temperature changes due to the difference in thermal expansion coefficients of MC material and the metal layer. This effect can be used for ultrasensitive temperature measurements [24,25] and the associated phase changes in very small amount of samples [26,27].

In dynamic mode, MCs act essentially as mechanical oscillators, whose resonance frequency depend on the added mass and the viscoelastic properties of the medium (see figure 1.4 (b)). For instance, adsorption of analytes onto a resonating MC results in lowering of its resonance frequency. Similarly, resonance frequency of the MCs is known to increase with decreasing density and viscosity of the surrounding fluid [13]. The sensitivity of the MCs for mass sensing can be enhanced by reducing their physical dimensions. Therefore, by scaling the dimensions of MCs to nanometer zepto gram (zg) mass sensitivities are demonstrated [14].

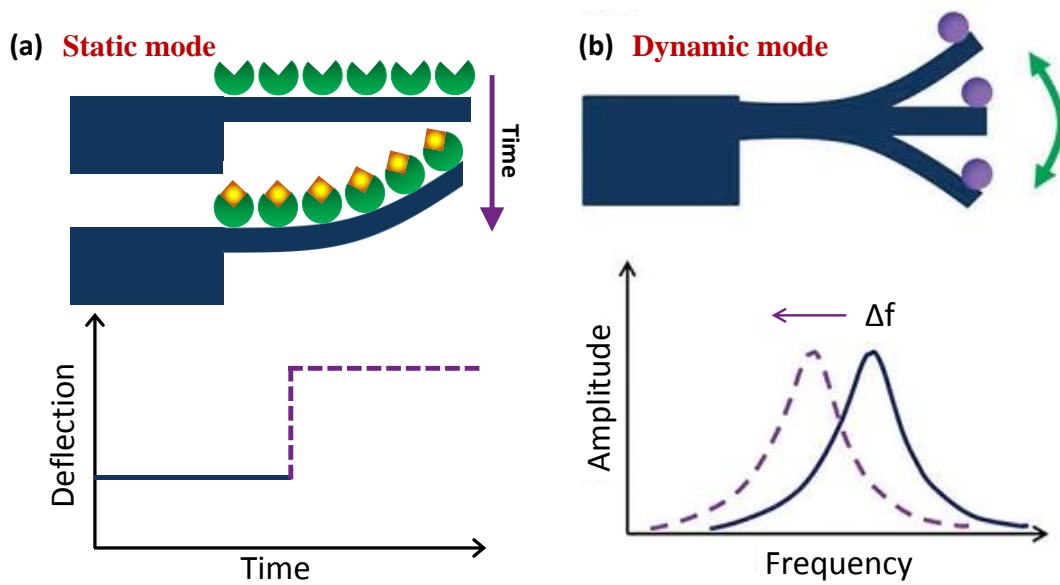


Figure 1.4. Schematic of MC working modes. **(a)** In static mode, one face is usually functionalized (🍀) and the deflection of MCs due to surface stress change when analytes (🔷) adsorb, is measured. **(b)** In dynamic mode, the MCs are usually operated at its resonance frequency and the shift in resonance due to added analytes (🟡) is measured. This image is adapted from reference [28].

1.2.2. Materials and microfabrication

MCs, like any other MEMS, are typically fabricated using Si and/or Si-based materials such as SiO₂, Si₃N₄, and SiC [13]. Apart from Si, polymer materials such as polyaniline [31], polystyrene [32], polyethylene terephthalate [33] are also explored in recent times. The greatest advantage of polymers over Si-based materials is their enhanced bending sensitivity owing to their lower Young's modulus E ($E_{\text{polymer}} = 0.7 - 8 \text{ GPa} \ll E_{\text{Si}} = 160 \text{ GPa}$) [1]. However, there are certain limitations while using polymers MCs for real-time applications such as low thermal and temporal stability, reduced optical reflectivity, moisture adsorption in liquids, or degassing in vacuum, which introduces drift in the final measurement [13]. Apart from Si and polymer-based materials, several other materials such as GaAs, AlN are also explored for MC fabrication depending upon the intended application [30,34].

Fabrication of MCs generally involves patterning the wafers using photolithography and releasing the free-standing MCs by dry/wet etching methods using bulk or surface micromachining techniques. A typical strategy for realization of silicon-based MCs through bulk micromachining consists of four main steps [13]: (a) substrate preparation involving the deposition of actual MC material, (b) MC pattern transfer on the front side by photolithography, (c) Etching the Si substrate from the backside till etch stop layer (usually SiO₂ layer on Si substrate) and (d) Releasing the MC by removing the etch stop layer. In contrast to this, the surface micromachining technique involves the deposition of a sacrificial layer on a Si Substrate followed by the deposition of structural material such as SiC or poly-Si using CVD techniques. Deposition parameters are optimized to reduce the residual stress in the film and followed by this, required MC structures are patterned on the film using lithography techniques. The lithography step is repeated on the bottom surface of the wafer for anisotropic bulk etching of Si. Followed by this, the sacrificial layer is removed to release the free-standing MCs. It may be noted, in surface micromachining, Si wafer acts only as a support layer and the free-standing MC is fabricated by depositing and releasing the thin film layers over Si. In the present thesis, SiO₂ MCs are fabricated using bulk micromachining method and is discussed in detail in chapter 3.

Apart from the conventional methods, some interesting alternatives such as thermoplastic injection molding [35], microstereolithography [36], and screen printing [37] are also studied in the literature for MC fabrication. It may be noted, details of MC design, the material used, and the fabrication methodology are largely dictated by the envisaged application, mode of operation, and readout technique intended.

1.2.3. Excitation and read-out methods

Excitation of the MCs can be realized by a variety of techniques depending upon the MC design and its intended application. Some of the popular excitation methods are piezoelectric, electromagnetic, capacitive (electrostatic), and electro/photothermal methods [13,38]. Piezoelectric excitation is the most common type of excitation method where the MCs are placed on a piezo actuator, which in turn is driven by a function generator. Piezoelectric actuators can also be miniaturized and integrated with MCs. Electromagnetic excitation is another form of excitation where the MCs are excited by the external magnetic field either by the formation of a conductive loop to pass current through the MCs (using Lorentz force) or by depositing a layer of magnetic material on the MC. In the electrostatic excitation method, there exist two electrodes of which the MC itself acts as one of the electrodes and the other electrode is kept at the proximity of the MC. When an alternating voltage is given across these electrodes a periodic force is exerted on the MC, thereby actuating it. In electrothermal excitation, the basic transduction element is a resistive heater, which is embedded on the surface of the MCs. Photothermal excitation is one of the recently developed excitation methods where a modulated low power laser beam is irradiated on the fixed end of an MC [39]. The excitation is achieved by induced thermal stress on the MC surface due to the irradiated laser beam.

To detect the nanomechanical deflection/change in the resonance frequency of MCs with sufficient precision, many read-out techniques using optical, piezoresistive, piezoelectric, capacitive, tunneling, and hard contact methods are developed. Among these, optical read-out method is the most popular owing to its simplicity and linear response over a wide range with sub-angstrom resolution [13]. In this method, a low power laser is focused on the MC surface and the reflected light is detected by a four-quadrant position-sensitive detector (PSD) (see figure 1.5 (a)) whose output is calibrated for MC

deflection. Apart from the laser-photodiode method, other optical techniques such as white light interferometry, Laser Doppler Vibrometry is also extensively used for MC deflection measurements. With suitable optics, these methods can be used for 2D mapping and real-time monitoring of MC deflection profiles. However, optical methods are difficult to apply for a large array of MCs and are known to introduce artefacts in liquid environments.

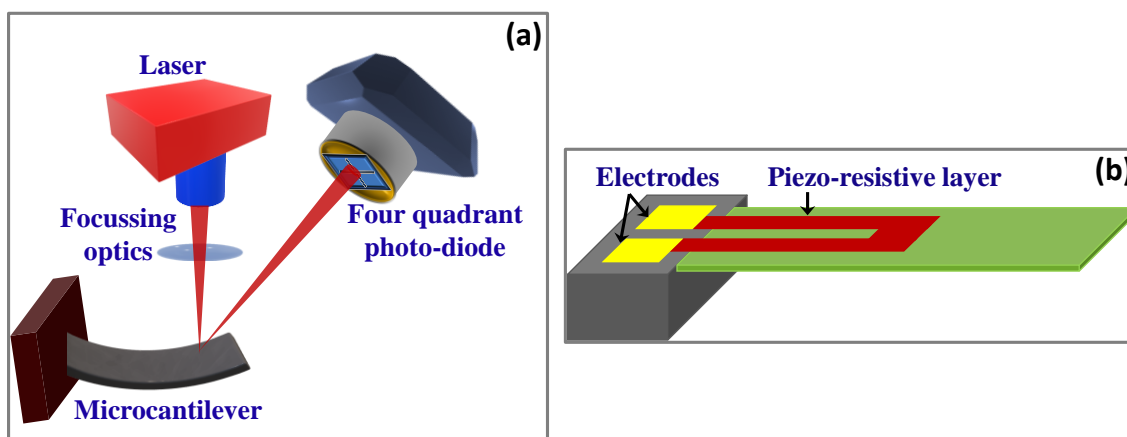


Figure 1.5. Schematic of a (a) typical optical read-out method where the deflection of the MC is detected by a laser and photo-diode arrangement and (b) piezoresistive MC with embedded piezoresistors (at the fixed end) along with contact pads for electrical output.

Piezo-resistivity is the property of change in resistivity of a material due to the applied stress. In piezoresistive method, piezoresistors are typically embedded on the MC surface (at the fixed end) as shown in figure 1.5 (b). When the MC deflects due to adsorption of the analyte or due to change in bulk stress, the corresponding change in the piezoresistance gives the measure of MC deflection [38,40]. Usually, piezoresistive MCs are implemented along with a reference MC by connecting them in a Wheatstone bridge configuration, to cancel out the noise in the measurement. One of the greatest advantages of piezoresistive method is that it is easy to integrate with readout electronics and can be applied for a large array of MCs simultaneously. Moreover, it suits well for measuring both static deflection and resonance frequency of the MC in both gaseous and liquid media.

1.2.4. Microcantilever theory

In this section, basic equations governing the static and dynamic modes of operation of MCs are derived. For static mode, Stoney's equation relating differential surface stress to MC deflection is presented, while the Euler-Bernoulli beam equation is derived for dynamic mode.

1.2.4.1. Stoney's equation

When adsorption on the MC surface is constrained to one side, differential surface stress is generated and as a consequence, MC undergoes deflection, which can be accurately predicted using Stoney's equation [41]. The displacement (U) at the free end of the MC in the y -direction with respect to the x -axis is shown in figure 1.6. The resulting curvature ' K ' with respect to origin ' O ' at distance x from the y -axis can be expressed as,

$$K = \frac{1}{R} = \frac{\frac{d^2U}{dx^2}}{\left\{1 + \left(\frac{dU}{dx}\right)^2\right\}^{\frac{3}{2}}} \quad (1.1)$$

where R is radius of curvature and by neglecting $(dU/dx)^2$ ($\ll 1$), Eq. (1.1) reduces to,

$$K = \frac{1}{R} = \frac{d^2U}{dx^2} \quad (1.2)$$

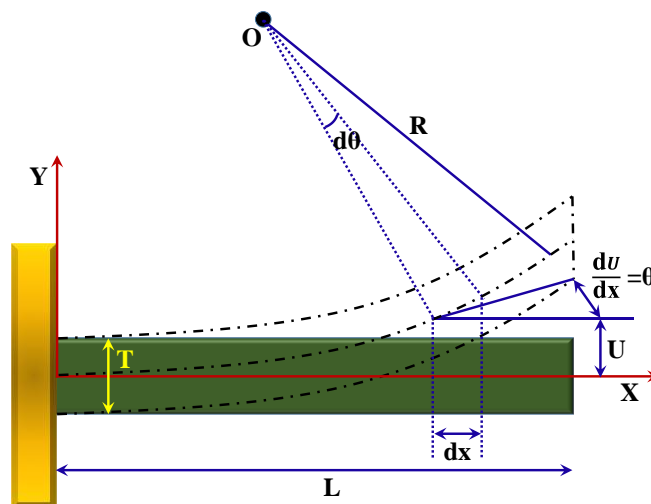


Figure 1.6. Schematic of MC relating the radius of curvature R to its deflection.

From Eq. (1.2) one can infer that the curvature of MC depends on the rate at which the slope changes along the axis of the beam. From Hooke's law, it is known that when the bending moment is loaded onto the MC it causes compression on one surface and expansion on the other. From the linear bending moment-curvature relationship we obtain,

$$K = \frac{1}{R} = \frac{M}{EI} \quad (1.3)$$

where M is the bending moment, E is the Young's Modulus, and $I = \frac{WT^3}{12}$ is the geometric moment of inertia of the cross-section. By combining Eqs. (1.2) and (1.3), we get,

$$K = \frac{1}{R} = \frac{d^2U}{dx^2} = \frac{M}{EI} \quad (1.4)$$

From figure 1.6, we know that $\frac{dU}{dx} = \theta$ (deflection angle). Now by integrating and solving equation 1.4 we get the deflection angle and deflection as,

$$\theta = \frac{Mx}{EI} \quad (1.5)$$

$$U = \frac{Mx^2}{2EI} \quad (1.6)$$

If the MC is functionalized on one side and exposed to analytes, then the surface interactions and the corresponding mechanical bending response will be different on this surface when compared to other side. This results in differential surface stress $\Delta\sigma$ ($= \sigma_1 - \sigma_2$, where σ_1 and σ_2 are the surface stress on top and bottom faces of MC, respectively) inducing a bending moment given by,

$$M = \frac{WT}{2} \Delta\sigma \quad (1.7)$$

By inserting Eq. (1.7) in eq. (1.4) we get the Stoney's relation as,

$$\frac{1}{R} = \frac{6\Delta\sigma}{ET^2} \quad (1.8)$$

As surface stress is isotropic, E has to be substituted with $E/(1-\nu)$, where ν is the Poisson's ratio of the film, leading to modified Stoney's relation,

$$\frac{1}{R} = \frac{6\Delta\sigma(1-\nu)}{ET^2} \quad (1.9)$$

Now, the MC deflection (Δz) can be estimated using the above equation, as it is related to the curvature by the equation, $\Delta z = \frac{L^2}{2R}$ [42] as,

$$\Delta z = \frac{3L^2(1-\nu)}{ET^2} \Delta\sigma \quad (1.10)$$

From this equation, it is evident that, for the increased surface stress sensitivity, the MC should be as thin and as long as possible. It is also inferred that the induced surface stress change could be positive or negative. Considering the adsorbed analytes as a uniform film over the MC surface, an expansion of the film results in downward bending of the MC to balance the stress. The resulting stress in the thin film is called compressive stress whereas the stress on the top face of the MC is said to be tensile. For a contracting film, the MC bends upwards and the stress in the thin film is called tensile stress [13].

It may be noted, the original Stoney's equation was derived for thin plates that are not clamped along the edges. Since MCs are rigidly clamped at one end, estimation of surface stress using Stoney's equation introduces certain errors [43,44]. Interestingly, the clamping effect on the deformation of MCs plays a vital role in understanding the effect of surface stress and/or fabrication induced curvature on the resonance frequency of MCs [45,46] and is not completely understood. In the present work, we have experimentally studied the effect of fabrication induced curvature vis-à-vis MC physical dimensions on the resonance frequency of SiO₂ MCs.

1.2.4.2. Expression for resonance frequency of MCs

For a rectangular MC with physical dimensions Length L, width W, and thickness T, neglecting shear deformation and rotational inertia, the equation of motion is given by Euler-Bernoulli beam equation [13],

$$\frac{\partial^2 U(y, t)}{\partial t^2} \rho \gamma + \frac{\partial^4 U(y, t)}{\partial y^4} EI = 0 \quad (1.11)$$

where, $U(y,t)$ is the displacement in the y-direction, ρ is the mass density, $\gamma=WT$ is the cross-sectional area, E is Young's modulus and $I (= WT^3/12)$ is the geometric moment of inertia. An ideal MC is fixed at one and free at the other, which means at the fixed end both deflection and slope are zero and at the free end both shear force and bending moments are zero, which fixes the initial boundary condition for an MC to be,

$$U = 0, \quad \frac{\partial U}{\partial y} = 0 \quad \text{at the fixed end of MC} \quad (1.12)$$

$$\frac{\partial^2 U}{\partial y^2} = 0, \quad \frac{\partial^3 U}{\partial y^3} = 0 \quad \text{at the free end of MC} \quad (1.13)$$

Using the above boundary conditions, the solution to equation (1.11) is harmonic that can be separated into a position-dependent and time-dependent terms using the variable separable method as, $U(y,t)= U_n(z)\Psi(t)$. By substituting $U(z,t)$ in equation (1.11), we get,

$$\frac{\partial^4 U(y, t)}{\partial y^4} = \alpha^4 U(y, t) \quad \text{where, } \alpha^4 = \frac{\omega_n^2 \rho \gamma}{EI} \quad (1.14)$$

where ω_n is the frequency of motion and n denotes the modal number. The solutions to this simplified beam equation can be written in the form,

$$U_n(z) = A_n(\cos(\alpha_n y) - \cosh(\alpha_n y)) + B_n(\sin(\alpha_n y) - \sinh(\alpha_n y)) \quad (1.15.1)$$

$$\Psi(t) = C_1 \cos \omega t + C_2 \sin \omega t \quad (1.15.2)$$

The modal constants in eq. (1.15.1) can be determined from the boundary conditions. For MCs, the characteristic frequency equation is hence given by,

$$1 + \cos(\alpha_n L) \cosh(\alpha_n L) = 0 \quad (1.16)$$

The solutions for $n = 1, 2, 3, \dots$ are $\lambda_n = \alpha_n L = 1.875, 4.6941, 7.8548, \dots, (2n-1)\pi/2$, respectively, implying that the beam will have quantized vibrational modes with a distinct shape. The number of nodal points increases with increasing mode number. The general expression of the n^{th} mode resonance of the beam, f_n is given by,

$$f_n = \frac{1}{2\pi} \frac{\lambda_n^2}{L^2} \sqrt{\frac{EI}{\rho\gamma}} = \frac{1}{2\pi} \frac{\lambda_n^2}{2\sqrt{3}L^2} \frac{T}{\sqrt{\rho}} \quad (1.17)$$

Equation 1.17 can be rewritten similar to a simple harmonic oscillator as,

$$f_1 = \frac{1}{2\pi} \sqrt{\frac{k_f}{m^*}} \quad (1.18)$$

where, k_f and m^* are the effective stiffness and effective mass of the MCs. For the longitudinal fundamental mode, k_f and m^* are given by,

$$k_f = \frac{ET^3W}{4L^3}, \quad m^* = 0.24m_0 \text{ where } m_0 = \rho\gamma L \quad (1.19)$$

When mass (Δm) is added uniformly on the surface of MC (like adsorption of water molecules), its resonance frequency will shift to

$$f_2 = \frac{1}{2\pi} \sqrt{\frac{k_f}{m^* + \Delta m^*}} = \frac{1}{2\pi} \sqrt{\frac{k_f}{m^* + (n\Delta m)}} \quad (1.20)$$

where 'n' is a mode-dependent geometric factor which is 0.24 for a rectangular MC in fundamental mode. By squaring the reciprocals of equations (1.18) and (1.20) and subtracting them, we can estimate the added mass using,

$$\Delta m = \frac{-k}{4\pi^2 n} \left[\frac{1}{f_1^2} - \frac{1}{f_2^2} \right] \quad (1.21)$$

From this equation, the amount of added mass can be estimated. It may be noted in this estimation, it is assumed that $\Delta m \ll m^*$ and change in effective stiffness of MC during adsorption is negligible.

Mass sensitivity (S) of an MC, when used as a mass sensor, can be obtained by differentiating Eq. (1.18) w.r.t. 'm', and is given by.

$$S = \frac{\Delta f_1}{\Delta m} \approx \frac{\partial f_1}{\partial m} = -\frac{f_1}{2m} \quad (1.22)$$

where, the influence of added mass on the stiffness of the MC is neglected. Similarly, the resolution (the smallest detectable mass of the sensor), Δm_m , is given by the smallest detectable frequency change Δf_m times the inverse sensitivity of the sensor,

$$\Delta m_m = S^{-1} \Delta f_m \quad (1.23)$$

From these equations, it is clear that mass sensitivity is directly proportional to resonance frequency and the interest is to reach maximum sensitivity and resolution. However, these parameters are also dependent on the Quality factor of the sensor.

1.2.4.3. Energy dissipation in MCs - Quality Factor

When MCs are vibrating in fluid environments, part of their energy is always dissipated into the surrounding fluid, in the form of thermal energy. This dissipation is related to inelastic phenomena in solids and viscosity of the fluids in which the MCs are immersed. The Quality factor (Q-factor) is the measure of this energy dissipation in MCs and is defined as the total energy lost per cycle of MC vibration [13,47], given by

$$Q = \frac{2\pi W_0}{\Delta W_0} \quad (1.24)$$

where W_0 and ΔW_0 are the mechanical energy stored and dissipated per vibration cycle of MC. Dissipation could be due to either intrinsic process in the MCs (phonon–phonon interactions, phonon–electron interactions, thermo-elastic damping, anchor losses) or could be due to extrinsic processes (interactions with the surrounding media) [13]. The total dissipation (Q_t) is determined by adding the contributions from all these processes given as,

$$\frac{1}{Q_t} = \frac{1}{Q_i} + \frac{1}{Q_e} \quad (1.25)$$

where, Q_i and Q_e are the Q-factors due to internal and external dissipation mechanisms, respectively. The external dissipation could be mainly caused by the viscosity of the surrounding medium and if the viscosity of the surrounding fluid is more, the Q-factor of the MC is low. This implies that the Q-factor is highly dependent on the pressure (P) in which the MCs are operated and that the Q-factor scales as $1/\sqrt{P}$ at higher pressures (continuum regime, $10^3 - 10^5$ Pa), as $1/P$ in the molecular regime ($10^1 - 10^3$ Pa) and is independent of pressure in the free molecular regime ($10^{-2} - 10^1$ Pa) [48]. Some of the other dissipation mechanisms arise due to clamping, surface, and material (due to internal frictions) losses. The material loss becomes dominant when there is more number of coating layers on the MC. Clamping losses could be minimized by using MCs with high length to width and width to thickness aspect ratios [13]. The Q-factors of a rectangular MC in air lie typically in the range of 10 – 1000 and ~10 in liquid [48].

Q-factor is inversely proportional to the damping coefficient and it is an important characteristic of MCs operating both in static and dynamic modes. Experimentally, the Q-

factor can be estimated from the measured resonance spectrum as the ratio of fundamental resonance frequency f_0 and its bandwidth (Δf_0), given by,

$$Q = \frac{f_0}{\Delta f_0} \quad (1.26)$$

where, Δf_0 is the full width at half maximum (FWHM) and full width at $\sqrt{2}$ times the maximum amplitude for energy and deflection measurements, respectively.

The Q-factor determines the resolution (the minimum detectable change in resonance frequency) of the MCs when used as sensors. Higher the Q-factor, higher is its resolution. In the present work, the variation of Q-factor of SiO₂ during adsorption and desorption of water molecules under ambient conditions is studied.

1.3. Brief literature survey on SiO₂ Microcantilevers

MCs made of elastic material with smaller spring constant such as silicon dioxide (SiO₂), can provide larger mechanical sensitivity i.e. bending amplitude under the same experimental conditions as compared to conventional Si or Si₃N₄ MCs [49]. The Young's modulus of SiO₂ is ~70 GPa, which is smaller than the Si (100) at 160 GPa or Si₃N₄ at 323 GPa [50]. Although other materials like polymers with still lower Young's modulus can be used, SiO₂ is of special importance for the MC based sensors, because of its compatibility with Si microfabrication and its capability to form silane-based self-assembled films [51]. Moreover, SiO₂ MCs can be used for ultrahigh sensitive Relative Humidity (RH) sensing [52] without any functionalization because of the presence of the hydroxyl groups on their surface which facilitates the water molecule adsorption through hydrogen bonding [53]. The greatest advantage of these sensors is that these are compatible with the current microelectronics industry and can easily be integrated with readout electronics. Taking these advantages into consideration, several studies are

reported in the literature, where SiO₂ MCs are explored for various sensing applications. For example, Tang et al. [54] studied the detection of femtomolar concentrations of HF using SiO₂ MC and demonstrated that its sensitivity is higher than that of its Si counterpart. In yet another study [55], they reported two order higher deflection, for a given concentration of aminoethanethiol, and attributed it to the lower spring constant of the SiO₂ MCs. Li et al. [56] successfully fabricated piezoresistive SiO₂ MCs for the detection of various gases like NH₃, dimethyl methylphosphonate (DMMP), and trinitrotoluene (TNT) [57] with a suitable self-assembled monolayer (SAM) on their surface. Recently, Abdollahi et al. [58] fabricated Al/SiO₂ bilayer MCs for IR detection and estimated the thermo-mechanical response of these detectors from finite element method simulations. Interestingly, resonance frequency measurements on successfully released SiO₂ MCs were used to estimate the material properties of the SiO₂ film itself, such as Young's modulus, yield strength, Poisson's ratio [59], residual stress [60] and thermal expansion coefficient [61]. In the present thesis, SiO₂ MCs are explored for ultrasensitive and ultrafast RH sensing and real-time human respiration monitoring.

1.4. Influence of functionalization and surface modifications on MC response

MCs are usually coated with a thin film layer on their surface in order to enhance the sensitivity and selectivity, both in static and dynamic modes. In static mode, typically Au or a polymer film is coated on one of the sides, to generate differential surface stress when exposed to analytes, resulting in measurable bending. Typically, Au coating will be functionalized with thiol-based chemistry to improve the molecular binding and therefore extensively studied for highly sensitive and selective detection of biomolecules such as proteins and DNA [62]. MCs are also functionalized with SAMs on one of their faces, for detecting explosives [63], volatile organic compounds (VOCs) [64], and e-nose

applications [65]. However, Au coating on the MC surface is known to introduce drift in the sensor output response. Also, morphology and grain size of the Au can influence the surface stress generated during self-assembly of thiolated alkane chains [66]. Similarly, polymer coating deteriorates the response time of MCs, while exploring them for RH sensing applications [22,66]. In dynamic mode, frequency shift due to added mass is measured, and therefore both the sides of MCs can be functionalized. However, apart from the added mass, frequency shift could also be influenced by secondary effects such as analyte-induced coating stress/strain. In the case of polymer-coated MCs, the effect of the surrounding medium on the coating sorption properties such as the effect of fluid temperature on the polymer partition coefficient [67] can influence their dynamic response. Also, thermal drift in output signal can arise due to the temperature dependence of Young's modulus of the MC material.

Taking the above aspects into consideration, in recent times, uncoated MCs are explored for various sensing applications. Uncoated MCs are made of single layer (i.e. no metal or organic overlayer) and eliminates or significantly reduces several issues associated with coated MCs. For example, Lakshmoji et al. [20] showed that the uncoated Si MCs with different morphologies on two sides can be effectively used for sensing water molecules. Pinnaduwege et al. [68] studied the desorption characteristics of explosives and common non-explosive vapors using uncoated Si MCs and showed that uncoated MCs can differentiate between these two. However uncoated MCs are often non-selective and offer very low sensitivities. It is possible to improve the sensitivity of uncoated MCs either by optimizing their physical geometry or by introducing micro patterns/nanostructures on their surface (physical tailoring).

Improving the sensitivity by first method is straight forward, as sensitivity of MCs in dynamic mode is directly proportional to their resonance frequency and therefore can be improved either by increasing the stiffness or by reducing the effective mass. For example, Hong et al. [69], studied the effect of MC geometry (rectangle, triangle, and half-ellipse) with an innovative inner cut on their sensitivity. From their numerical analysis and experimental studies, they found that low-aspect-ratio MC with a high-aspect-ratio inner cut offers the highest sensitivity. Subramanian et al. [70] suggested the use of a nonlinear width profile for V-shaped MCs to increase the structural stiffness and subsequently the mass sensitivity. Similarly, Boudjiet et al. [71] used uncoated Si MCs and showed that wide and short rectangular uncoated MCs are more sensitive to changes in gas density (various concentrations of H₂/N₂ gas mixtures) than U- and T-shaped devices of the same overall dimensions. Prabakar et al. [72] demonstrated via FEM simulation studies that by introducing a step discontinuity across the length of the MCs, the mass sensitivity increases by two orders of magnitude and it depends on the position of step from free end, step thickness, and step width.

Second method of improving the sensitivity of uncoated MCs involves physically modifying their surface. For example, Nguyen Van Toan et al. [73] experimentally showed that the Si MCs with high aspect ratio Si nanopillars on their surface would improve the bending sensitivity during moisture adsorption. Stassi et al. [74] proved that the RH sensitivity could be enhanced by introducing mesoporous silica coating on c-Si MCs. Canavese et al. [75] studied the resonating behavior of nano-machined holed MCs and showed a 250% enhancement in mass sensitivity without altering other figure of merits of the sensor. Noyce et al. [76] fabricated high surface area MCs using carbon nanotube templated microfabrication technique and showed that their RH sensitivity is comparable to polymer-coated Si MCs without compromising the Q-factor. In order to increase the

sensitivity and selectivity of commercial MCs for detecting dimethyl methylphosphonate (DMMP), Lee et al. [77] used nanostructured (vertically oriented amorphous titanium dioxide nanotubes) MCs. A sensitive calorimetric sensor using uncoated TiO₂ MC with nanowell patterns on its surface was proposed by Lee et al. [77]. The thermomechanical sensitivity in these devices was found to originate from the structure-dependent variations in both the elastic modulus and thermal expansion coefficient of TiO₂ due to the presence of ordered nanowells. Nanoporous Aluminium oxide modified MCs are also studied in the literature for moisture [78,79] and CO₂ [80] sensing applications.

Interestingly, modification of the MC surface in itself can influence its dynamic characteristics [48,81–83]. For example, Ergincan et al. [81] studied the influence of surface roughness on the resonance frequency of the bi-material MCs and established the relation between the resonance frequency shift and roughness parameters along with material properties of the film and physical dimensions of the bare MC. In yet another study, these authors studied the effect of systematic surface modification on the quality factor of commercial MCs as a function of gas pressure and established a clear correlation between increasing surface area and decreasing Q-factor [82]. They extended their work on gold-coated MCs and showed that surface engineering offers a promising method to control and increase the Q factor up to 50% for operation in vacuum [82]. Duan et al. [83] in a recent study showed that the surface patterns/surface morphology can enhance, reduce or annul the effect of surface stress on the resonance frequency of the MCs depending upon their surface inclination angle and Poisson's ratio of the material under consideration.

From the foregoing literature scan, it is clear that surface modification has important implications on the sensitivity of MCs and it is imperative to understand the role of micro/nanopatterning on their characteristics. In the present thesis, SiO₂ MCs with

controlled micro-patterns are successfully fabricated and the role of micro-patterns on their static (initial bending) and dynamic (resonance frequency shift) characteristics are studied. It is shown that micro-patterned MCs can be effectively used for ultra-high sensitive RH sensing, without compromising their response times and hysteresis characteristics.

1.5. Motivation of the present thesis

The motivation of the present thesis are,

1. To optimize various process parameters to release SiO₂ MCs of various dimensions using DLW and wet chemical etching methods.
2. To understand the role of biaxial curvature inherently present in SiO₂ MCs on their resonance frequency.
3. To study the effect of post-release high-temperature annealing on the residual stress evolution in SiO₂ MCs.
4. To test the RH sensitivity of as-fabricated SiO₂ MCs and explore the possibility of enhancing the same by introducing controlled micro-patterns on the MC surface.

The detailed objectives along with the methodology adopted to achieve them are given below.

1.5.1. Fabrication and characterization of SiO₂ MCs

SiO₂ MCs are generally fabricated using SiO₂/Si wafers in two steps. Initially, MC patterns are transferred on the wafer using UV lithography and is followed by wet/dry etching of underlying Si to release the MCs. However, UV lithography suffers from limitations such as the requirement of a pre-fabricated Chrome mask and lack of flexibility of the mask design. Direct laser writing is an alternative patterning method that circumvents the above issues and is emerging as an interesting new technology for

micro/nanofabrication. However, for effective pattern transfer using DLW, various process parameters need to be optimized. Similarly, once the desired pattern is transferred on the photoresist and subsequently on to the SiO₂ satisfactorily, SiO₂ MCs are typically released by etching the underlying c-Si by wet chemicals. During the wet chemical etching process, the released devices usually stick to the underlying Si substrate, making the device unusable. Therefore, it is also important to figure out innovative methods to avoid stiction and improve the yield of successfully released MCs by wet chemical etching methods. These two issues are addressed in Chapter 3 of the thesis. Optimization of various microfabrication process parameters is carried out for the successful release of SiO₂ MCs, such as laser dose (in DLW), pre- and post-baking temperature values, etc. It is shown that even for fabricating simple structures like MCs, DLW can be a valuable tool, if optimizations at the design level are desired. An innovative two-step method to avoid stiction in SiO₂ MCs by introduction of a sharp convex tip at the free end of the MC along with a post-etch rinsing in boiling DI water while releasing them using wet chemicals, is proposed. It is shown that the stiction is substantially reduced, even in the longest MCs (L = 330 μm) studied in the present work.

1.5.2. Effect of biaxial curvature on the resonance frequency and high-temperature annealing on the bending properties of SiO₂ MCs

SiO₂ MCs released by wet chemical etching method are usually bent away from the wafer due to the presence of residual stress in SiO₂ film. Presence of curvature in MCs induces certain artefacts such as initial bending (in static mode) and stiffness changes (dynamic mode) when exploring them for sensing applications.

Therefore, in Chapter 4, as a prelude to RH sensing experiments, i) the effect of fabrication induced biaxial curvature on the resonance frequency and ii) the role of high-

temperature annealing on the residual stress evolution of uncoated SiO₂ MCs, are studied. Resonance frequencies of the released MCs were measured using Laser Doppler Vibrometer (LDV) and compared with finite element modeling (FEM) simulation results. The difference between the experimental and FEM simulated values is attributed to the presence of biaxial curvature in these MCs. The curvature present in the MCs was measured independently using a 3D OM. The role of MC dimensions vis-à-vis curvature on the observed frequency shift is discussed in detail. Similarly, the effect of post-release high-temperature annealing (800 °C and 1000°C) in different environments (O₂ and N₂) and temperature on the residual stress evolution of SiO₂ MCs are presented. From these studies, the optimum physical dimensions of the MC to be used for sensing studies are identified.

1.5.3. RH sensing studies using SiO₂ MCs

For RH sensing application, MCs are usually coated with a moisture-sensitive layer such as metal oxides, organic polymers, or hybrid composite materials, on their surface whose purpose is to selectively adsorb the water molecules [84]. Subsequently, the adsorption of water molecules on the MC surface increases the effective mass and results in a resonance frequency shift. Interestingly, SiO₂ MCs can be used for RH sensing without any functionalization because of the presence of the hydroxyl groups on their surface which facilitates the water molecule adsorption through hydrogen bonding [53]. This was verified in Chapter 5, where it is shown that the as-fabricated SiO₂ MCs can indeed be used for RH sensing with good sensitivity and resolution.

An innovative method is proposed to enhance the RH sensitivity of as-fabricated SiO₂ MCs. It is shown that the introduction of controlled micro-patterns on their surface will enhance the RH sensitivity without compromising other crucial characteristics. The

reason for the enhanced RH sensitivity of micropatterned MCs when compared to unpatterned ones is attributed to the formation of *gel-like* water layers inside the cavities which facilitate the enhanced uptake of water molecules. Finally, real-time monitoring of human respiration during normal and slow inhale/exhale breathing cycles is demonstrated using micropatterned MCs.

1.6. References

- [1] M.J. Madou, Solid-State Physics, Fluidics, and Analytical Techniques in Micro- and Nanotechnology, CRC Press, Cambridge, 2011.
- [2] M.J. Madou, From MEMS to Bio-MEMS and Bio-NEMS, CRC Press, 2011.
- [3] T.-R. Hsu, MEMS and microsystems: design and manufacture, Tat McGraw Hill 2002.
- [4] O. Brand, I. Dufour, S.M. Heinrich, F. Josse, Resonant MEMS: Principles, modeling, implementation, and applications, 2015.
- [5] J.P. Seymour, F. Wu, K.D. Wise, E. Yoon, State-of-the-art mems and microsystem tools for brain research, *Microsystems Nanoeng.* 3 (2017) 1–16.
- [6] M.I. Younis, MEMS Linear and Nonlinear Statics and Dynamics, Springer US, Boston, MA, 2011.
- [7] F. Ejeian, S. Azadi, A. Razmjou, Y. Orooji, A. Kottapalli, M. Ebrahimi Warkiani, M. Asadnia, Design and applications of MEMS flow sensors: A review, *Sensors Actuators, A Phys.* 295 (2019) 483–502.
- [8] S.. Senturia, *Microsystem Design*, Kluwer Academic Publishers, Boston, 2002.

- [9] Y. Xu, X. Hu, S. Kundu, A. Nag, N. Afsarimanesh, S. Sapra, S.C. Mukhopadhyay, T. Han, Silicon-based sensors for biomedical applications: A review, *Sensors (Switzerland)*. 19 (2019) 2908.
- [10] M.J. Madou, *Manufacturing Techniques for Microfabrication and Nanotechnology*, CRC Press, 2011.
- [11] T. Betancourt, L. Brannon-Peppas, Micro- and nanofabrication methods in nanotechnological medical and pharmaceutical devices, *Int. J. Nanomedicine*. 1 (2006) 483–495.
- [12] A. Boisen, T. Thundat, Design & fabrication of cantilever array biosensors, *Mater. Today*. 12 (2009) 32–38.
- [13] A. Boisen, S. Dohn, S.S. Keller, S. Schmid, M. Tenje, Cantilever-like micromechanical sensors, *Reports Prog. Phys.* 74 (2011) 036101.
- [14] T.P. Burg, M. Godin, S.M. Knudsen, W. Shen, G. Carlson, J.S. Foster, K. Babcock, S.R. Manalis, Weighing of biomolecules, single cells and single nanoparticles in fluid, *Nature*. 446 (2007) 1066–1069.
- [15] A.K. Naik, M.S. Hanay, W.K. Hiebert, X.L. Feng, M.L. Roukes, Towards single-molecule nanomechanical mass spectrometry, *Nat. Nanotechnol.* 4 (2009) 445–450.
- [16] M.R. Ramaiah, K. Prabakar, S.T. Sundari, S.K. Dhara, Wavelength dependence of photothermal deflection in Au/Si bimaterial microcantilevers, *Sensors Actuators A Phys.* (2020) 112233.
- [17] N. Gao, D. Zhao, R. Jia, D. Zhang, D. Liu, Plasmonic Microcantilever with Remarkably Enhanced Photothermal Responses, *Sci. Rep.* 7 (2017) 4796.

- [18] A.A. Allocca, J.H. Wilson, V. Galitski, Nonanalytic behavior of the Casimir force across a Lifshitz transition in a spin-orbit-coupled material, *Phys. Rev. B - Condens. Matter Mater. Phys.* 90 (2014) 075420.
- [19] H. Etayash, M.F. Khan, K. Kaur, T. Thundat, Microfluidic cantilever detects bacteria and measures their susceptibility to antibiotics in small confined volumes, *Nat. Commun.* 7 (2016) 12947.
- [20] K. Lakshmoji, K. Prabakar, S. Tripura Sundari, J. Jayapandian, A.K. Tyagi, C.S. Sundar, Origin of bending in uncoated microcantilever - Surface topography?, *Appl. Phys. Lett.* 104 (2014) 2–5.
- [21] R. Yang, X. Huang, Z. Wang, Y. Zhou, L. Liu, A chemisorption-based microcantilever chemical sensor for the detection of trimethylamine, *Sensors Actuators, B Chem.* 145 (2010) 474–479.
- [22] M. Godin, V. Tabard-Cossa, Y. Miyahara, T. Monga, P.J. Williams, L.Y. Beaulieu, R. Bruce Lennox, P. Grutter, Cantilever-based sensing: the origin of surface stress and optimization strategies, *Nanotechnology.* 21 (2010) 075501.
- [23] J. Mertens, M. Calleja, D. Ramos, A. Tarín, J. Tamayo, Role of the gold film nanostructure on the nanomechanical response of microcantilever sensors, *J. Appl. Phys.* 101 (2007).
- [24] L. Wu, T. Cheng, Q.C. Zhang, A bi-material microcantilever temperature sensor based on optical readout, *Meas. J. Int. Meas. Confed.* 45 (2012) 1801–1806.
- [25] A. Alodhayb, F. Khan, H. Etayash, T. Thundat, Review—Nanomechanical Calorimetric Infrared Spectroscopy using Bi-Material Microfluidic Cantilevers, *J. Electrochem. Soc.* 167 (2020) 037504.

- [26] A.P. Haring, M. Singh, M. Koh, E. Cesewski, D.A. Dillard, Z. “James” Kong, B.N. Johnson, Real-time characterization of hydrogel viscoelastic properties and sol-gel phase transitions using cantilever sensors, *J. Rheol. (N. Y. N. Y)*. 64 (2020) 837–850.
- [27] S.L. Biswal, D. Raorane, A. Chaiken, A. Majumdar, Using a Microcantilever Array for Detecting Phase Transitions and Stability of DNA, *Clin. Lab. Med.* 27 (2007) 163–171.
- [28] J. Tamayo, P.M. Kosaka, J.J. Ruz, Á. San Paulo, M. Calleja, Biosensors based on nanomechanical systems, *Chem. Soc. Rev.* 42 (2013) 1287–1311.
- [29] J. Tamayo, D. Ramos, J. Mertens, M. Calleja, Effect of the adsorbate stiffness on the resonance response of microcantilever sensors, *Appl. Phys. Lett.* 89 (2006) 2004–2007.
- [30] R.B. Karabalin, L.G. Villanueva, M.H. Matheny, J.E. Sader, M.L. Roukes, Stress-induced variations in the stiffness of micro- and nanocantilever beams, *Phys. Rev. Lett.* 108 (2012) 1–5.
- [31] C. Steffens, A. Manzoli, F.L. Leite, O. Fatibello, P.S.P. Herrmann, Atomic force microscope microcantilevers used as sensors for monitoring humidity, *Microelectron. Eng.* 113 (2014) 80–85.
- [32] R. Zhao, Y. Sun, Polymeric flexible immunosensor based on piezoresistive microcantilever with PEDOT/PSS conductive layer, *Sensors (Switzerland)*. 18 (2018) 451.
- [33] X.R. Zhang, X. Xu, Development of a biosensor based on laser-fabricated polymer microcantilevers, *Appl. Phys. Lett.* 85 (2004) 2423–2425.

- [34] H. Yamaguchi, GaAs-based micro/nanomechanical resonators, *Semicond. Sci. Technol.* 32 (2017) 103003.
- [35] Michelle Khine, C.-S. Chen, A. Grimes, D.N. Breslauer, L. Lee, M. Dunlap, A. Gopinathan, S. Ghosh, *Processes For Rapid Microfabrication Using Thermoplastics And Devices Thereof*, Pub No.: US 2017/0215756A1, 1(19) 2015 - 2018 (2017).
- [36] C. Credi, A. Fiorese, M. Tironi, R. Bernasconi, L. Magagnin, M. Levi, S. Turri, 3D Printing of Cantilever-Type Microstructures by Stereolithography of Ferromagnetic Photopolymers, *ACS Appl. Mater. Interfaces.* 8 (2016) 26332–26342.
- [37] J. Charmet, R. Rodrigues, E. Yildirim, P.K. Challa, B. Roberts, R. Dallmann, Y. Whulanza, Low-Cost microfabrication tool box, *Micromachines.* 11 (2020) 135.
- [38] J. Xu, M. Bertke, H.S. Wasisto, E. Peiner, Piezoresistive microcantilevers for humidity sensing, *J. Micromechanics Microengineering.* 29 (2019) 053003.
- [39] S. Kim, D. Lee, R. Thundat, M. Bagheri, S. Jeon, T. Thundat, Photothermal Cantilever Deflection Spectroscopy, *ECS Trans.* 50 (2013) 459–464.
- [40] J.Q. Huang, F. Li, M. Zhao, K. Wang, A surface micromachined CMOS MEMS humidity sensor, *Micromachines.* 6 (2015) 1569–1576.
- [41] D. Ramos, J. Mertens, M. Calleja, J. Tamayo, Study of the Origin of Bending Induced by Bimetallic Effect on Microcantilever, *Sensors.* 7 (2007) 1757–1765.
- [42] S.S. Rao, *Mechanical Vibrations (Fifth Edition)*, Pearson Education Inc., 2010.

- [43] V. Pini, J. Tamayo, E. Gil-Santos, D. Ramos, P. Kosaka, H.D. Tong, C. Van Rijn, M. Calleja, Shedding light on axial stress effect on resonance frequencies of nanocantilevers, *ACS Nano*. 5 (2011) 4269–4275.
- [44] J. Tamayo, V. Pini, P. Kosaka, N.F. Martinez, O. Ahumada, M. Calleja, Imaging the surface stress and vibration modes of a microcantilever by laser beam deflection microscopy, *Nanotechnology*. 23 (2012).
- [45] J.J. Ruz, V. Pini, O. Malvar, P.M. Kosaka, M. Calleja, J. Tamayo, Effect of surface stress induced curvature on the eigenfrequencies of microcantilever plates, *AIP Adv.* 8 (2018) 105213.
- [46] J. Tamayo, J.J. Ruz, V. Pini, P. Kosaka, M. Calleja, Quantification of the surface stress in microcantilever biosensors: Revisiting Stoneys equation, *Nanotechnology*. 23 (2012).
- [47] J.-H. Lee, S.-T. Lee, C.-M. Yao, W. Fang, Comments on the size effect on the microcantilever quality factor in free air space, *J. Micromech. Microeng.* J. Micromech. Microeng. 17 (2007) 139–146.
- [48] O. Ergincan, G. Palasantzas, B.J. Kooi, Viscous damping of microcantilevers with modified surfaces and geometries, *Appl. Phys. Lett.* 101 (2012).
- [49] Y. Tang, J. Fang, X. Yan, H.F. Ji, Fabrication and characterization of SiO₂ microcantilever for microsensor application, *Sensors Actuators, B Chem.* 97 (2004) 109–113.
- [50] M. J.Madou, *Fundamentals of Microfabrication and nanotechnology, volume I, "Solid-State Physics, Fluidics, and Analytical Techniques in Micro- and Nanotechnology"*, 2011.

- [51] S.R. Wasserman, Y.T. Tao, G.M. Whitesides, Structure and Reactivity of Alkylsiloxane Monolayers Formed by Reaction of Alkyltrichlorosilanes on Silicon Substrates, *Langmuir*. 5 (1989) 1074–1087.
- [52] Q. Chen, J. Fang, H. Ji, K. Varahramyan, Microfabrication and Characterization of SiO₂ Microcantilever for High Sensitive Moisture Sensor, (2007) 1436–1439.
- [53] P. Raghu, C. Yim, F. Shadman, E. Shero, Susceptibility of SiO₂, ZrO₂, and HfO₂ dielectrics to moisture contamination, *AIChE J.* 50 (2004) 1881–1888.
- [54] Y. Tang, J. Fang, X. Xu, H.F. Ji, G.M. Brown, T. Thundat, Detection of Femtomolar Concentrations of HF Using an SiO₂ Microcantilever, *Anal. Chem.* 76 (2004) 2478–2481.
- [55] Y. Tang, J. Fang, X. Yan, H.F. Ji, Fabrication and characterization of SiO₂ microcantilever for microsensor application, *Sensors Actuators, B Chem.* 97 (2004) 109–113.
- [56] P. Li, X. Li, A single-sided micromachined piezoresistive SiO₂ cantilever sensor for ultra-sensitive detection of gaseous chemicals, *J. Micromechanics Microengineering*. 16 (2006) 2539–2546.
- [57] P. Li, X. Li, G. Zuo, J. Liu, Y. Wang, M. Liu, D. Jin, Silicon dioxide microcantilever with piezoresistive element integrated for portable ultrasensitive gaseous detection, *Appl. Phys. Lett.* 89 (2006).
- [58] H. Abdollahi, H. Hajghassem, S. Mohajerzadeh, Simple fabrication of an uncooled Al/SiO₂ microcantilever IR detector based on bulk micromachining, *Microsyst. Technol.* 20 (2014) 387–396.

- [59] C.L. Dai, Y.M. Chang, A resonant method for determining mechanical properties of Si₃N₄ and SiO₂ thin films, *Mater. Lett.* 61 (2007) 3089–3092.
- [60] W. Fang, J.A. Wickert, Determining mean and gradient residual stresses in thin films using micromachined cantilevers, *J. Micromechanics Microengineering*. 6 (1996) 301–309.
- [61] C. Tsou, Y.S. Huang, H.C. Chang, On the Determination of Thermal Expansion Coefficient of Thermal Oxide, *Tech. Proc. 2005 NSTI Nanotechnol. Conf. Trade Show*. 3 (2005) 339–342.
- [62] R.M.R. Pinto, V. Chu, J.P. Conde, Label-Free Biosensing of DNA in Microfluidics using Amorphous Silicon Capacitive Micro-Cantilevers, *IEEE Sens. J.* 20 (2020) 1–1.
- [63] S.J. Patil, N. Duragkar, V.R. Rao, An ultra-sensitive piezoresistive polymer nano-composite microcantilever sensor electronic nose platform for explosive vapor detection, *Sensors Actuators B Chem.* 192 (2014) 444–451.
- [64] V. Seena, R.S. Dudhe, H.N. Raval, S. Patil, A. Kumar, S. Mukherji, V.R. Rao, Organic Sensor Platforms for Environmental and Security Applications, *ECS Trans.* 35 (2019) 67–77.
- [65] V.S. Palaparthi, S.N. Doddapujar, G. Gupta, P. Das, S.A. Chandorkar, S. Mukherji, M.S. Baghini, V.R. Rao, E-Nose: Multichannel Analog Signal Conditioning Circuit With Pattern Recognition for Explosive Sensing, *IEEE Sens. J.* 20 (2020) 1373–1382.

- [66] V. Tabard-Cossa, M. Godin, I.J. Burgess, T. Monga, R.B. Lennox, P. Grütter, Microcantilever-based sensors: Effect of morphology, adhesion, and cleanliness of the sensing surface on surface stress, *Anal. Chem.* 79 (2007) 8136–8143.
- [67] I. Dufour, F. Josse, S.M. Heinrich, C. Lucat, C. Ayela, F. Ménénil, O. Brand, Unconventional uses of microcantilevers as chemical sensors in gas and liquid media, *Sensors Actuators, B Chem.* 170 (2012) 115–121.
- [68] L.A. Pinnaduwege, V. Boiadjiev, J.E. Hawk, T. Thundat, Sensitive detection of plastic explosives with self-assembled monolayer-coated microcantilevers, *Appl. Phys. Lett.* 83 (2003) 1471–1473.
- [69] H. Hocheng, W.H. Weng, J.H. Chang, Shape effects of micromechanical cantilever sensor, *Meas. J. Int. Meas. Confed.* 45 (2012) 2081–2088.
- [70] S. Subramanian, N. Gupta, Improved V-shaped microcantilever width profile for sensing applications, *J. Phys. D. Appl. Phys.* 42 (2009) 185501.
- [71] M.T. Boudjiet, J. Bertrand, F. Mathieu, L. Nicu, L. Mazonq, T. Leichlé, S.M. Heinrich, C. Pellet, I. Dufour, Geometry optimization of uncoated silicon microcantilever-based gas density sensors, *Sensors Actuators, B Chem.* 208 (2015) 600–607.
- [72] K. Prabakar, J. Jayapandian, A.K. Tyagi, C.S. Sundar, B. Raj, Sensitivity of a nanocantilever-based mass sensor, *Nano.* 5 (2010) 25–30.
- [73] N. Van Toan, M. Toda, T. Hokama, T. Ono, Cantilever with High Aspect Ratio Nanopillars on Its Top Surface for Moisture Detection in Electronic Products, *Adv. Eng. Mater.* 19 (2017) 1–5.

- [74] S. Stassi, V. Cauda, S. Fiorilli, C. Ricciardi, Surface area enhancement by mesoporous silica deposition on microcantilever sensors for small molecule detection, *J. Mater. Chem. C*. 3 (2015) 12507–12513.
- [75] G. Canavese, S.L. Marasso, M. Quaglio, M. Cocuzza, C. Ricciardi, C.F. Pirri, Polymeric mask protection for alternative KOH silicon wet etching, *J. Micromechanics Microengineering*. 17 (2007) 1387–1393.
- [76] S.G. Noyce, R.R. Vanfleet, H.G. Craighead, R.C. Davis, High surface-area carbon microcantilevers, *Nanoscale Adv.* 1 (2019) 1148–1154.
- [77] D. Lee, S. Kim, I. Chae, S. Jeon, T. Thundat, Nanowell-patterned TiO₂ microcantilevers for calorimetric chemical sensing, *Appl. Phys. Lett.* 104 (2014) 141903.
- [78] O. Boytsova, A. Klimenko, V. Lebedev, A. Lukashin, A. Eliseev, Nanomechanical humidity detection through porous alumina cantilevers, *Beilstein J. Nanotechnol.* 6 (2015) 1332–1337.
- [79] P. Kapa, L. Pan, A. Bandhanadham, J. Fang, K. Varahramyan, W. Davis, H.F. Ji, Moisture measurement using porous aluminum oxide coated microcantilevers, *Sensors Actuators, B Chem.* 134 (2008) 390–395.
- [80] C. Yim, M. Lee, M. Yun, G. Kim, K.T. Kim, CO₂-Selective Nanoporous Metal-Organic Framework Microcantilevers, *Sci. Rep.* 5 (2015) 1–8.
- [81] O. Ergincan, G. Palasantzas, Influence of random roughness on cantilever resonance frequency, *Phys. Rev. B - Condens. Matter Mater. Phys.* 82 (2010) 155438.

- [82] O. Ergincan, G. Palasantzas, B.J. Kooi, Influence of surface modification on the quality factor of microresonators, *Phys. Rev. B.* 85 (2012) 205420.
- [83] H. Duan, Y. Xue, X. Yi, Vibration of cantilevers with rough surfaces, *Acta Mech. Solida Sin.* 22 (2009) 550–554.
- [84] J. Xu, M. Bertke, X. Li, A. Setiono, M. Fahrbach, A. Schmidt, E. Peiner, Silicon Microcantilevers with ZnO Nanorods/Chitosan-SAMs Hybrids on Its Back Surface for Humidity Sensing, *Proceedings.* 2 (2018) 838.

Chapter 2

Experimental methods

In this chapter, details about the various experimental setups used for microfabrication and characterization of SiO₂ MCs are given. The chapter begins with a brief description on the working principle of DLW and various processes carried out on a chemical wet bench. Followed by this, details about the experimental facilities used for characterization of MCs using 3D optical microscope, Nano Vibration Analyzer, Laser Doppler Vibrometer, and Atomic Force Microscope AFM, are given. Details about FEM simulations carried out to estimate the resonance frequency of MCs are presented. The methodology adopted for estimating the mean and gradient residual stress of SiO₂ film from MC bending profiles is delineated. Finally, various experimental setups established and calibration studies undertaken for RH sensing using SiO₂ MCs are given.

2.1. Direct Laser Writer

Direct Laser Writer (DLW) is a mask-less lithography system which is used for transferring the micropatterns from a preloaded soft mask onto Photoresist (PR) coated wafers using a laser source, in a serial fashion. In the present work, a commercial DLW unit (M/s Microtech, Italy, Model no: LW405B), housed in a class-1000 clean room, is used for microfabrication work. This instrument comprise of two units: a write unit and a control unit, the operations of which are controlled by the *Laser Draw* software package. Write unit consists of a laser source ($\lambda \sim 405$ nm, GaN diode laser), a micro translational system for holding the substrate, and other allied electro-optical components for modulating the laser beam as shown in figure 2.1 and 2.2.

Four convex lenses with varying numerical apertures permit the user to select the beam size between 1, 2, 4, and 8 μm and therefore define the patterning resolution (figure 2.2 (a) inset). Depending upon the minimum pattern size in the mask file, the user needs to select the appropriate lens. The write unit also includes an optical filter that can be set at 1, 3, 10, 30, 100% of the available laser beam energy (60 mW) that controls the laser fluence for effective pattern transfer. The PR coated wafer is placed on an XYZ stage and is held with a vacuum chuck. While writing, the laser is auto-focused on the substrate by controlling the Z micro-translation using either geometric or image tracking. The sample stage motion in the XY direction is precisely controlled by interferometers with a resolution of 10 nm. The Control unit consists of three interconnected industrial PCs to control the sample stage, interferometers, laser source, and the user interface (figure 2.2 (b)). Pattern transfer using DLW can be performed in beam, stage, or vector scan modes. In beam scan mode, the entire mask pattern is converted into a bitmap pattern and divided into a number of strips, as shown in figure 2.2 (c). The laser is modulated using an oscillating mirror and is scanned across the strip width on the substrate (in X-direction), while the stage is slowly moved in the direction of the strip length (i.e. Y-direction). Strip width and number of strips depends on the selected lens and its overlap (D-step) can be adjusted by the user interface. It may be noted, the final dose on PR is decided by the laser fluence which in turn depends on the selected optical filter, gain, and D-step. By optimizing various process parameters such as laser dose, focus, diameter, and writing speed, a minimum feature size of $\sim 0.8 \mu\text{m}$, can be achieved using this setup.

It may be noted, photoresist coating (using a spin coater), pre / post-backing, and pattern development process on the substrate at various stages were performed inside the clean-room.

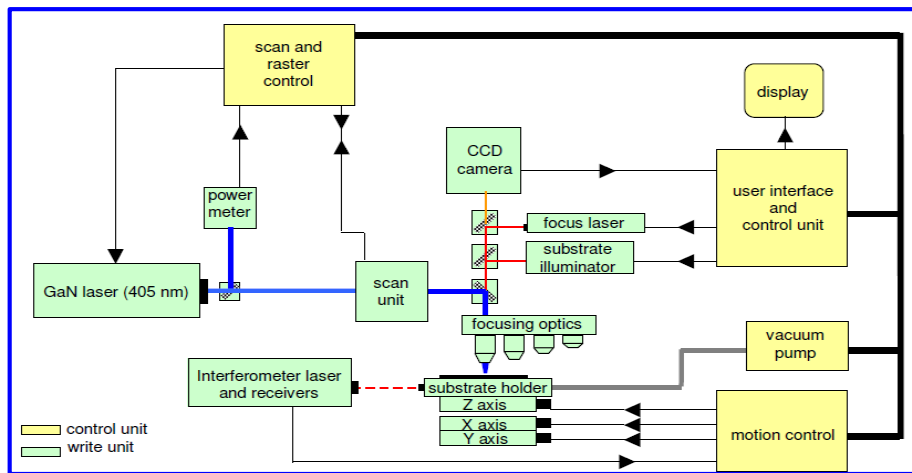


Figure 2.1. Block diagram of DLW (Adapted from User Manual, LB405B, M/s Microtech, Italy).

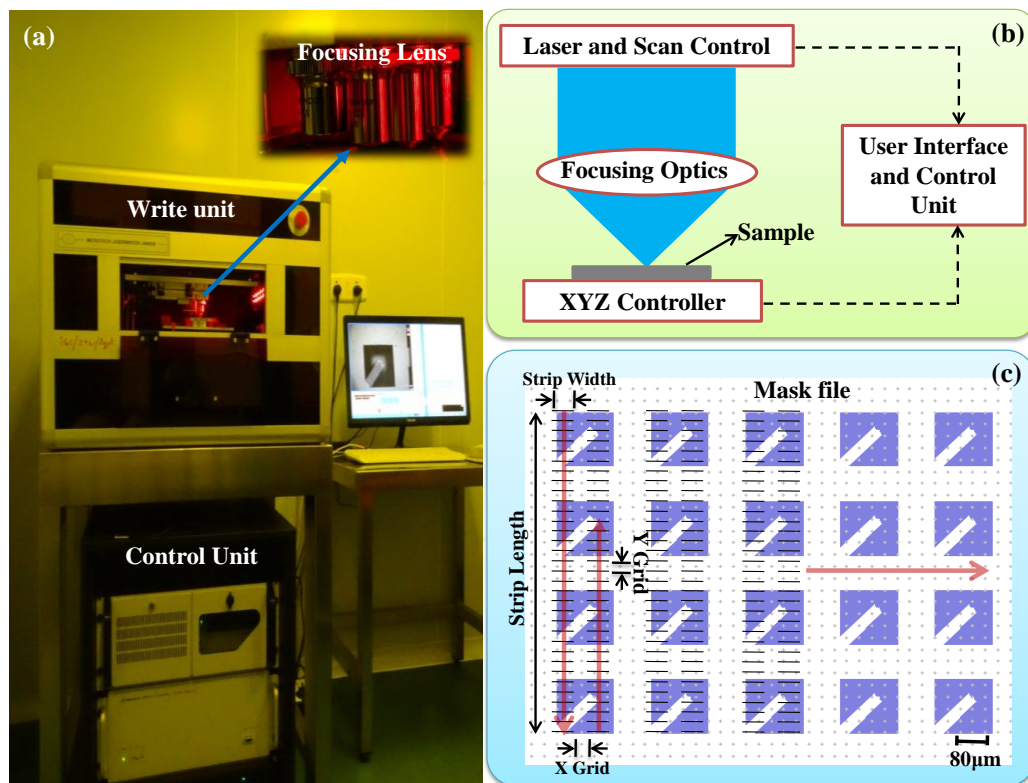


Figure 2.2. (a) Photograph and (b) schematic of the DLW used in the present work. (c) Typical soft mask used to transfer the MC patterns on PR coated wafers. Mask file is divided into strips and is written in a serial fashion. Strip width and number depends on the selected lens and its overlap (D-step) can be adjusted by the user interface.

2.2. Chemical wet bench

Several other microfabrication processes such as Si wafer cleaning (using Piranha solution), etching of SiO_2 (using BOE), and Si etching (using TMAHw solution) were carried out in a chemical wet bench which is housed outside the clean-room. A detailed discussion about each of these processes is presented in chapter 3. The photograph of the experimental setup used for etching Si in TMAHw solution followed by a boiling DI water dip is shown in figure 2.3. TMAHw solution was heated to the required temperature using a hot plate and the Si wafer pieces (containing the MC patterns) were held firmly inside the crucible using a Teflon holder, in vertical position. During etching, the solution was continuously stirred using a magnetic bead and the temperature of the solution was monitored using a thermometer. Additionally, to avoid the loss of liquid from the surface, the crucible was closed using a Teflon lid with provisions for sample holder and thermometer as shown in figure 2.3. Post etch rinsing in boiling DI water was performed on a separate beaker containing DI water placed over another hot plate (see figure 2.3).

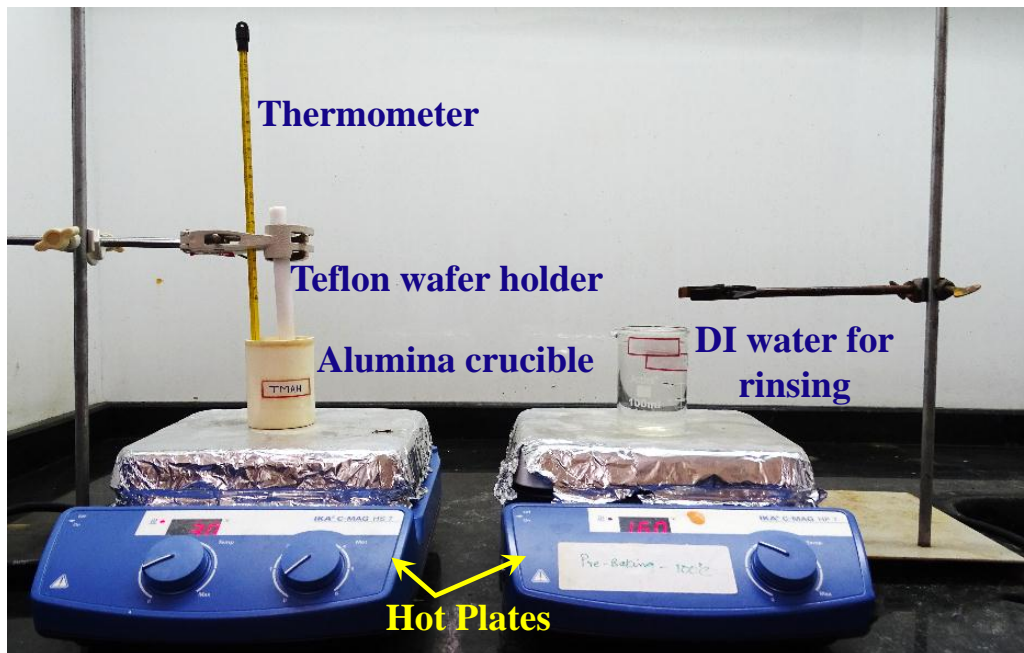


Figure 2.3. Setup inside wet chemical bench for performing Si etching using TMAHw solution followed by rinsing in boiling DI water.

2.3. 3D optical microscope

3D optical microscope (3D OM) is a versatile white light-based interferometric system integrated with a microscope for measuring nanometer range topographical features. It is a non-contact, optical method for height profile measurement of 3D structures. The broad bandwidth white light source used in 3D OM naturally leads to short coherence length which helps in high Z resolution imaging. Further, it can be useful for characterizing the out-of-plane deflection of free-standing mechanical microstructures or membranes, step height, etch depth, and surface roughness of a film/surface [1]. The block diagram of a typical 3D OM is shown in figure 2.4 (a) and its working principle is discussed here briefly. A bright, broadband white light from an LED source initially passes through a neutral density filter preserving its short coherence length. A beam splitter then separates the beam into two parts: directing one part towards the test sample via an objective lens, and the other beam towards a reference mirror. Recombination of the two reflected beams forms a high contrast interference fringes when the waves are in phase i.e. when the sample surface is in focus. Due to the short coherence length of the filtered light source, fringes are localized around the focused area. As the objective lens scans the test sample vertically, the sensor head generates a series of interference patterns, called an interferogram, which is captured by photodetectors. Intensity captured at each pixel of the interferogram is individually processed using frequency domain analysis and a robust algorithm reconstructs the complete three-dimensional image of the test surface with a Z resolution of better than 1 nm and can differentiate heights up to 10 mm [2].

Photograph of the 3D OM (M/s: Bruker, USA make, model: Contour GT-K,) used in the present work is shown in figure 2.4. The equipment is fully automated with a proprietary software *Vision 64*. For measuring curvature present in SiO₂ MCs, the wafer containing MCs was placed on a tilt controlled XY stage. The white light from the LED

source is focused onto the sample with the help of an objective lens of magnification 10X and is scanned in the Z direction. The interferogram, formed between the reflected light from the sample and the reference mirror, is collected by a charge-coupled device which acts as the intensity sensor at the image plane, and the reconstructed 3-D profile of the sample can be viewed through the computer interface. In the present work, all the measurements were performed in vertical scanning interferometry mode at room temperature and ambient pressure.

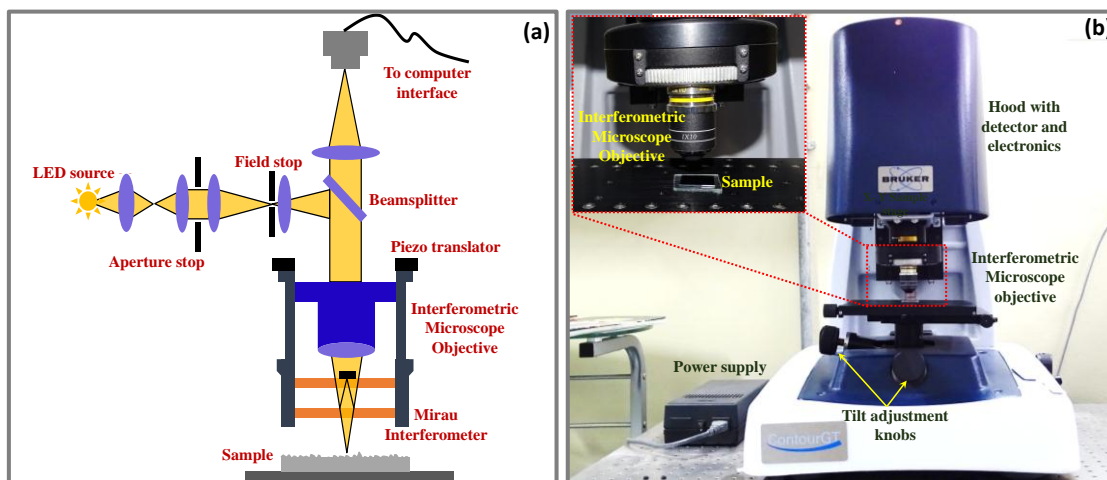


Figure 2.4. (a) Block diagram and (b) photograph of 3D OM used in the present work. Inset in (b) shows the magnified image of the interferometric microscope objective focused on the sample placed on the X-Y stage.

2.4. Nano Vibration Analyzer

A laser-based interferometric system, Nano vibration analyzer (NVA), (M/s SIOS, Germany), is used for dynamic characterization (resonance frequency and vibrational modes shapes) of microfabricated free-standing microstructures. The block diagram and the photograph of the setup employed in the present work are shown in figure 2.5. NVA consists of a fiber-coupled laser (He-Ne laser, $\lambda = 632.8$ nm) based interferometer along with a precision microscope for imaging and focusing the laser beam on the microstructure surface. It also enables real-time monitoring of the sample through a USB camera along

with a computer interface. For resonance frequency measurements of SiO₂ MCs, the wafer containing MCs was glued to a piezo actuator which in turn was placed on the XY sample stage of NVA. The laser beam from NVA was made to focus on the free end of the MC

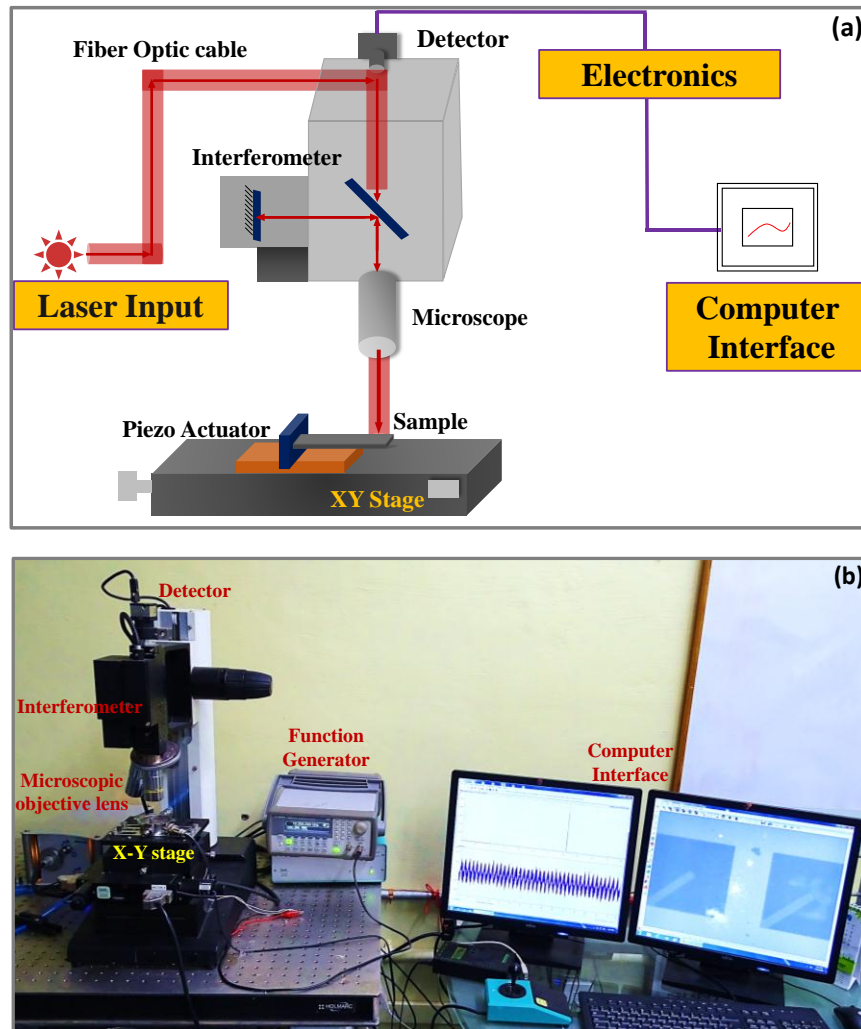


Figure 2.5. (a) Photograph and (b) block diagram of NVA used in the present work.

using a 50X objective lens. Piezo actuator was excited using a function generator (Model: 33220A, M/s Agilent technologies). By varying the function generator frequency in the required steps, the amplitude of vibration was recorded using NVA at each frequency through a user-programmable interface software *InfasVibro*. The resonance frequency of the MC was then estimated from the plot of applied sweep frequency vs amplitude of

vibration. All the measurements were performed at room temperature (23°C) in ambient air (Pressure = 10^5 Pa).

Figure 2.6 shows a typical resonance spectrum of 210 μm long MC measured using NVA along with Lorentzian fit, from which resonance frequency (f_0), bandwidth (Δf), and quality factor ($Q = f_0/\Delta f_{0d}$) were estimated to be 17.82 kHz, 0.89 kHz and 19.82, respectively.

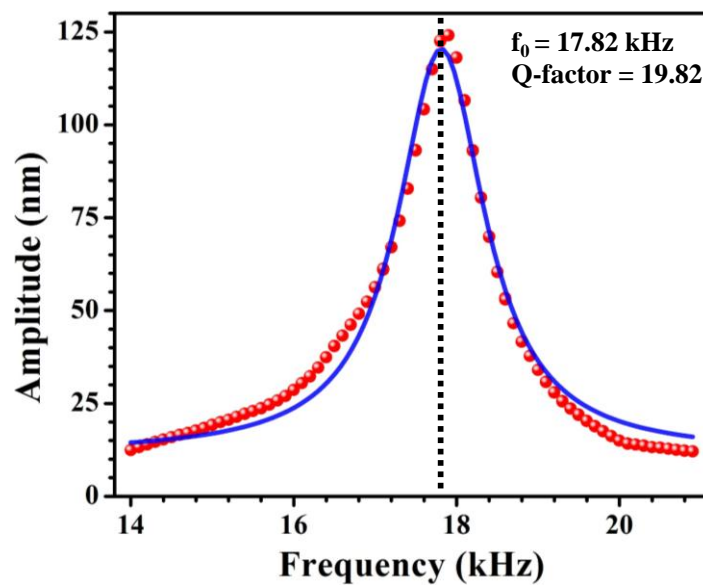


Figure 2.6. Resonance spectrum of a typical 210 μm long SiO_2 MC recorded using NVA.

2.5. Laser Doppler Vibrometer

Laser Doppler Vibrometry is an interferometric technique for measuring velocity and works on the principle of Doppler shift of laser light reflected from the moving object. Because of its non-contact nature and precision, it has been widely used to characterize small-scale vibrations (in the range of few pm to nm) in devices ranging from MEMS to disk drives [3]. In the present work, a commercial Laser Doppler Vibrometer (LDV, M/s: Polytec MSA500) available at CSIR-CEERI, Pilani (Rajasthan), was used for dynamic characterization of the fabricated SiO_2 MCs. A photograph and the block diagram of the experimental setup used is shown in figure 2.7 (a) and (b), respectively. For resonance

measurements, the wafer containing MCs was glued to a piezo actuator (Model No: CMAP09, Noliac) which in turn was excited using a sinusoidal signal (0 – 1 MHz) from the internal function generator of LDV as shown in figure 2.7 (b). The laser beam from LDV was focussed on the free end of the MC, where the amplitude of vibration is maximum. The resonance spectrum was recorded in air by sweeping the frequency, which resulted in several peaks corresponding to various modes of MC along with spurious resonance effects from the piezo-actuator used.

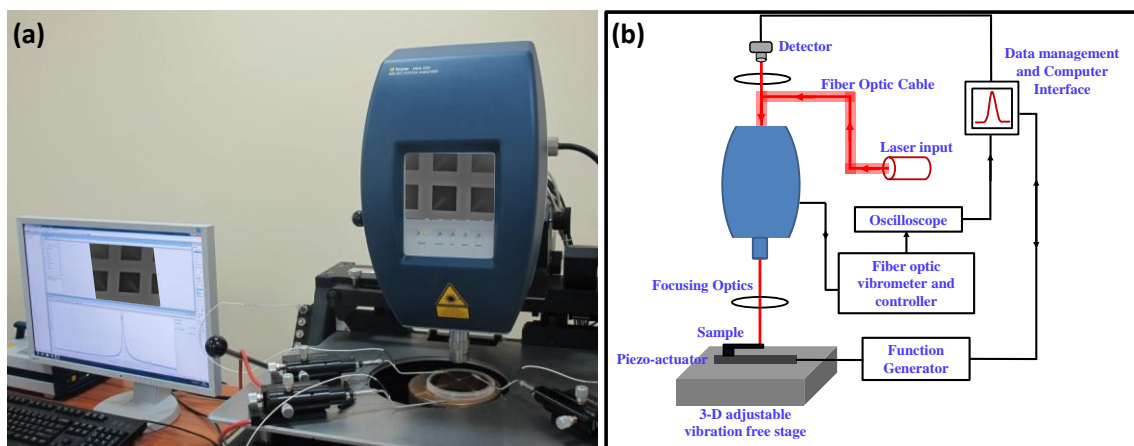


Figure 2.7. (a) Photograph and (b) block diagram of LDV used in the present work for resonance frequency measurements of MCs.

To identify the peak corresponding to the fundamental mode of the MC, two approaches were adopted. In the first approach, the experiment was repeated by focusing the laser on the substrate and the recorded signal was used to subtract the spurious peaks from the piezo actuator. In the second approach, for a given dimension of MC, Finite Element Modelling (FEM) simulations were carried out to predict the fundamental mode resonance frequency (discussed later in section 2.7). Once the desired peak was identified, the frequency spectrum was again recorded around the peak value with a high-resolution frequency scan (figure 2.8(a)) and the resonance frequency was estimated by fitting the recorded peak to a Lorentzian function, as shown in figure 2.8(b). From Lorentzian fit, f_0 , Δf , and Q-factor values were estimated. It may be noted that even though the measured

resonance frequency values using NVA and LDV are nearly similar, the resonance spectrum measured using LDV contains a greater number of data points compared to the data measured using NVA.

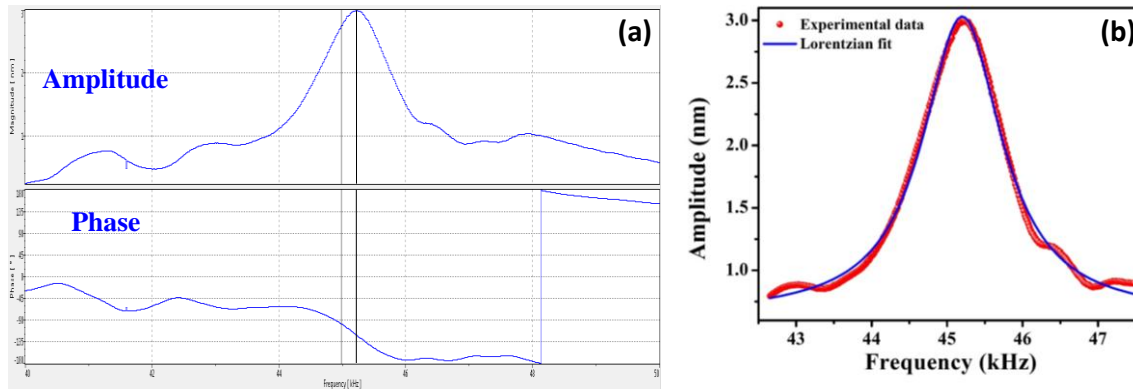


Figure 2.8. (a) High-resolution LDV scan at resonance and its (b) Lorentzian fit on a typical released 130 μm long MC.

2.6. Atomic Force Microscopy

Surface morphology/ roughness of SiO_2 MCs was characterized using a precision Atomic Force Microscope (AFM, M/s NT-MDT Ntegra Prima, Russia – figure 2.9(a)). For this purpose, SiO_2 MC was loaded as sample in AFM and using a commercial MC with tip (Model No: NSG01/Au, M/s: NT-MDT, Russia) it was scanned. AFM was operated in non-contact mode and the scanning was performed under ambient conditions. Once the AFM image was recorded, average and RMS roughness values were extracted using the in-built image analysis module. Figure 2.9 (b) shows a typical AFM image of a SiO_2 surface scanned over an area of $5 \mu\text{m}^2$. From this image, the RMS roughness of the surface was found to be $\sim 4.1 \text{ nm}$. Similar measurements were performed at various places of the sample to obtain statistical variation.

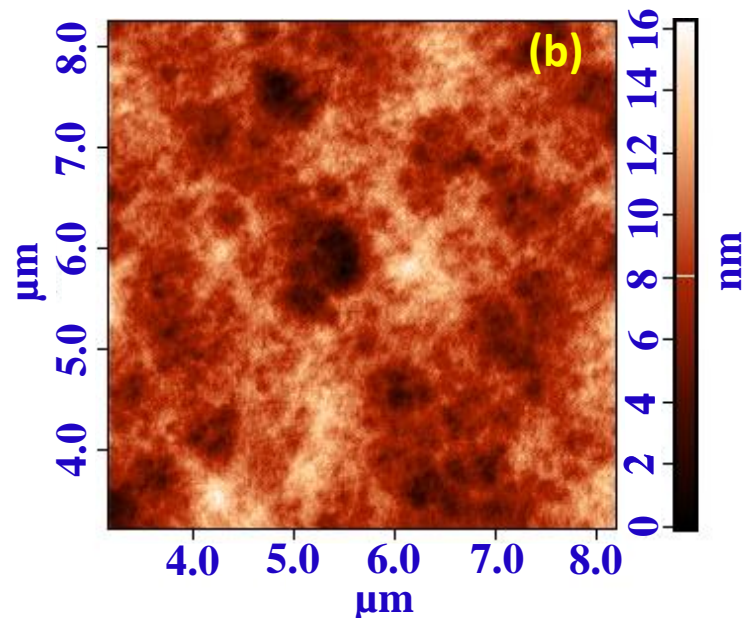
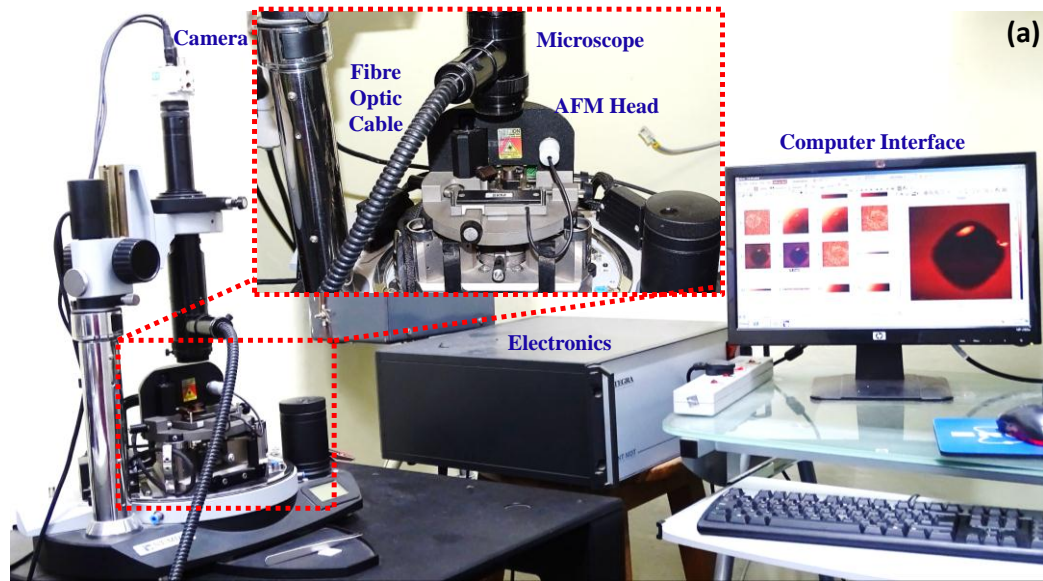


Figure 2.9. (a) Photograph of the AFM used in the present work. (b) Surface morphology of a typical SiO₂ surface recorded using AFM. From this image, the RMS roughness of the surface was estimated to be ~ 4.1 nm.

2.7. Finite Element Modeling simulations

Resonance frequency values of all the MCs were also estimated through FEM simulations, using commercial software package *Intellisuite*. The finite element method is a general technique for constructing approximate solutions to boundary value problems. This method involves dividing the domain of the solution into a finite number of simple sub-domains which are called finite elements and uses variational concepts to construct an

approximate solution over the collection of finite elements [4]. To estimate the resonance frequency of an MC, it was designed with desired dimensions using the *3D builder module* of the *Intellisuite* software. The designed MC was then imported to the *Thermoelectromechanical (TEM) module* where the material properties of SiO₂ were provided as input from the material database of the software (Young's modulus, $E = 70$ GPa, mass density, $\rho = 2650 \text{ kg/m}^3$ [5]). The mesh generated for the calculations consists of cuboids of $1 \mu\text{m}^3$ along the length of the MC. One end of the designed MC was fixed by boundary conditions and vibrational mode simulations were performed as shown in figure 2.10. Simulations were repeated for various dimensions of MCs ($L = 50 - 350 \mu\text{m}$, $W = 40 \mu\text{m}$ and $T = 0.05 - 1 \mu\text{m}$) and compared with experimentally measured values (detailed in chapter 4).

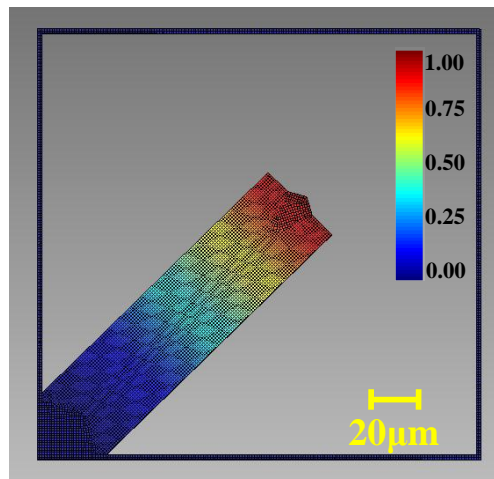


Figure 2.10. MC structure designed and simulated using FEM software with a mesh size of $1 \mu\text{m}^3$. The color code represents the amplitude of vibration and it can be clearly seen that the amplitude is maximum at its free end.

The effect of micro/nanopattern on the resonance frequency of SiO₂ MCs was also studied using FEM simulations. For this purpose, MCs ($210 \times 40 \times 1 \mu\text{m}^3$) with and without surface patterns ($100 \times 100 \times (5-50) \text{ nm}^3$, pitch: $1 \mu\text{m}$) were designed and their resonance frequency values were estimated. Figure 2.11 (a) shows the relative shift in fundamental flexural mode frequencies ($\Delta f/f$ (%)) with respect to unpatterned MCs) plotted

as a function of the depth of micro-patterns. Inset shows similar results but when pattern size is varied from 0 to 20 μm at a fixed pattern depth of 50 nm. From these figures, it is evident that with increasing pattern depth or decreasing pattern size, $\Delta f/f$ increases and is attributed to the reduction in effective thickness of MCs.

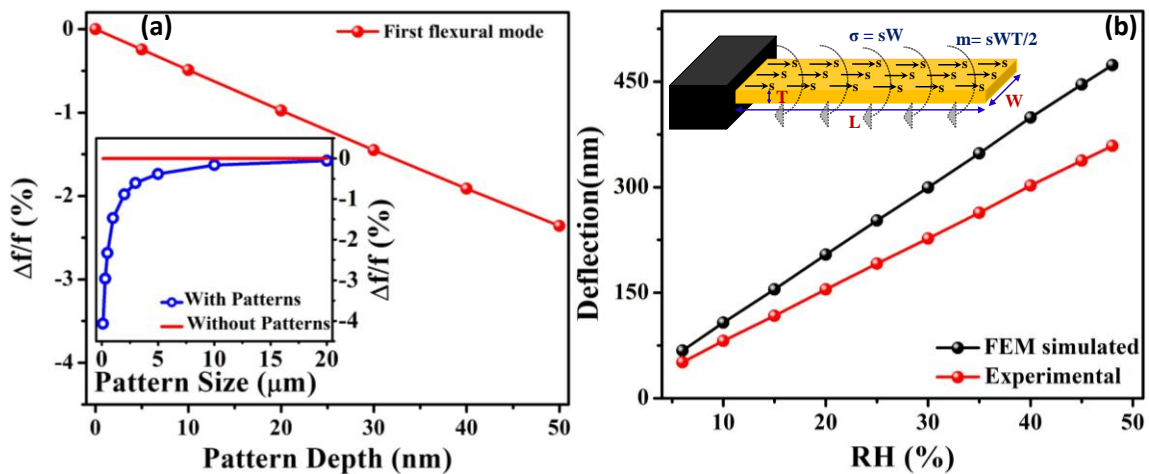


Figure 2.11. (a) Relative shift in the resonance frequency of SiO_2 MCs due to the presence of surface patterns, with varying pattern depth, estimated using FEM simulations. Inset shows the relative shift in the resonance frequency of SiO_2 MCs as a function of surface pattern size. (b) Static deflection of the MCs estimated using FEM simulation along with experimentally reported values from literature [7], while RH is varied between 6 to 50%. Inset shows the schematic diagram of MC and the loading scenario used in FEM simulations based on Zhang et al. model [6]. The surface stress is modeled as the uniformly distributed axial stress $\sigma = sW$ and a uniformly distributed bending moment $m = sWT/2$ where s is the uniformly distributed area stress and W and T are the width and the thickness of the MC.

Static bending characteristics of MCs were also examined using FEM simulations. For this purpose, surface stress-induced deflection of an MC ($210 \times 40 \times 1 \mu\text{m}^3$) during adsorption of water molecules while RH is varied between 6 to 50% was studied. Surface stress was modeled as an equivalent uniform in-plane force acting on the surface of the MC [6]. Figure 2.11 (b) shows the simulated peak deflection values with increasing RH.

For comparison, experimental deflection values, reported in the literature [7] on MCs with similar dimensions during adsorption of water molecules, is also shown in this figure. From this figure, it is clear that with increasing RH, MC deflection increases indicating an increase in surface stress. However, FEM simulations overpredicted the experimental deflection values by $\sim 32\%$, especially at higher RH values. This is probable, because in FEM simulations surface roughness and associated stress concentration regions are not included.

2.8. Estimation of mean and gradient residual stress of films from MC bending

When SiO₂ MCs are released by etching the underlying Si substrate, residual stress in the SiO₂ film gets released as out-of-plane deformation of MC. In general, the uniaxial residual stress in a thin film is represented by [8],

$$\sigma_{tot} = \sum_{k=0}^{\infty} \sigma_k \left(\frac{y}{T/2} \right)^k \quad (2.1)$$

where, T is the thickness of the film and y is a coordinate across the thickness of the film, and k is an integer. In the first approximation, i.e. when k is truncated to 1, σ_{tot} is the sum of constant mean stress σ_0 and gradient stress σ_1 . Neglecting the higher-order terms, Eq. 2.1 becomes,

$$\sigma_{tot} \cong \sigma_0 + \sigma_1 \left(\frac{y}{T/2} \right) \quad (2.2)$$

While studying the residual stress in SiO₂ films using MCs, Fang et al. [8] proposed that the out of place deformation of the MCs can be modeled as the combination of gradient stress (σ_1) induced curvature and mean stress (σ_0) induced initial slope at the fixed end. The total angular rotation of the MC is determined by the superposition of components

due to mean and gradient stress, i.e. θ_0 (curvature due to mean stress) and θ_1 (curvature due to gradient stress), respectively. Based on the empirical fits θ_0 and θ_1 were found to be,

$$\theta_0 = \frac{\sigma_0}{E} (1.33 + 0.45\nu)(-0.014h + 1.022) \quad (2.3)$$

$$\theta_1 = \frac{\sigma_1}{E} (0.0086h^2 - 0.047h + 0.81) \quad (2.4)$$

where, E , ν , and T are the Young's Modulus, Poisson's ratio, and thickness of MC, respectively. In addition to the base rotation, the gradient residual stress also contributes to the out-of-plane deflection which could be estimated by the radius of curvature, R of the MC as,

$$\sigma_1 = \frac{ET}{2R} \quad (2.5)$$

Now, by superimposing the effects due to σ_0 and σ_1 , the transverse deflection of the MC is given as,

$$y = (\theta_0 + \theta_1)x + \frac{1}{2R}x^2 \quad (2.6)$$

where x is a point along the length L of the MC. Using this model, in the present work, the mean and gradient residual stress present in the SiO_2 film was estimated. Figure 2.12 shows a typical deflection profile of an MC along with the extracted components of x and x^2 using eq. (2.6). From these figures, mean and gradient residual stress values were estimated and found to be -451.34 MPa and 15.62 MPa, respectively.

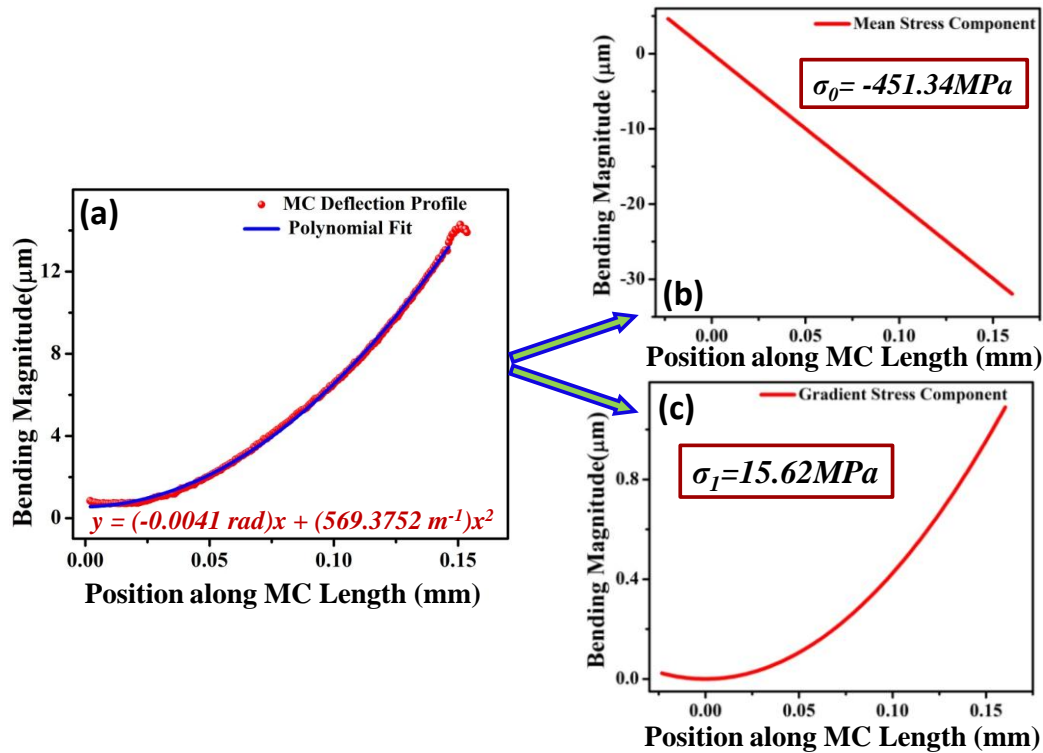


Figure 2.12. Deconvolution of mean and gradient residual stress components from initial bending profile of MCs. (a) Deflection profile of a typical released SiO₂ MC across its length. From this, (b) mean (x-component) and (c) gradient (x² component) residual stress values were estimated using Fang's et al. model [8].

2.9. Annealing experiments on released SiO₂ MCs

In the present thesis, the effect of high-temperature annealing on the residual stress evolution of the released SiO₂ MCs was studied (discussed in chapter 4). For this purpose, a set of wafers containing SiO₂ MCs was annealed at 800°C and 1000°C in O₂ and N₂ atmospheres. Details about the samples and annealing conditions are discussed in detail in chapter 4, section 4.2. Figure 2.13 shows a typical temperature profile used for annealing a sample at 800°C. It may be noted after annealing at the specified temperature for the required duration (800 °C for 60 min in figure 2.13), the furnace was switched off and the sample was allowed to cool down naturally through convection.

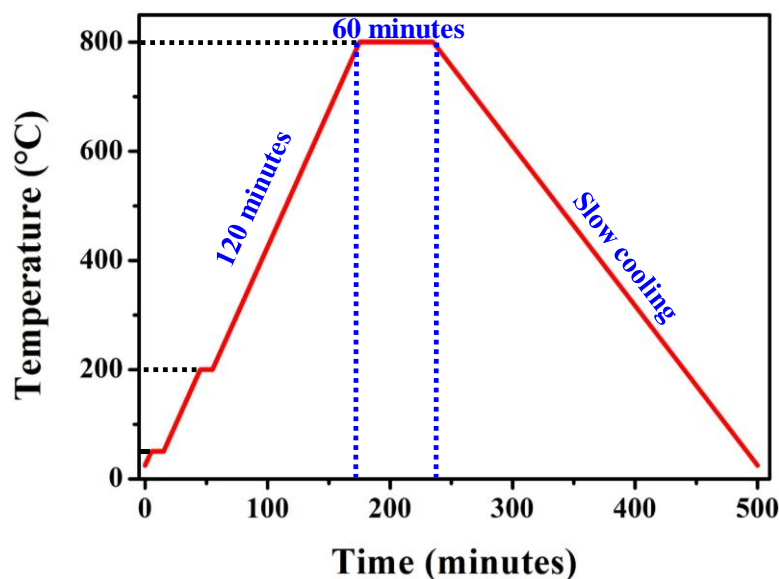


Figure 2.13. Typical temperature profile set in the furnace for high temperature annealing of SiO₂ MCs in O₂ environment.

2.10. Experimental setup for RH sensing

2.10.1. Fabrication of mini air-tight chamber

An air-tight stainless steel (SS) chamber was designed and fabricated for performing RH sensing experiments on SiO₂ MCs using NVA. The fabricated cylindrical chamber (75 mm diameter x 20 mm height) consists of a transparent quartz glass window port on the top (figure 2.14 a) which serves twin purposes of visual inspection and performing optical experiments using NVA. The chamber was provided with a base plate at the bottom for fixing the chamber on the XY stage of NVA. The chamber also has provisions for gas inlet and outlet and an 8-pin/5A electrical biasing feedthrough connector, as shown in figure 2.14 (b) and (c).

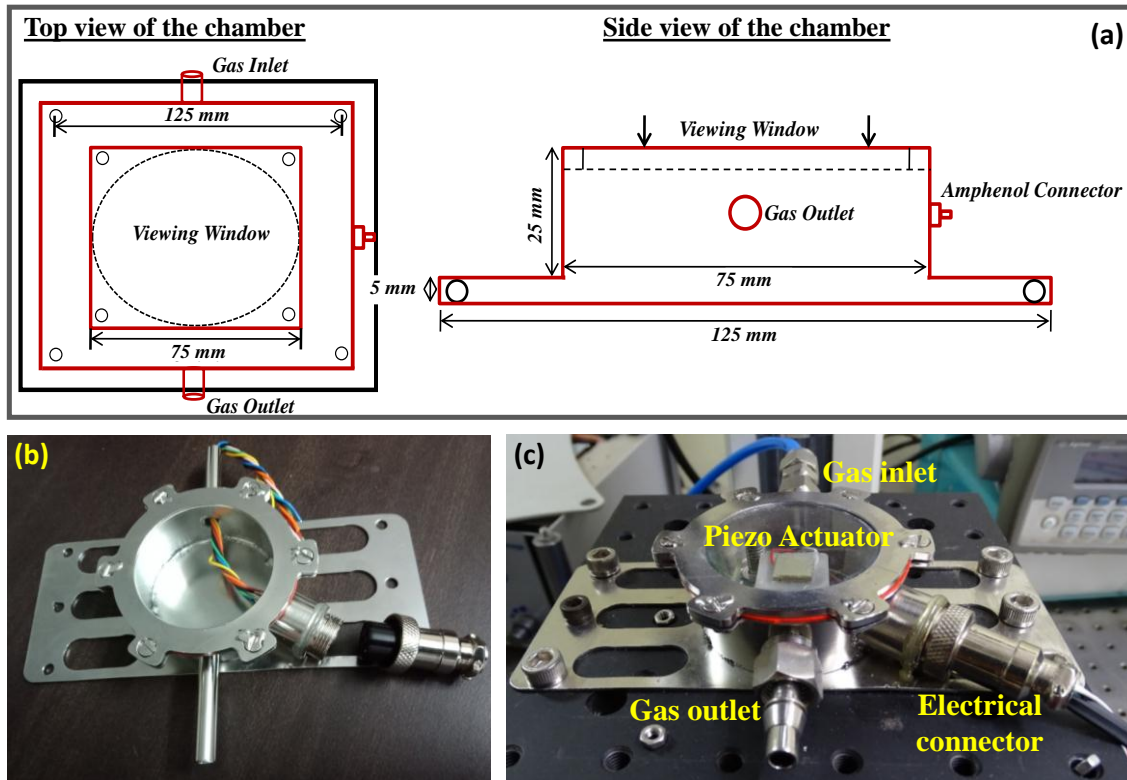


Figure 2.14. (a) Top and side views of the custom-made air-tight chamber designed for RH sensing experiments. Photograph of the (b) chamber and (c) RH sensing setup where it is mounted on the XY stage of NVA. In these photographs, electrical connection for piezo actuator and gas inlet ports are also clearly seen.

2.10.2. Resonance frequency measurements

RH sensing experiments were performed by measuring the shift in resonance frequency (fundamental mode) of the MCs, using NVA, when the RH is varied between 20% and 90%. MCs were excited using a piezo actuator which in turn was driven using a function generator. Wafer containing the MCs along with the piezo actuator was placed inside the air-tight chamber, which in turn was mounted on the XY stage of NVA. RH inside the chamber was precisely controlled by varying the flow rate of wet and dry nitrogen (N_2) gas using mass-flow controllers (Model: GFC17, M/s Aalborg) and a home-made bubbler setup, as shown in figure 2.15. All the experiments were performed in air at ambient conditions (Ambient pressure $\approx 10^5$ Pa) and the temperature inside the chamber

was maintained at 23°C ($\pm 0.2^{\circ}\text{C}$). RH and temperature inside the environmental chamber were independently measured using a commercial RH sensor (M/s Sensirion SHT21, Switzerland, accuracy $\pm 2\%$).

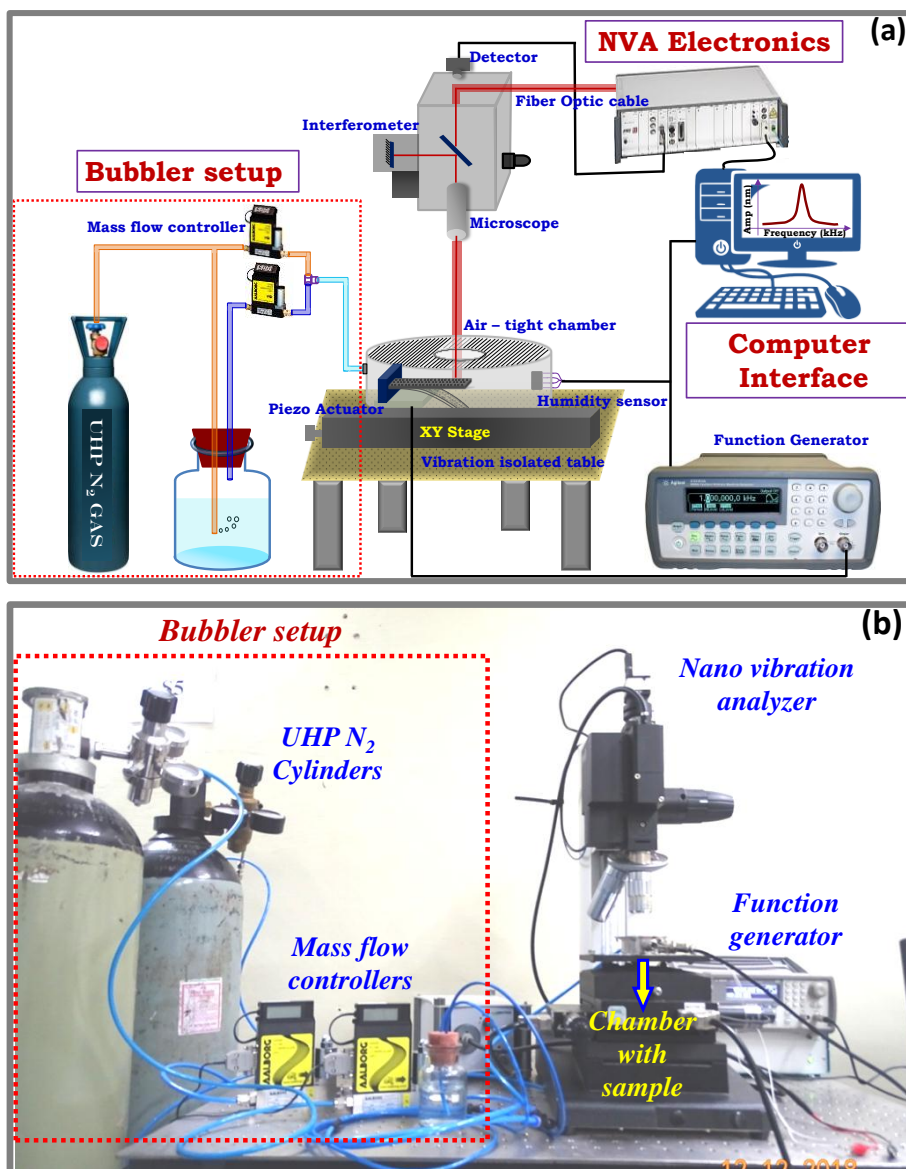


Figure 2.15. (a) Schematic and (b) photograph of the experimental setup used for measuring the shift in the resonance frequency of the MCs using NVA when the RH is varied between 20% and 90%.

Initially, RH inside the chamber was stabilized at 20% by continuously purging the ultra-high pure dry N₂ gas. The resonance frequency of MCs recorded at this RH value served as a reference for all other measurements. Now, the RH inside the chamber was

increased in steps of 5% till 90% and at each interval, the resonance spectrum was recorded. For hysteresis measurement, experiments were repeated while RH is reduced back to 20%. It may be noted that at a given interval, the RH value was allowed to stabilize for ~ 10 minutes, and at least three resonance spectra were recorded during this time interval. Ahead of actual experiment, RH variation and temperature inside the chamber was calibrated and is shown in figure 2.16.

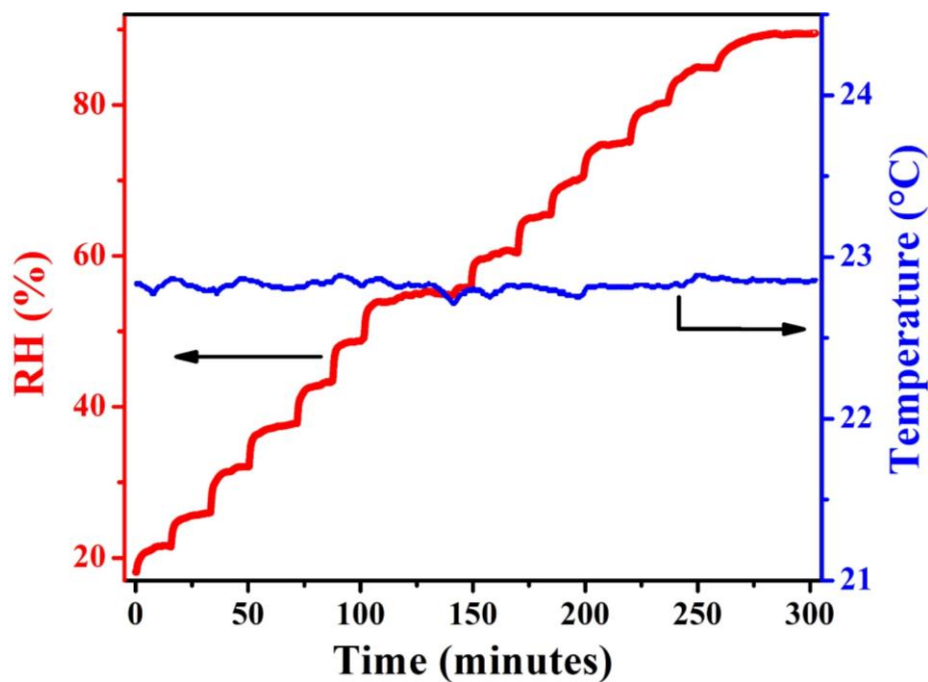


Figure 2.16. Typical calibration plot showing the variation of RH (red line) and temperature (blue line) inside the chamber, with time. These measurements were performed using a commercial RH sensor while RH inside the chamber was varied.

2.10.4. Setup for breath monitoring studies

Breath monitoring experiments were performed by exposing MCs to inhale and exhale breath cycles of healthy adult (male) and by continuously measuring the shift in peak amplitude at the resonance of these devices using NVA. For this purpose, the same experimental setup shown in figure 2.15 was used, however, now a breathing mask setup was used as RH input, as shown in figure 2.17. The data were recorded during normal

(inhale-exhale cycle = 4 s) and slow breathing (inhale-exhale cycle = 10 s) cycles under ambient conditions. The measurements were recorded with 5 MCs to ensure the repeatability and reliability of the sensors. The RH variation during the experiment was also continuously recorded using a commercial RH sensor.

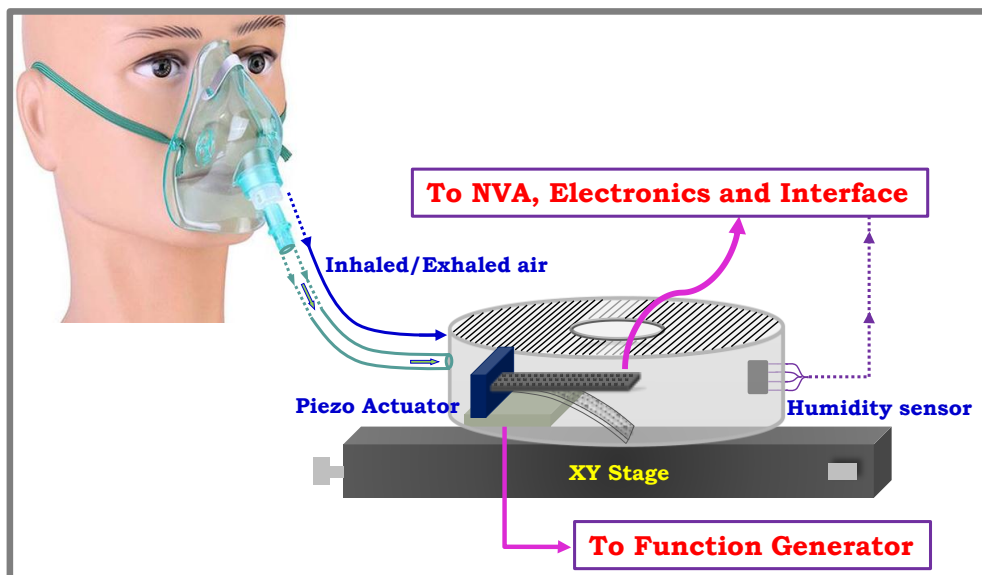


Figure 2.17. Experimental setup for monitoring human respiration during inhale/exhale breath cycles.

References

- [1] S.C.H. Thian, W. Feng, Y.S. Wong, J.Y.H. Fuh, H.T. Loh, K.H. Tee, Y. Tang, L. Lu, Dimensional measurement of 3D microstructure based on white light interferometer, *J. Phys. Conf. Ser.* 48 (2007) 1435–1446.
- [2] C. O’Mahony, M. Hill, M. Brunet, R. Duane, A. Mathewson, Characterization of micromechanical structures using white-light interferometry, *Meas. Sci. Technol.* 14 (2003) 1807–1814.
- [3] B. Ohler, Cantilever spring constant calibration using laser Doppler vibrometry, *Rev. Sci. Instrum.* 78 (2007).
- [4] S.S. Rao, *The Finite Element Method in Engineering*, Fourth Edition, Elsevier Publications, 2011.

- [5] R. Knizikevičius, Real dimensional simulation of SiO₂ etching in CF₄+H₂ plasma, *Vacuum*. 65 (2002) 101–108.
- [6] Y. Zhang, Q. Ren, Y.P. Zhao, Modelling analysis of surface stress on a rectangular cantilever beam, *J. Phys. D. Appl. Phys.* 37 (2004) 2140–2145.
- [7] K. Lakshmoji, K. Prabakar, S. Tripura Sundari, J. Jayapandian, C.S. Sundar, Effect of surface stress on microcantilever resonance frequency during water adsorption: Influence of microcantilever dimensions, *Ultramicroscopy*. 146 (2014) 79–82.
- [8] W. Fang, J.A. Wickert, Determining mean and gradient residual stresses in thin films using micromachined cantilevers, *J. Micromechanics Microengineering*. 6 (1996) 301–309.

Chapter 3

Fabrication and Characterization of SiO₂

Microcantilevers

In this chapter, details about the fabrication of SiO₂ MCs of various dimensions ($L = 50 - 330 \mu\text{m}$; $W = 37 \mu\text{m}$; $T = 0.98 \mu\text{m}$), using DLW and wet chemical etching methods, are presented. Optimization of various process parameters carried out for the successful release of SiO₂ MCs, such as laser dose (in DLW), pre- and post-baking temperature values, method to avoid stiction during Si etching, etc., are explained. Details about the fabrication of SiO₂ MCs with controlled surface micro-patterns ($4 \times 4 \times (0.015 - 0.075) \mu\text{m}^3$) using two-layer lithography are also given. Static and dynamic characterization results on the successfully released MCs using 3D OM and NVA are detailed.

3.1. Introduction

SiO₂ MCs are normally fabricated using SiO₂/Si wafer in two steps. In the first step, the desired MC pattern is transferred on SiO₂ layer by standard UV lithography technique, while the second step involves the release of MCs from bulk silicon (c-Si) by either wet chemical [1] or dry reactive ion etching [2] of c-Si resulting in free-standing SiO₂ MCs. For MC fabrication, though the pattern transfer can be preferentially achieved through conventional UV lithography due to its ability to pattern large areas with micron size resolution in minutes, it has certain disadvantages such as; i) requirement of pre-fabricated Chrome mask, whose cost can be substantial if the required pattern resolution is high, ii) lack of flexibility of the mask since the designed mask cannot be altered. Any minor changes in MC design require a complete set of new masks, resulting in high

production costs and delayed times and finally iii) it is limited to planar lithography, i.e. 3D patterning is not possible [3,4].

DLW is an alternative patterning method that circumvents the above issues and is emerging as an interesting new technology for micro/nano fabrication [5,6]. In this method, a laser beam is used to write (transfer) the desired pattern from a soft mask, on a photoresist coated substrate, in a serial fashion. Therefore, it is a mask-less technique which offers a great advantage as a rapid prototyping tool since the desired patterns can be designed and modified in the software itself without the need for making new Chrome masks. However, the major disadvantage of DLW technique is its low writing speed, considering that one laser beam is typically used to write the entire pattern. But this is an acceptable compromise due to its higher flexibility at design stage [7]. In terms of resolution of the physical feature that can be achieved, DLW bridges the gap between nanolithography techniques such as e-beam and AFM-based lithography and micrometer-resolution UV lithography [8]. A minimum feature size of 150 nm can be easily achieved using DLW, if diffractive-limited optics and short wavelength UV-visible lasers are used [9]. Various techniques of DLW have been developed, with applications in fabrication of optical elements [10], polymer field effect transistors [11], micro batteries and sensors [9]. Moreover, for the fabrication of microfluidic components with precisely defined geometries using SU-8 photoresist, it is shown that DLW is the preferred fabrication method over UV photolithography [12]. Attempts are also made in literature [13] to combine the conventional mask-based UV lithography with DLW to compensate for the drawbacks of each system. Also, in recent years, femtosecond laser based DLW techniques have shown the capability for prototyping 3D micro/nano structures by using suitable photosensitive materials [3,14].

Once the desired pattern is transferred on the photoresist and subsequently on to the SiO₂ satisfactorily, SiO₂ MCs are typically released by etching the underlying c-Si by wet chemicals such as potassium hydroxide (KOH), tetramethylammonium hydroxide (TMAH) or Ethylenediamine Pyrocatechol (EDP) solutions. Various process optimizations during the release of MCs by these methods require careful evaluation of advantages and trade-offs. For example, Jolly et al [15], fabricated miniature SiO₂ MCs by anisotropic etching of Si using the EDP solution and gave criteria for stability of the released structures. They used elastic theory to show that MCs whose thickness to width ratio is smaller than $0.52\sqrt{\Delta\alpha\Delta T}$ would not be stable due to stress caused by the difference in thermal expansion coefficient ($\Delta\alpha$) of Si and SiO₂ at elevated temperatures of film growth (ΔT). In yet another study, Jovic et al [1] showed that the orientation of SiO₂ MCs with respect to the underlying Si plays the pivotal role in the stability of these structures when released by wet chemicals and concluded that MCs which are oriented along $\langle 100 \rangle$ direction of Si are more stable compared to the ones oriented along $\langle 110 \rangle$ direction. They have also shown that Si etching in TMAH solution compared to KOH solution yields more stable MCs.

When wet chemicals are used for releasing the SiO₂ MCs, the released devices usually stick to the underlying Si substrate, making the device unusable. Stiction in these devices occurs when the capillary/electrostatic forces between the structural layer and the substrate dominate over the elastic restoring force of the former, leading to device failure [16]. Several methods are proposed in the literature to avoid stiction, which includes evaporation drying after rinsing in liquids having low surface tension at their boiling points [17], sublimation of the rinse liquid after low-temperature solidification, critical point drying at high pressure [18], etc. Joshi et al [19] proposed a novel technique to release ultra-thin SiO₂ MCs by etching significant amount of Si from the backside prior to

patterning the MC from the front side of the wafer which eliminates stiction during wet chemical etching. Methods of reducing stiction by reducing the MC-substrate contact area were also studied by several authors. They include introducing temporary support structures such as bumps, sidewall spacers or by increasing the surface roughness at the interface [20] and by adding small areas with convex corners, at the periphery of the microstructures, near the point of largest vertical deflection [21] to counteract the surface tension forces.

In the present thesis, SiO₂ MCs of various lengths (keeping width and thickness constant) were fabricated using DLW and wet chemical etching methods. Various microfabrication process parameters were optimized for the successful release of these devices. Successfully released MCs were characterized using a 3D OM and NVA for initial bending and resonance frequency measurements, respectively. The released MCs were found to exhibit upward bending and their corresponding peak deflection was found to increase with increasing MC length. From the linear relation between these two parameters, the gradient residual stress in the SiO₂ film was estimated. Experimentally measured resonance frequency values were compared with analytical values estimated from classical beam theory and the reasons for the difference between these two values especially at smaller lengths are discussed. Details about the fabrication of SiO₂ MCs with controlled surface micro-patterns using two-layer lithography are also discussed. Finally, the effect of micro-patterns on the static and dynamic properties of the MCs is discussed.

3.2. SiO₂ microcantilever fabrication steps

SiO₂ MCs of varying lengths in the range from 50 μm to 330 μm with fixed width and thickness of 37 μm and 0.98 μm, respectively, which are oriented in <100> direction of Si {100} wafer (i.e. 45° to primary flat), were fabricated using DLW and wet chemical

etching method. Various parameters set in DLW for MC pattern transfer and details about the mask file used are given in Table 3.1. It may be noted, MCs oriented in Si <100> direction, are relatively easy to fabricate and more stable compared to the ones oriented in Si <110> direction [1] (see section 3.2.1 for more details). Various steps followed for the fabrication of these MCs are shown in figure 3.1. Si {100} wafer (IceMOS Technology Ltd., UK) with 0.98 μm thick thermal oxide was used as starting material (figure 3.1 (a)). Fabrication process started with *Piranha* (H_2SO_4 : H_2O_2 in 3:1 ratio) cleaning of SiO_2/Si {100} wafer pieces (2 cm x 2 cm) followed by spin coating of $\sim 1.4 \mu\text{m}$ thick positive photoresist (AZ1512HS, Microchemicals, Germany) (figure 3.1 (b)). PR coated wafer was pre-baked at 100 $^\circ\text{C}$ for 60 s to evaporate the solvents. Thereafter, the wafer was placed on the sample holder of DLW to transfer the pre-loaded MC mask pattern in CIF format.

Table 3.1. Various process parameters set in DLW for pattern transfer on PR coated wafer and details about the soft-mask file.

| S.No. | Parameter | Value |
|-------|---------------------------------|---|
| 1. | Laser wavelength | 405 nm |
| 2. | Laser power | 3% of 60 mW |
| 3. | NA of the lens | 0.65 (lens 5) |
| 4. | Writing mode | Beam scan |
| 5. | Sample stage control resolution | 10 nm (Interferometric) |
| 6. | Write speed | 320 $\mu\text{m}/\text{sec}$ |
| 7. | Total writing time | ~ 5000 sec (1.5 Hrs) |
| 8. | Laser dose | 272 mJ/cm^2 |
| 9. | Mask size | 12000 μm x 12800 μm |
| 10. | No. of strips | 124 |
| 11. | Strip length & width | 12800 μm & 100 μm |
| 12. | X and Y grid (D-step) | 0.1 μm & 0.2 μm |

Laser dose for effective pattern transfer on photoresist was optimized and found to be 272 mJ/cm^2 (see section 3.2.2 for details). Post-written patterns were developed in developer solution (AZ400K, Microchemicals, Germany) and once the patterns were satisfactory, the wafer was post-baked at 150°C for 10 min (see section 3.2.3 for details). Followed by this, the wafer was etched using buffered oxide etchant (BOE, M/s Microchemicals GmbH, Germany, etch rate $\sim 80 \text{ nm/minute}$) for $\sim 10 \text{ min}$ to transfer the pattern from PR to SiO_2 layer (figure 3.1 (c)).

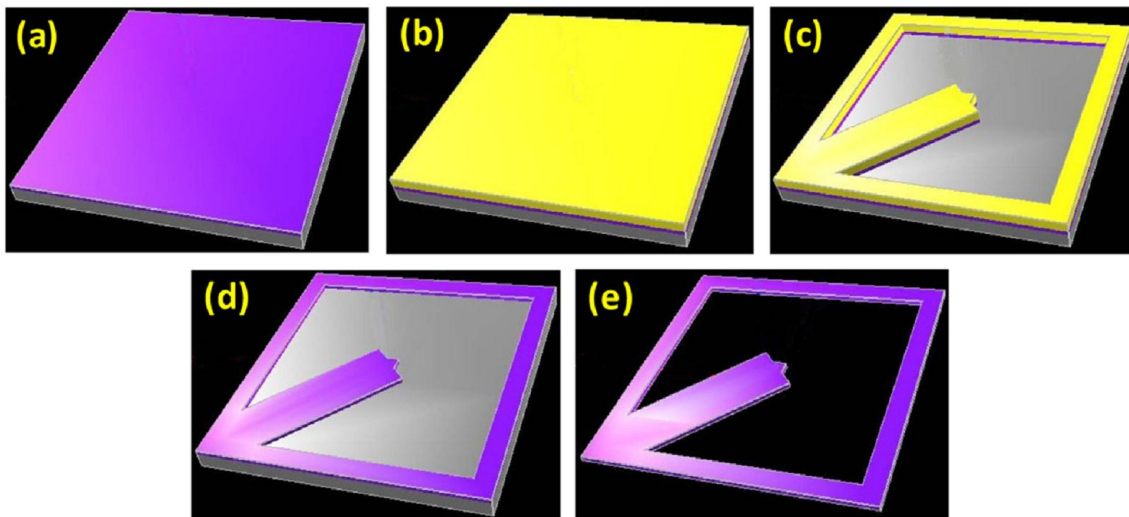


Figure 3.1. Various process steps involved in the fabrication of SiO_2 MCs. **(a)** Starting material: Si $\langle 100 \rangle$ wafer with $0.98 \mu\text{m}$ thick thermal SiO_2 . **(b)** $1.4 \mu\text{m}$ thick photoresist (PR) is coated using spin coater. **(c)** MC pattern is transferred on PR using DLW followed by buffered oxide etching of SiO_2 . **(d)** PR is stripped using acetone and cleaned with IPA. **(e)** Underlying Si is etched in TMAHw solution to finally release the SiO_2 MC.

After oxide etching, the residual PR was stripped off in acetone and cleaned with isopropyl alcohol (IPA) (figure 3.1(d)). Finally, bulk Si below the patterned SiO_2 was etched using TMAHw solution (diluted to 5%) at 75°C for $\sim 90 \text{ min}$, to release the SiO_2 MCs (figure 3.1 (e)). During etching, TMAHw solution was continuously stirred using a magnetic bead, to maintain a constant temperature. After the etching process, the wafer was removed from the solution and thoroughly rinsed with DI water, allowed to dry in

Table 3.2. Various process parameters optimized for the successful released of SiO₂ MCs.

| Microfabrication process | Optimized value |
|---|---|
| MC orientation | <100> orientation of SiO ₂ /Si {100} wafer |
| <i>Wafer cleaning</i> | |
| Piranha (H ₂ SO ₄ :H ₂ O ₂) cleaning | 15 min. |
| DI water rinse | 5 min. |
| <i>PR (AZ1512 HS) coating</i> | |
| Pre-heating temperature and time | 150 ⁰ C, 10 min. |
| Spin-coating speed and time | 4000 rpm, 30 s. |
| Pre-baking temperature and time | 100 ⁰ C, 60s. |
| <i>Lithography</i> | |
| DLW Laser energy | 272 mJ/cm ² |
| PR Development (AZ400K) time | 30 -35 s. |
| Post-baking temp and time | 150 ⁰ C, 10 min |
| <i>SiO₂ etching</i> | |
| BOE Time and temperature | 10 min, 25 ⁰ C (Room temperature) |
| <i>Si etching using TMAH (5 wt%)</i> | |
| Temperature and time | 75-80 ⁰ C, ~90 min |
| DI water rinse temperature and time | 100 ⁰ C, ~ 10 min |

ambient air and was carefully observed under microscope. However, most of the released SiO₂ MCs were stuck to the bottom Si, as expected, due to “stiction”. In the present thesis, an innovative two-step process was followed to avoid stiction and is discussed in detail in section 3.2.4. Table 3.2 summarizes various process parameters optimized for the

successful release of SiO₂ MCs. Figure 3.2 shows a typical FESEM image of the successfully released SiO₂ MCs after implementing these optimization steps. Once the fabrication process is complete, the wafer containing the released SiO₂ MCs was carefully stored in a vacuum desiccator before being taken for characterization.

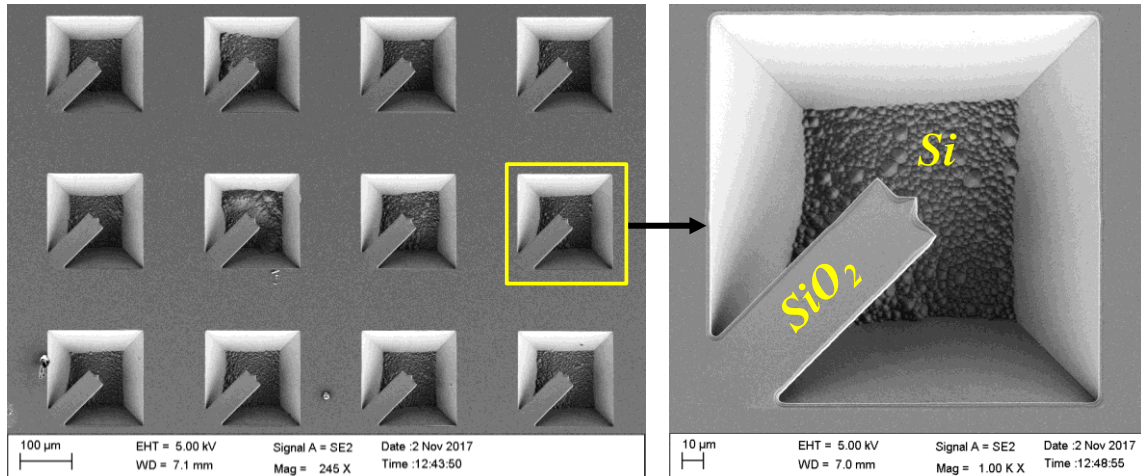


Figure 3.2. FESEM images of the typical SiO₂ MCs fabricated in the present work. A tip at the free end is added to avoid the stiction while releasing the MCs by wet chemical etching method.

Experiments performed to optimize various process parameters such as laser dose (in DLW), PR post-baking temperature/time and a two-step process followed to avoid “stiction” are discussed now.

3.2.1. MC orientation with respect to Si

It is well known that the crystallographic orientation of underlying Si (see figure 3.3 (a)) plays a major role in achieving the stability of the SiO₂ MCs released by wet chemical methods [1,22]. The orientation determines the preferential direction along which the etching of underlying Si below the MCs progresses. When MCs are oriented along $\langle 100 \rangle$ direction, etching of Si initiates and progresses along the width of MC whereas, etching is preferred along length in the MCs oriented along $\langle 110 \rangle$ (see figure 3.3 (b), (c), (d)). In the former case, Si remains till the final release of MCs and thus

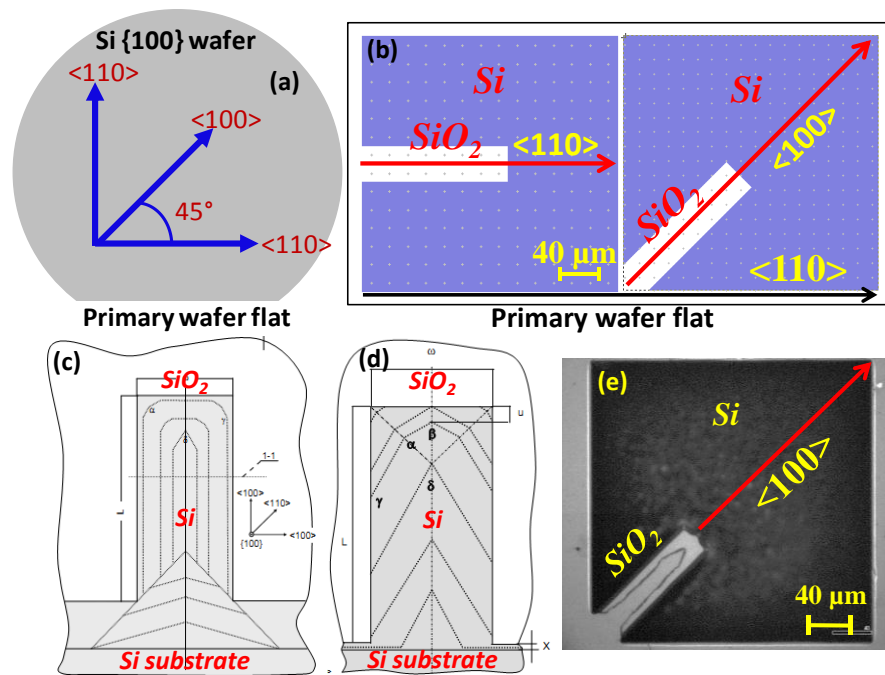


Figure 3.3. (a) Schematic of different crystallographic orientations in Si {100} wafer with respect to the wafer prime flat. (b) Typical mask layout showing MCs oriented along $\langle 110 \rangle$ and $\langle 100 \rangle$ directions. Evolution of Si undercutting when SiO_2 MCs are oriented along (c) $\langle 100 \rangle$ and (d) $\langle 110 \rangle$ directions with respect to underlying Si {100} wafer (adopted from [1]). In (c) and (d) the black dotted lines represent the progressing direction of Si etching in TMAH solution, with time. (e) Typical optical microscope image of a SiO_2 MC oriented in $\langle 100 \rangle$ direction after 50 minutes of Si etching. Underlying Si, along the width of the MC is clearly seen in this image.

ensuring the stability (figure 3. 3 (e)). Also, releasing of MCs oriented at 45° to the primary flat of Si {100} wafer is an easy and fast process compared to 90° oriented MCs; normally the width is significantly smaller than the length of any MC [1,22]. Taking these aspects into consideration, in this work, it was decided to fabricate MCs which are aligned 45° ($\langle 100 \rangle$ direction) to the primary flat of the {100} Si wafer.

3.2.2. Laser dose optimization

While transferring a micro pattern using DLW on the PR, there exists a critical laser dose - ' D_c ', at which the transferred pattern matches exactly with the actual mask pattern. If the laser dose is lower than D_c , residual PR remains at the exposed regions and

when it is higher, pattern resolution deteriorates. Initially, a test pattern (see figure 3.4 (a)) was written on PR using DLW at various laser doses starting from 160 mJ/cm² to 320 mJ/cm² from which the optimum value of D_c was determined. Figures 3.4 (b) - (g) show the optical microscope images of the transferred pattern at these doses. From these images, it is clear that till 230 mJ/cm² (figure 3.4 (e)), pattern transfer is incomplete i.e. exposed PR still remains at some places, showing under exposure. This indicates that the laser power is not sufficient to reach till the end of PR thickness (i.e. $< D_c$) since its intensity falls as $I = I_0 e^{-ah}$, where ‘ a ’ is the absorption coefficient and ‘ h ’ is the thickness of PR. Further increase in laser dose (figure 3.4 (f)) was found to completely dissolve the exposed PR and the transferred pattern matches well with the mask pattern around ~270 to 275 mJ/cm². However, when the laser dose was increased beyond this value, the dimensions of the transferred patterns were found to reduce, indicating that the dose is $> D_c$ (see figure 3.4 (g)). When laser energy is greater than D_c , the light starts seeing the substrate leading

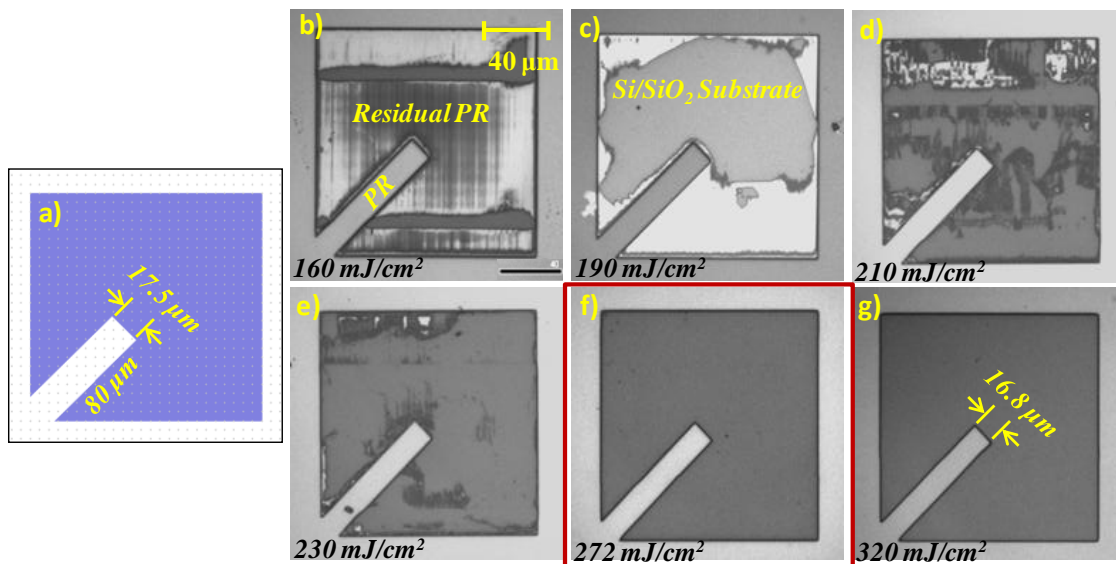


Figure 3.4. (a) MC test pattern used for estimating the critical laser dose “ D_c ”. (b) – (g) shows the optical microscope images of the transferred MC pattern on PR using DLW at various laser doses from 160 mJ/cm² to 320 mJ/cm². From this study, D_c for optimum pattern transfer was estimated to be 272 mJ/cm².

to scattering/ diffractions effects which eventually reduces the pattern dimensions [23]. From the foregoing discussions, it is clear that $D_c = 272 \text{ mJ/cm}^2$ and the same value was set in DLW, for effective pattern transfer.

3.2.3. Photoresist post baking temperature and time optimization

After successfully transferring the patterns on the PR, the sample was post-baked at 120°C on a hot plate for 10 minutes to improve its adhesion for subsequent etching of SiO_2 in BOE. Figure 3.5 (a) shows the transferred pattern on SiO_2 (after stripping the PR in acetone) along with the actual mask pattern (figure 3.5 (b)). From these figures, it is clear that the transferred pattern has slanted edges, which indicates the presence of undercutting.

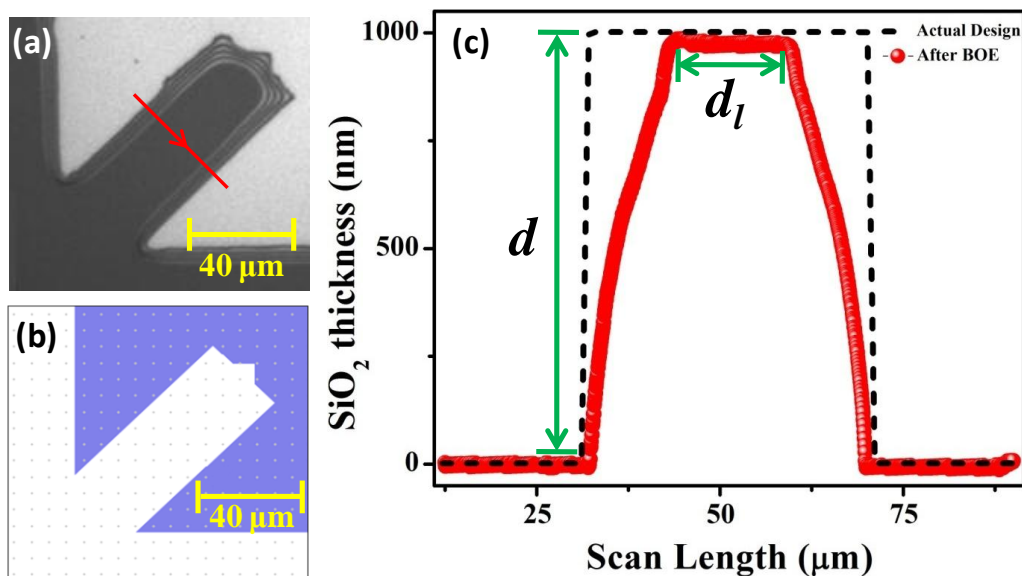


Figure 3.5. Photoresist post-baking temperature optimization. (a) Optical microscope image of the transferred MC pattern on SiO_2 after post-baking the PR at 120°C followed by BOE (b) along with the mask pattern used. (c) Dektak line profile of the transferred pattern along the width of the MC. The dotted line shows the actual mask pattern for comparison. From this data undercut ratio, U_R was estimated.

The undercutting is more evident from figure 3.5 (c), which shows the SiO_2 film thickness profile of the transferred MC pattern across its width, recorded using a Dektak

stylus profiler. It should be noted that there is always a natural degree of undercutting, as BOE being an isotropic etchant and thus penetrates in all directions, but the lack of PR adhesion on the substrate leads to the penetration of etchant along the substrate-resist interface and exaggerates the same [23]. In order to distinguish between these two effects, one can measure the undercut ratio (U_R), which is given by,

$$U_R = \frac{d}{d_l} \quad (3.1)$$

where, d and d_l are the thickness of SiO_2 and width of the MC measured at the top, respectively, as shown in figure 3.5 (c). If $U_R = 1$, undercutting is due to unavoidable isotropic BOE etching, whereas, if it is < 1 , it is due to improper adhesion of PR. From figure 3.5 (c), U_R was estimated to be 0.133, indicating the presence of severe undercutting and is indeed due to improper PR adhesion. Also, the concave profile of the undercutting observed from figure 3.5 (c) confirms that it is due to the poor photoresist adhesion and not due to inevitable undercutting in case of isotropic wet etching using BOE, which otherwise would have resulted in convex profile, as explained in figure 3.6.

Adhesion of PR on the substrate depends on several parameters such as the cleanliness of the wafer, its wettability, and PR post-baking temperature/time. Since the wafers used in the present work are thoroughly cleaned in *Piranha* solution, it was decided to study the parametric effect of post baking temperature and time. In order to find the optimum post-baking temperature (i.e. temperature for which undercutting is minimum), lithography experiment was repeated on five different samples with increasing post-baking temperatures from 120°C to 160°C in steps of 10°C . From the optical microscope images of the transferred patterns at these temperatures, U_R was estimated and is plotted against post-baking temperature in figure 3.7. From this figure it is clear that at 150°C , $U_R \sim 0.9$, and thereafter it remains constant, indicating the minimum achievable undercutting. Based

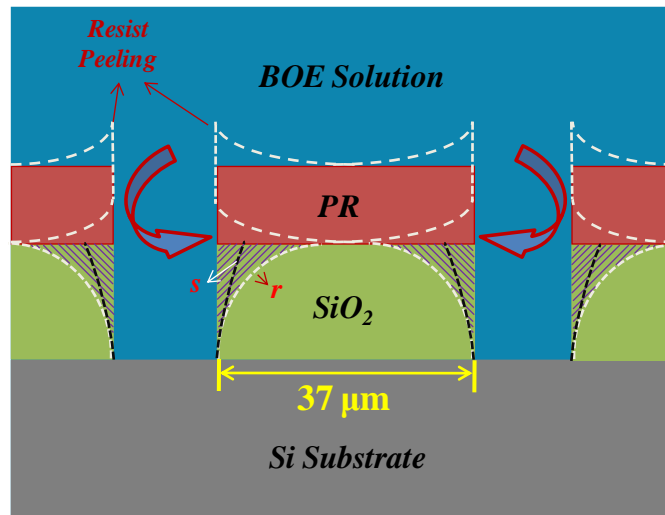


Figure 3.6. Role of PR adhesion on the SiO_2 undercutting during BOE (cross-section schematic). White (r) and black (s) dotted lines depict the resultant transferred pattern in SiO_2 due to resist peel off and inevitable undercutting in BOE.

on these experiments, therefore, in the present work, the post-baking temperature was fixed at 150°C . Inset of figure 3.7 shows the transferred MC pattern at this temperature, and it is evident from this figure that undercutting is substantially reduced compared to the sample post-baked at 120°C (see figure 3.5 (a)).

Experiments were also performed by varying the post-baking time from 5 minutes to 20 minutes, at a fixed post baking temperature of 150°C . We found that with increasing post-baking time, PR adhesion becomes better and thus reducing the undercutting. However, for the post-baking times greater than 10 minutes, the PR stripping in acetone became difficult. Based on these inputs, in the present work, the post-baking temperature and time were fixed at 150°C and 10 minutes respectively.

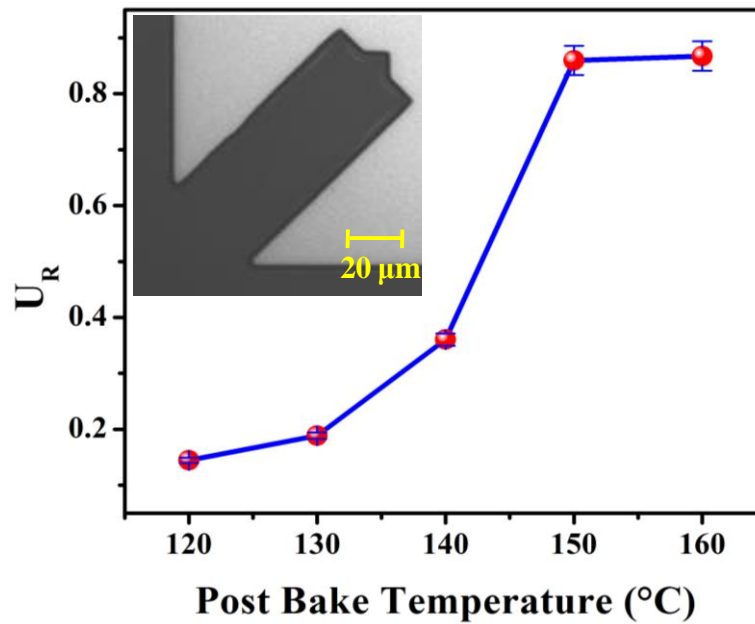


Figure 3.7. Plot between post-bake temperature and undercutting ratio, U_R . The inset shows the optical microscope image of the MC pattern after post-baking at 150°C with minimum undercutting.

3.2.4. Effective method to avoid ‘stiction’ during wet release of SiO_2 MCs

As explained earlier, SiO_2 MCs are usually stuck to the underlying Si substrate when released by wet chemical etching method (see figure 3.8 (a) and (b)). Taking a clue from the existing studies in literature, and after several trial and error experiments, in the present work, a two-step procedure was followed, to avoid the stiction. First, a sharp convex tip was introduced at the free end of the MCs which acts as an “anti-stiction tip” (see figure 3.8 (c)) and the fabrication process was repeated. It may be noted, dimensions and the shape of the anti-stiction tip was finalized after several iterations. With this modification, most of the MCs were successfully released as shown in figure 3.8 (d). This is attributed to the reduction in effective contact length at the free end of the MC across its width and the substrate from 37 μm (width of MC) to < 1 μm (size of the anti-stiction tip) during the rinse-dry cycle. Reduction in the contact area will reduce the amount of restoration force required by MCs against capillary forces and thus facilitates the release. Second, post-etch rinsing was performed in boiling DI water. This step further improved

the MC release yield. This is attributed to the reduction in surface tension of water to ~ 58.9 mNm^{-1} at 100°C (from ~ 72 mNm^{-1} at room temperature), which in turn reduces the capillary/ electrostatic forces between the MC and the substrate along with a reduction in drying time. It may be also due to the release of air bubbles trapped beneath the MCs, pushing the devices away from the substrate.

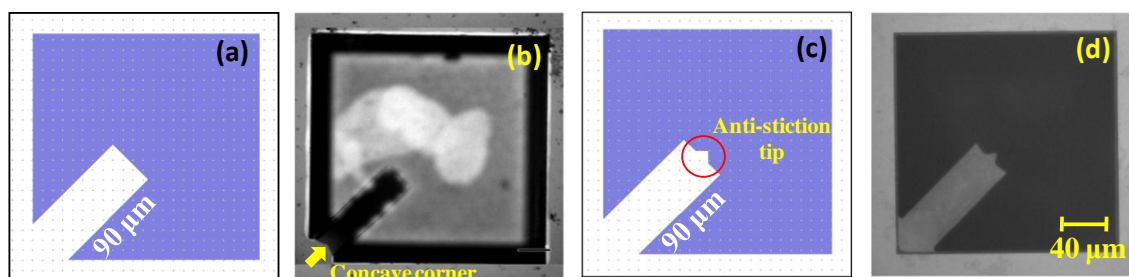


Figure 3.8. Typical mask file (a) without and (c) with anti-stiction tip along with the (b) stuck and (d) fully released MCs ($L = 90\ \mu\text{m}$), respectively, after TMAH etching of Si and immediate rinsing in DI water.

3.3. Fabrication of surface micro-patterned SiO_2 MCs

SiO_2 MCs ($210 \times 40 \times 0.98\ \mu\text{m}^3$) with controlled micro-patterns ($4\ \mu\text{m} \times 4\ \mu\text{m} \times (15 - 75)\ \text{nm}$) on their surface were fabricated using “two-layer lithography” process as shown in figure 3.9. Initially, “First mask layer” containing MC patterns was transferred on PR and subsequently on SiO_2 using DLW and buffered oxide etchant (BOE) solution, respectively (figure 3.9 (a) & (b)). Once the MC patterns transfer was satisfactory, the lithography step was repeated (on 50% of the devices) with the “second mask layer” to transfer the micro-patterns ($4\ \mu\text{m}^2$) on the surface of MC patterns (see figure 3.9 (c)). During this step, the desired depth of micro-patterns ($\sim 15 - 75\ \text{nm}$) on SiO_2 was controlled by optimizing the BOE etching time from 10 s to 50 s. Finally, the micro-patterned MCs were released by etching the underlying Si using TMAHw solution (figure 3.9 (d)).

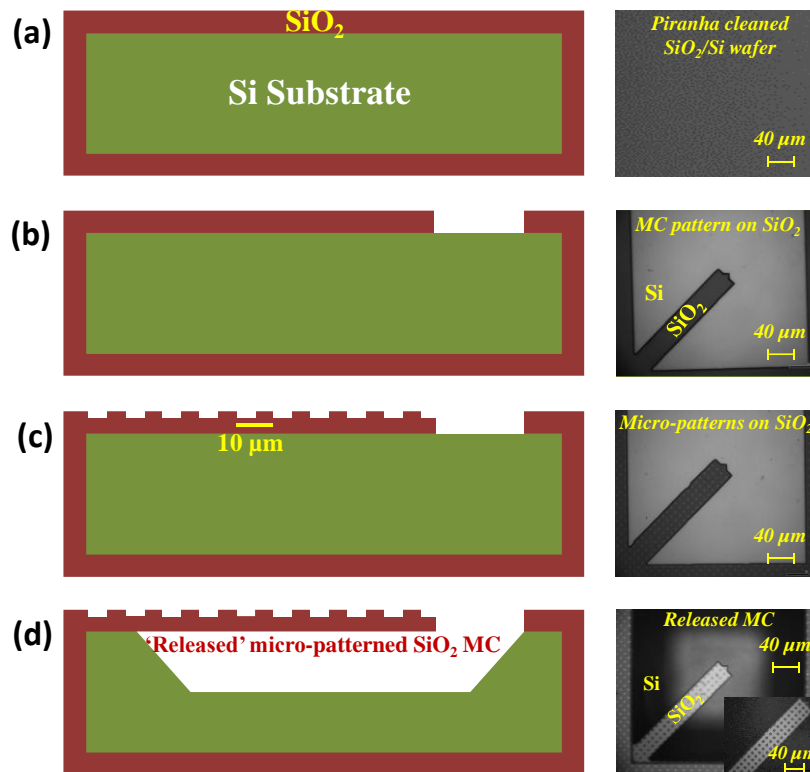


Figure 3.9. Schematic of the process steps involved in the fabrication of surface micro-patterned SiO_2 MCs along with the corresponding optical microscope images. (a) Starting material: Si {100} wafer with $\sim 0.98 \mu\text{m}$ thick SiO_2 , (b) MC pattern and (c) ordered surface micro-patterns ($4 \mu\text{m}^2$ with a pitch of $6 \mu\text{m}$) transferred on SiO_2 layer by a two-layer lithography process, (d) TMAHw etching of underlying Si to finally release MCs.

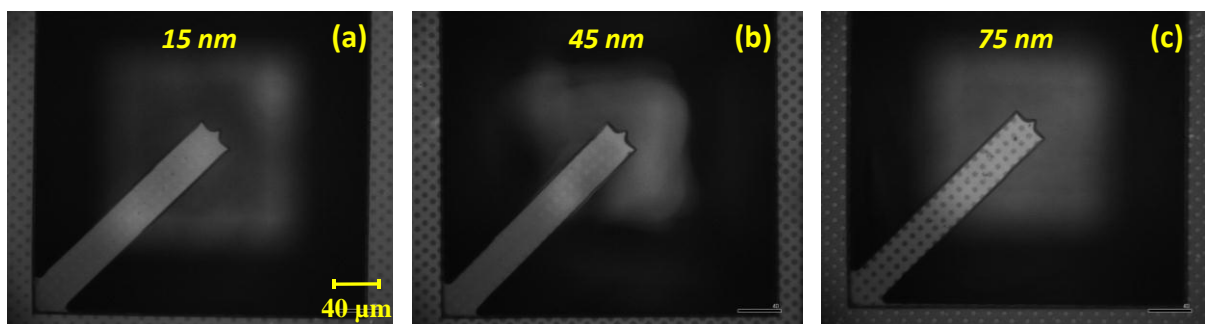


Figure 3.10. Typical optical microscope images of released MCs with controlled micro-patterns on their surface. From left to right depth of micro-patterns is increasing from 15 nm to 75 nm.

Figure 3.10 shows the optical microscope images of the typical MCs ($210 \times 37 \times 0.98 \mu\text{m}^3$) with increasing micro-pattern depth. The micro-patterns are more evident from figure 3.11

(a) where FESEM image of a typical micro-patterned SiO₂ MC is shown. Inset shows the magnified view of the free end of the MC, where micro-patterns are clearly visible. Depth of micro-patterns was thoroughly characterized (prior to the release of MC) using an AFM and a typical topological image of a micro-pattern is shown in figure 3.11 (b).

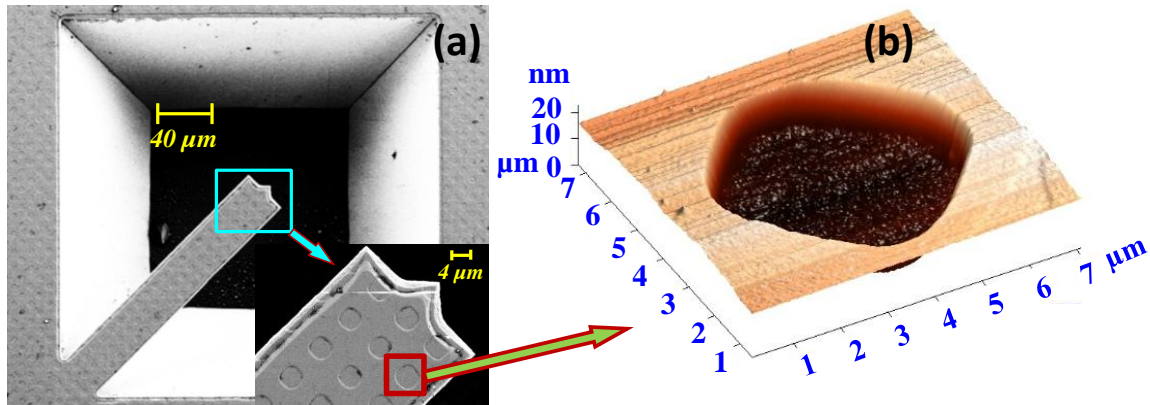


Figure 3.11. (a) FESEM image of a typical surface micro-patterned SiO₂ MC. Inset shows the magnified view of the free end of MC, where the micro-patterns are clearly seen. (b) Typical micro-pattern on a MC surface recorded using AFM. From this image depth of the pattern was estimated to be ~15 nm.

From AFM image analysis, depth of the micro-patterns was found to be ~ 15 nm. Similar measurements were performed at multiple places on the wafer, and the maximum error in depth was found to be ± 2 nm. It is also evident from this figure that the pattern size has marginally increased to ~4.5 μm than the designed value of 4 μm and the corners of the square pattern are rounded off. These features are attributed to the isotropic etching nature of BOE that is used to generate the micro-patterns on SiO₂. Similar measurements were repeated on all the MCs and the estimated micro-pattern depth along with the BOE etch time is shown in table 3.3.

Table 3.3. Optimized BOE etch time and the obtained pattern depth on the surface of SiO₂ MCs. Pattern dimensions was fixed at 4x4 μm².

| S.No. | BOE etch time (s) | Pattern depth (nm) |
|-------|-------------------|--------------------|
| 1. | 50 | 75 |
| 2. | 40 | 60 |
| 3. | 30 | 45 |
| 4. | 20 | 30 |
| 5. | 10 | 15 |

Once the fabrication process is complete, the wafers containing the released SiO₂ MCs with and without micro-patterns were carefully stored in a vacuum desiccator.

3.4. Characterization of SiO₂ MCs

3.4.1. Curvature measurements

Figure 3.12 (a) and (b) shows a typical 3D profile recorded using 3D OM and the extracted line profile across the length of a typical 110 μm long SiO₂ MC. From these figures, it is clear that the MC is released completely and is bending upwards, i.e. away from the wafer by ~ 3.6 μm. The out of plane deflection of the MC is attributed to the presence of gradient residual stress, inherently introduced during the SiO₂ film growth by thermal oxidation of c-Si. Similar measurements were repeated on all the MCs and peak deflection magnitude (z_{\max}) in each case was extracted.

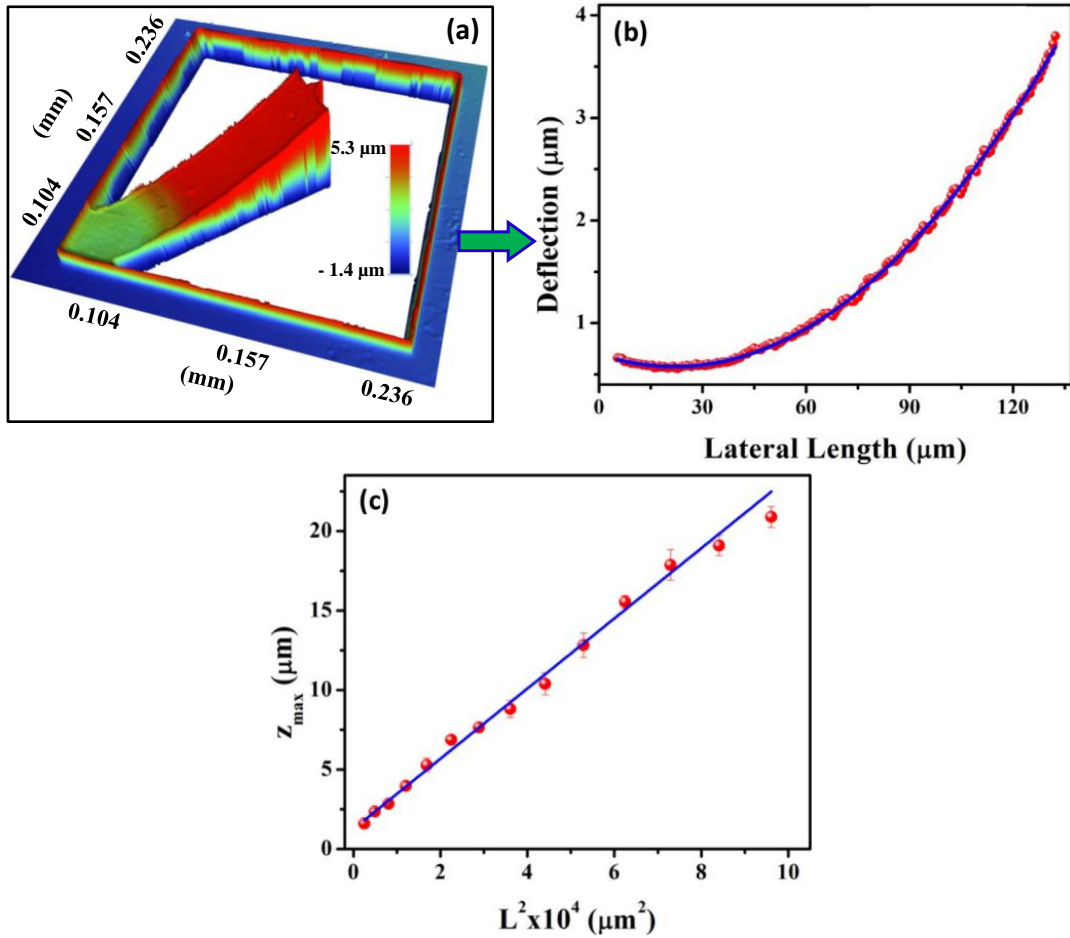


Figure 3.12. (a) Typical 3D profile of a released $110 \mu\text{m} \times 37 \mu\text{m} \times 0.98 \mu\text{m}$ SiO_2 MC. (b) Line profile of the same MC across its length (shown as a white line in (a)). Out of plane deflection seen in this figure indicates the presence of inherent gradient residual stress in the SiO_2 film. (c) Peak deflection vs. square of the length of the MCs fabricated in the present work. From the slope of the linear fit of this data, gradient stress in the film was estimated to be 15.14 ± 0.32 MPa.

The residual stress was estimated from a linear plot of z_{max} vs. the square of the length of MCs (L^2), as shown in figure 3.12 (c). The linearity seen in this figure clearly validates the deflection magnitude measurements. From the slope of the linear fit, the peak gradient stress (σ_{max}) was estimated using the relation, $\sigma_{\text{max}} = ETz_{\text{max}}/L^2$ [25], where E, T and L are Young's modulus, thickness and length of the MC, respectively. By substituting, $E = 70$ GPa, $T = 0.98 \mu\text{m}$, $z_{\text{max}}/L^2 = 220.774 \text{ m}^{-1}$, σ_{max} in SiO_2 film used in the present work was estimated to be $15.14 \text{ MPa} \pm 0.32 \text{ MPa}$. Unlike mean stress, stress

gradient is anti-symmetric about the MC mid-plane and is a result of more localized effects like atomic diffusion through the film/substrate interface, interstitial or substitutional defects and atomic peening [24]. While studying the mean and gradient residual stress in SiO₂ MCs released by wet chemical etching method, Fang et al [24], reported σ_{\max} of 2.18 MPa, which is an order less compared to the values observed in the present work, whereas, Tsou et al [26] reported a value of 10.85 MPa in their SiO₂ MCs of similar dimensions. Laconte et al [27], from their measurements on much thinner SiO₂ MCs, generalized the stress gradient to be 17 MPa/0.1 μm . These results are summarized in table 3.4 along with the value obtained in the present work. From this table it is clear that the stress values estimated by various authors differ by an order. It should be noted that the stress profile across the thickness of the SiO₂ film is complicated and depends a lot on its growth conditions. A change in stress in a very small section of the layer can have an important effect on the MC deflection and accordingly on the determined stress gradient. Notably, this gradient residual stress induced curvature gives rise to certain artifacts in the deflection sensitivity measurements [28] and can influence the stiffness of MCs [29]. Therefore, care must be exercised while interpreting such results.

Table 3.4. Comparison of gradient residual stress values reported in SiO₂ films, obtained from MC bending measurements.

| <i>S. No.</i> | Reference | Typical MC dimensions | σ_{\max} (MPa) |
|---------------|------------------|--|-----------------------|
| 1. | [24] | L = 50 – 150 μm , L = 20 μm , T = 1 μm | 2.18 |
| 2. | [26] | L = 20 – 140 μm , W = 10 μm , T = 1 μm | 10.85 |
| 3. | [27] | L = 100 μm , W = 10 μm , T = 0.3 μm | 17 |
| 4. | This work | L = 50 – 330 μm, W = 37 μm, T = 0.98 μm | 15.14 |

3D OM measurements were also performed on micro-patterned MCs. Typical line profiles across the length of micro-patterned MCs of varying pattern depths (15 – 75 nm) along with a profile of unpatterned MC is shown in figure 3.13 (a). As expected, the line profiles measured on these devices are not smooth due to the presence of trenches across the line of measurement. Similar measurements were repeated on at least 10 devices from each sample and their mean peak deflection value (z_{\max}) is plotted as a function of pattern depth in figure 3.13 (b). From these figures, it is evident that z_{\max} value does not follow any trend with increasing pattern depth and the variation with respect to unpatterned one remains within $\pm 20\%$.

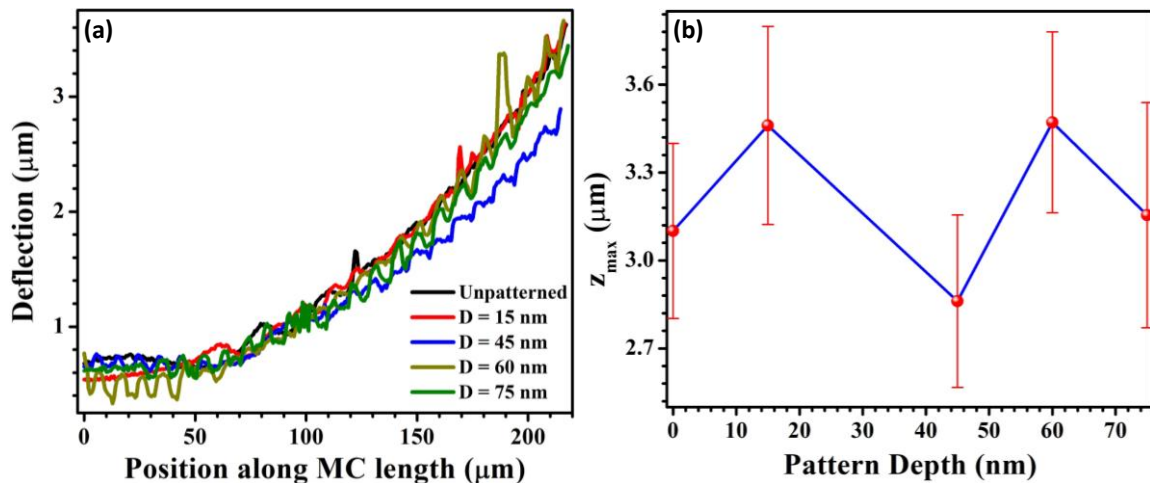


Figure 3.13. (a) Typical deflection profiles across the length of the micro-patterned MCs. For comparison, profile recorded on unpatterned MC is also shown. (b) Plot of peak bending magnitude estimated from the bending profiles as a function of pattern depth.

3.4.2. Resonance frequency measurements

Resonance frequencies of MCs of varying lengths were measured using NVA as explained in section 2.4 of chapter 2. Figure 3.14 shows a typical resonance spectrum of 210 μm long MC along with Lorentzian fit, from which f_0 , Δf and Q-factor values were estimated to be 18.91 kHz, 0.64 kHz and 29.51, respectively. Similar measurements were repeated on all the MCs (of various lengths) and f_0 and Q-factor values were extracted. It

may be noted, for a given dimension, resonance frequency measurements were repeated on at least 5 MCs.

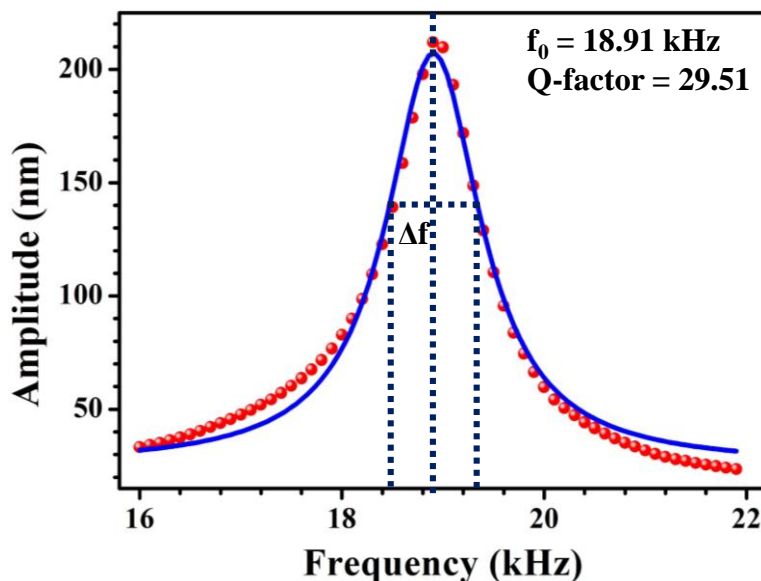


Figure 3.14. Typical resonance spectrum of a MC recorded using NVA and from the Lorentzian fit resonance frequency and Q-factor values were extracted. In this figure, the Δf is the full width at $\sqrt{2}$ times the maximum amplitude.

From Eq. (1.17) we know that,

$$f_n = \frac{\lambda_n^2}{2\pi\sqrt{12}} \frac{T}{L^2} \sqrt{\frac{E}{\rho}} \quad (3.2)$$

which predicts a linear relationship between the resonance frequency and square of the reciprocal length of MCs ($1/L^2$). By substituting the values of λ_n , T , E and ρ (1.857, 0.98 μm , 70 GPa and 2650 kg/m^3) in Eq. (3.2), the resonance frequencies of various MCs ($L=50 - 330 \mu\text{m}$, $W=37 \mu\text{m}$, $T=0.98 \mu\text{m}$) fabricated in the present work were estimated and are plotted against $1/L^2$ along with the experimentally measured values in figure 3.15. From this figure, it is clear that the experimentally measured resonance frequency deviates from the linear dependence predicted by Eq. (3.2) and the deviation is more pronounced for smaller MCs. This is attributed to the deviations in physical dimensions of MCs fabricated by wet chemical etching method [32].

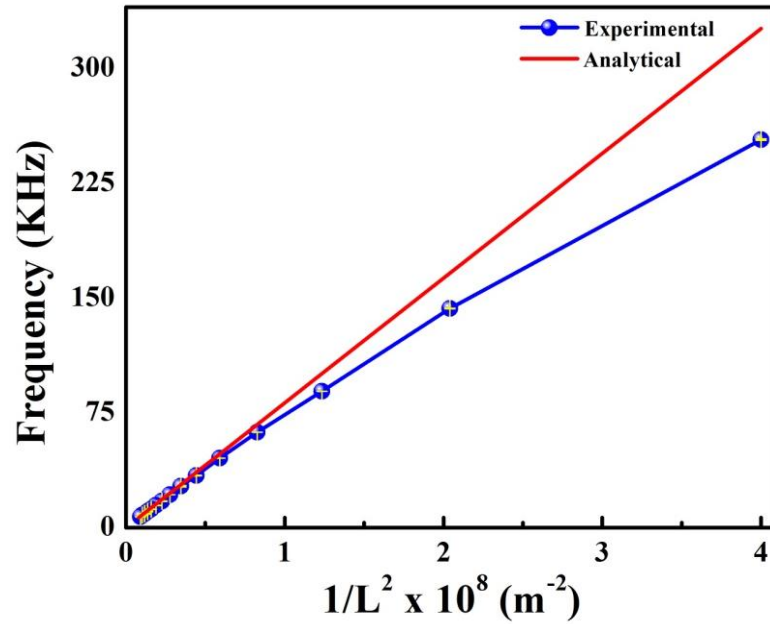


Figure 3.15. Analytical and the experimental resonance frequency of MCs with the inverse square of length (L) (error bar is of the symbol size in the experimental data).

It is well known that the MCs patterned by isotropic wet etching results in beams of non-rectangular cross-section (see figure 3.16 (a)) with a different I/A ratio compared to rectangular beams [33]. Also, an undercutting at the fixed end is inherent in these structures as they are released by the wet chemical method, which increases the effective length leading to a decrease in resonance frequency. Correction required in resonance frequency estimation of these MCs due to the foresaid effects will be discussed now.

When pattern transfer of SiO_2 MCs is effected with an isotropic etchant like BOE, the beam sidewalls profile can be approximated by arcs of circles (see figure 3.16 (b)) leading to a different I and A as given by [33],

$$I = \frac{WT^3}{12} \left[\frac{1 + (12 - 7\pi/2)T/W + (44/3 - 7\pi + 3\pi^2/4)T^2/W^2}{1 + (2 - \pi/2)T/W} \right] \quad (3.3.1)$$

$$A = WT + 2(1 - \pi/4)T^2 \quad (3.3.2)$$

where, the symbols have their usual meaning. The correction factor (β) in the estimated resonance frequency with respect to rectangular MC is given by,

$$\beta = \frac{(I/A)}{(I/A)_{rect}} - 1 \quad (3.4)$$

By substituting the values of W and T in Eq. (3.3) & (3.4), β for the present MCs was estimated to be 0.001% and is independent of MC length. However, the deviation in the observed frequency is as high as $\sim 30\%$ for the smallest MC, indicating that the frequency shift cannot be explained by non-rectangular cross-section alone.

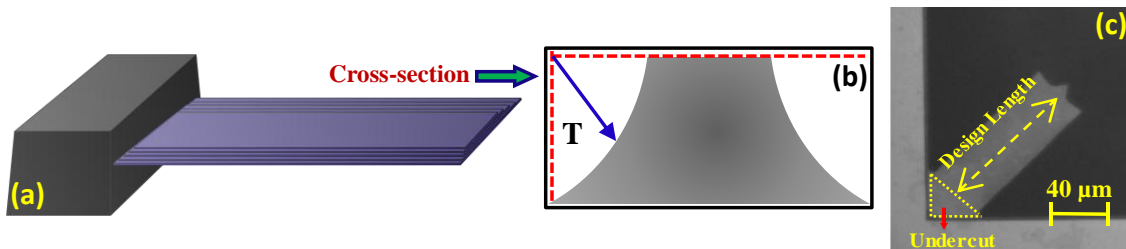


Figure 3.16. (a) Schematic of MC with non-rectangular cross-section and (b) cross-sectional view of the MC patterned by isotropic wet etching. The magnitude of asymmetry is exaggerated for clarity. (c) Optical microscope image of a typical SiO_2 MC released in the present work. Undercut region at the fixed end is shown by a triangle.

SiO_2 MCs fabricated in the present work are released by wet chemical etching of underlying Si using TMAHw solution, which results in an undercutting at the fixed end of these structures. The effect of undercutting on resonance frequencies can be modelled by including extra length ΔL at the fixed end of the designed rectangular MCs (see figure 3.16 (b)), where ΔL is independent of MC length [32]. ΔL was estimated by performing least square fit on the resonance frequency vs. MC length data using a function $f(x) = m/(L + \Delta L)^2 + c$ as shown in figure 3.17 (a) and it was found to be $7.01 \mu\text{m}$.

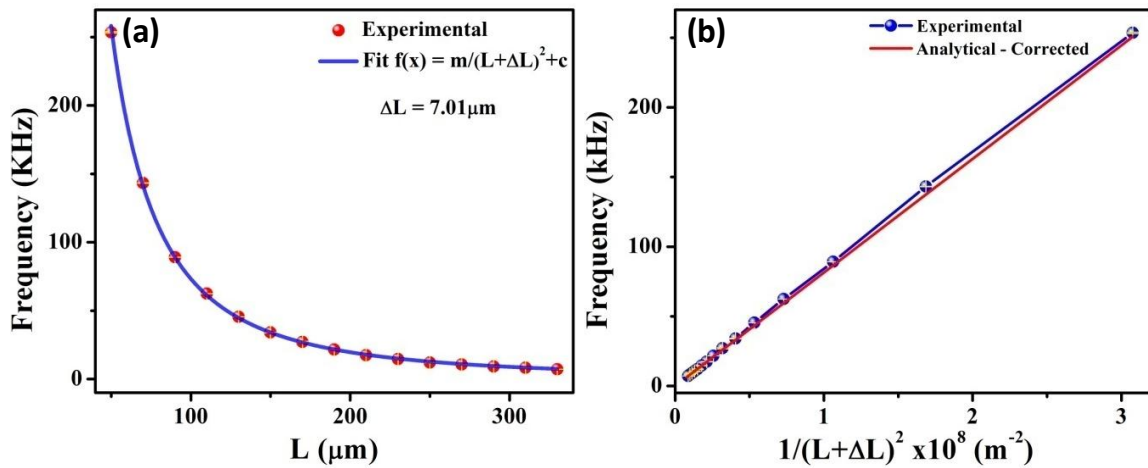


Figure 3.17. (a) Experimental resonance frequency with the length of MCs and is fitted to $f(x) = m/(L + \Delta L)^2 + c$ by the least square method to estimate the ΔL . (b) Experimental and analytical resonance frequency with the inverse square of corrected effective length. Collapse of these two data on each other indicates that the leading correction in resonance frequency estimation comes from extra length introduced due to undercutting.

Now the resonance frequency of MCs was estimated with the new effective length and is plotted against $1/(L + \Delta L)^2$ along with the experimentally measured frequency in figure 3.17 (b). Both the data collapse on each other in this figure, thereby establishing that major correction in resonance frequency estimation indeed comes from the effect of undercutting in SiO₂ MCs released by wet chemical etching method. Interestingly, the length correction also influences the gradient residual stress estimation and was estimated to be $14.43 \pm 0.28 \text{ MPa}$ with $(L + \Delta L)$, which is only $\sim 5\%$ lower than that of without correction.

The dependence of Q – factor on the resonance frequency of the MCs of various lengths was also investigated and is shown in figure 3.18. From this figure it is clear that the Q-factor linearly increases with increasing frequency till $\sim 150 \text{ kHz}$, to a value of ~ 93 and thereafter it seems to saturate. It is to be noted, in the present work, all the frequency measurements were performed in air at ambient pressure ($\sim 10^5 \text{ Pa}$) and hence explains the

lower Q – factor obtained in these devices [34]. The saturation of Q – factor above 150 kHz can be attributed to the air viscous damping at ambient pressures [35].

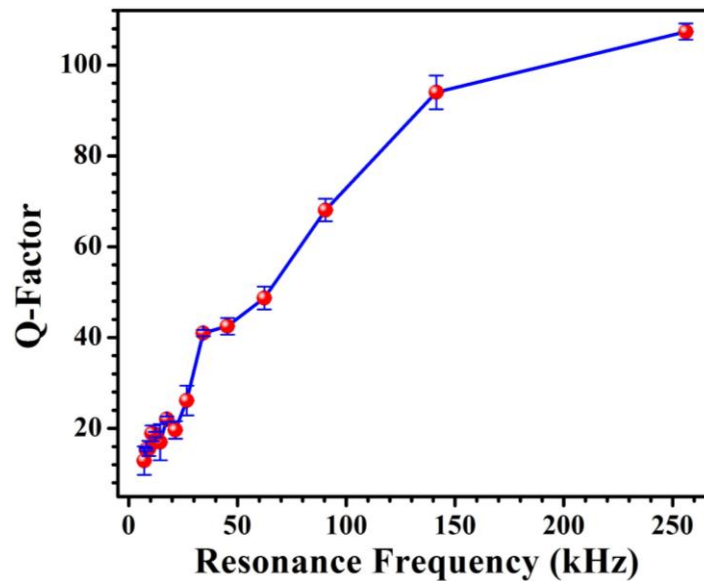


Figure 3.18. Experimentally estimated Quality factor of the released MCs as a function of their respective resonance frequencies.

Resonance frequency measurements were also performed on micro-patterned MCs. Figure 3.19 (a) shows the resonance spectra of typical micro-patterned MCs of various depths (15 – 75 nm) along with the corresponding Lorentzian fit. For comparison, the resonance spectrum of a typical unpatterned MC is also shown in this figure. From this figure, resonance frequency and Q-factor values were estimated and their variation with pattern depth is shown in figure 3.19 (b). From this figure, it is evident that both f_0 and Q-factor values decrease with increasing pattern depth. The decrease in resonance frequency can be attributed to the competing effects of marginal decrease in effective thickness of the MCs and the corresponding reduction in mass and is in accordance with FEM simulation results. Reduction in Q-factor may be due to the enhanced viscoelastic damping on the surface introduced by micropatterns.

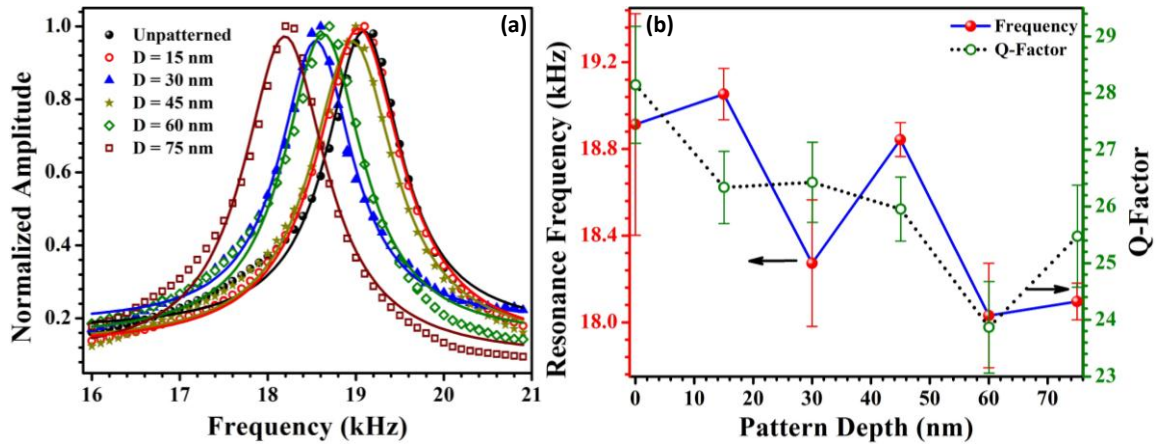


Figure 3.19. (a) Typical resonance frequency spectra of micro-patterned MCs. For comparison, resonance spectrum of an unpatterned MC is also shown. From the Lorentzian fit, resonance frequency and Q-factor values were estimated. (b) Mean resonance frequency (blue solid line) and Q-factor (green dotted line) of MCs as a function of pattern depth. In this figure 0 nm pattern depth denotes the frequency of unpatterned MCs.

3.5. Summary

In summary, SiO₂ MC of various dimensions are successfully fabricated using DLW unit and wet chemical etching methods. Various micro-fabrication process parameters were optimized and are summarized (Table 3.1 & Table 3.2). It is shown that, even for fabricating simple structures like MCs, DLW can be a valuable tool, if optimizations at design level are desired. It is shown that introduction of a sharp convex tip at the free end of the MC along with a post-etch rinsing in boiling DI water, which are otherwise considered separately, reduces the stiction substantially, even in the longest MCs ($L = 330 \mu\text{m}$) studied in the present work. From the initial bending measurements on the released MCs, gradient residual stress present in the SiO₂ film was estimated and found to be $15.14 \pm 0.32 \text{ MPa}$. It is shown that, compared to the role of non-rectangular cross-section of SiO₂ MCs, presence of undercutting, which increases the effective length by $\sim 7.01 \mu\text{m}$, influences the resonance frequency estimation most, especially at smaller lengths. From the resonance frequency measurements, Q-factor values were estimated and found to

increase linearly with increasing frequency till ~ 150 kHz, to a value of ~ 93 and thereafter it seems to saturate. The saturation of Q – factor above 150 kHz is attributed to the air viscous damping at ambient pressures. Further, micro-patterned MCs were fabricated using two-layer lithography process. Presence of micro-patterns does not seem to influence the bending characteristics of SiO₂ MCs. Resonance frequency measurements on micro-patterned MCs revealed that both resonance frequency and Q-factor values reduces marginally with respect to unpatterned ones.

3.6. References

- [1] V. Jović, J. Lamovec, M. Popović, Ž. Lazić, Fabrication of SiO₂ - based microcantilevers by anisotropic chemical etching of (100) single crystal Si, J. Serbian Chem. Soc. 72 (2007) 1127–1138.
- [2] Y. Tang, J. Fang, X. Yan, H.F. Ji, Fabrication and characterization of SiO₂ microcantilever for microsensor application, Sensors Actuators, B Chem. 97 (2004) 109–113.
- [3] B. Bin Xu, Y.L. Zhang, H. Xia, W.F. Dong, H. Ding, H.B. Sun, Fabrication and multifunction integration of microfluidic chips by femtosecond laser direct writing, Lab Chip. 13 (2013) 1677–1690.
- [4] J.A. Lewis, G.M. Gratson, Direct writing in three dimensions, Mater. Today. 7 (2004) 32–39.
- [5] A. Singh, G. Scotti, T. Sikanen, V. Jokinen, S. Franssila, Laser direct writing of thick hybrid polymers for microfluidic chips, Micromachines. 5 (2014) 472–485.

- [6] S. Ghosh, G.K. Ananthasuresh, Note on high aspect-ratio SU-8 micromechanical structures using mask-less direct laser writing. ASME. International manufacturing science and engineering conference, ASME 2012 international manufacturing science and, Eng. Conf. (2012) 1001 – 1007.
- [7] M.G. Ivan, J. Vaney, D. Verhaart, E.R. Meinders, S.M.B. V, Direct Laser Write (DLW) as a Versatile Tool in Manufacturing Templates for Imprint Lithography on Flexible Substrates, 7271 (2009) 1–8.
- [8] E. Forsén, P. Carlberg, L. Montelius, A. Boisen, Laser lithography on resist bi-layer for nanoelectromechanical systems prototyping, *Microelectron. Eng.* 73–74 (2004) 491–495.
- [9] C.B. Arnold, R.C. Wartena, B. Pratap, B. Shashishekar, A. Piqu, K.E. Swiderlyons, D.W. Weir, R.A. Kant, Laser direct-write of miniature sensor and microbattery systems, 50 (2003) 57–62.
- [10] M. Flury, A. Benatmane, P. Gérard, P.C. Montgomery, J. Fontaine, T. Engel, J.P. Schunck, E. Fogarassy, Excimer laser ablation lithography applied to the fabrication of reflective diffractive optics, in: *Appl. Surf. Sci.*, 2003: pp. 238–244.
- [11] M. Schrödner, R.I. Stohn, K. Schultheis, S. Sensfuss, H.K. Roth, Polymer field effect transistors made by laser patterning, *Org. Electron.* 6 (2005) 161–167.
- [12] R. Mishra, T.K. Maiti, T.K. Bhattacharyya, Structural comparison of SU-8 microtubes fabricated by direct laser writing and UV lithography, *Proc. IEEE Sensors*. 2017-Decem (2017) 7–9.
- [13] M.P. Lim, X. Guo, E.L. Grunblatt, G.M. Clifton, A.N. Gonzalez, C.N. LaFratta, Augmenting mask-based lithography with direct laser writing to increase resolution and speed, *Opt. Express*. 26 (2018) 7085.

- [14] H. Chandralim, Q. Chen, A.A. Said, M. Dugan, X. Fan, Monolithic optofluidic ring resonator lasers created by femtosecond laser nanofabrication, *Lab Chip*. 15 (2015) 2335–2340.
- [15] R.D. Jolly, Miniature Cantilever Beams Fabricated by Anisotropic Etching of Silicon, *J. Electrochem. Soc.* 127 (1980) 2750.
- [16] J.W. Rogers, T.J. Mackin, L.M. Phinney, A thermomechanical model for adhesion reduction of MEMS cantilevers, *J. Microelectromechanical Syst.* 11 (2002) 512–520.
- [17] T. Abe, W.C. Messner, M.L. Reed, Effects of elevated temperature treatments in microstructure release procedures, *J. Microelectromechanical Syst.* 4 (1995) 66–75.
- [18] C.-J. Kim, J.Y. Kim, B. Sridharan, Comparative evaluation of drying techniques for surface micromachining, *Sensors Actuators A Phys.* 64 (1998) 17–26.
- [19] M. Joshi, V.R. Rao, S. Mukherji, A novel technique for microfabrication of ultra-thin affinity cantilevers for characterization with an AFM, *J. Micromechanics Microengineering*. 20 (2010).
- [20] N. Tas, T. Sonnenberg, H. Jansen, R. Legtenberg, M. Elwenspoek, Stiction in surface micromachining, *J. Micromechanics Microengineering*. 6 (1996) 385–397.
- [21] T. Abe, W.C. Messner, M.L. Reed, Effective methods to prevent stiction during post-release-etch processing, *Proc. IEEE Micro Electro Mech. Syst.* 1995. (1995) 94.
- [22] K. Prabakar, M. Raghuramaiah, S. Balasubramanian, S. Midhya, P. Avinash, S.T. Sundari, Residual stress in underlying silicon at the fixed end of SiO₂ microcantilevers — A micro-Raman study, *Mod. Phys. Lett. B.* 33 (2018) 1850419.

- [23] Application note, Microchemicals, Germany, 2013, www.microchemicals.com/downloads/application_notes.html
- [24] W. Fang, J.A. Wickert, Determining mean and gradient residual stresses in thin films using micromachined cantilevers, *J. Micromechanics Microengineering*. 6 (1996) 301–309.
- [25] N. Lobontiu, E. Garcia, *Mechanics of microelectromechanical systems*, 2005.
- [26] C. Tsou, Y.S. Huang, H.C. Chang, On the Determination of Thermal Expansion Coefficient of Thermal Oxide, *Tech. Proc. 2005 NSTI Nanotechnol. Conf. Trade Show*. 3 (2005) 339–342.
- [27] J. Laconte, F. Iker, S. Jorez, N. André, J. Proost, T. Pardoën, D. Flandre, J.P. Raskin, Thin films stress extraction using micromachined structures and wafer curvature measurements, *Microelectron. Eng.* 76 (2004) 219–226.
- [28] M.X. Shi, B. Liu, Z.Q. Zhang, Y.W. Zhang, H.J. Gao, Direct influence of residual stress on the bending stiffness of cantilever beams, *Proc. R. Soc. A Math. Phys. Eng. Sci.* 468 (2012) 2595–2613.
- [29] A.N. Sohi, P.M. Nieva, Frequency response of curved bilayer microcantilevers with applications to surface stress measurement, *J. Appl. Phys.* 119 (2016).
- [30] A. Boisen, S. Dohn, S.S. Keller, S. Schmid, M. Tenje, Cantilever-like micromechanical sensors, *Reports Prog. Phys.* 74 (2011) 036101.
- [31] C.L. Dai, Y.M. Chang, A resonant method for determining mechanical properties of Si_3N_4 and SiO_2 thin films, *Mater. Lett.* 61 (2007) 3089–3092.
- [32] K. Babaei Gavan, E.W.J.M. Van Der Drift, W.J. Venstra, M.R. Zuiddam, H.S.J. Van Der Zant, Effect of undercut on the resonant behaviour of silicon nitride cantilevers, *J. Micromechanics Microengineering*. 19 (2009).

- [33] H. Bourouina, R. Yahiaoui, E. Yusifli, M.E.A. Benamar, K. Ghoumid, G. Herlem, Shear effect on dynamic behavior of microcantilever beam with manufacturing process defects, *Microsyst. Technol.* 23 (2017) 2537–2542.
- [34] R. Sandberg, K. Mølhave, A. Boisen, W. Svendsen, Effect of gold coating on the Q-factor of a resonant cantilever, *J. Micromechanics Microengineering.* 15 (2005) 2249–2253.
- [35] F.R. Blom, Dependence of the quality factor of micromachined silicon beam resonators on pressure and geometry, *J. Vac. Sci. Technol. B Microelectron. Nanom. Struct.* 10 (1992) 19.

Chapter 4

Effect of biaxial curvature on the resonance frequency and high-temperature annealing on the bending properties of microcantilevers

In this chapter, as a prelude to RH sensing studies, 1) the effect of inherent biaxial curvature on the resonance frequency of SiO₂ MCs and 2) post-release annealing on the evolution of residual stress in these devices, are investigated in detail. In the first part, the resonance frequencies of the released MCs were measured using LDV and compared with FEM simulation results. The difference between the experimental and FEM simulated values is attributed to the presence of biaxial curvature in these MCs. The curvature present in the MCs was measured independently using a 3D OM. The role of MC dimensions vis-à-vis curvature on the observed frequency shift is discussed in detail. Finally, the experimental data from the present work are compared with the experimental works reported in the literature and existing theoretical models. In the second part, the effect of post-release high-temperature annealing (800 °C and 1000°C) in different environments (O₂ and N₂) on the residual stress evolution of SiO₂ MCs are presented. These studies revealed that, irrespective of annealing environment (i.e. O₂ or N₂), both mean and gradient residual stress values increase with increasing annealing temperature. Interestingly, no such increase was seen in samples that are annealed prior to the final release of MCs. These results are explained based on the onset of plastic deformation and stress accumulation at the free end of MCs with annealing.

4.1. Effect of biaxial curvature on the resonance frequency of SiO₂ MCs

4.1.1. Introduction

SiO₂ or Si₃N₄ MCs are bent usually away from the underlying Si wafer when released by wet chemical etching methods. As discussed in chapter 3, this is due to the presence of gradient residual stress (compressive) introduced during the growth of thin film at high temperatures [1]. Similarly, to enhance the reflectivity [2] or for immobilizing biological receptors such as antibodies [3], MCs are usually coated with a metal layer such as gold on their surface. When subjected to small amounts of heat, these devices exhibit biaxial curvature due to the difference in thermal expansion coefficients of their constituent layers. Presence of such biaxial curvature can induce non-linear stiffening and can significantly influence the MC stiffness [4]. Apart from the fabrication-induced curvature, when explored for sensor applications, adsorption-induced surface stress can also influence the stiffness of the MCs [5].

MCs are usually operated either in static or dynamic mode, depending upon the application. In general, static and dynamic modes of operation of MCs are considered to be independent of each other and within the framework of classical beam theory, it is assumed that the surface stress generated during adsorption does not influence the stiffness of MCs. However, several experimental studies [5–10] reported in the literature show otherwise and demonstrate that the surface stress can indeed significantly affect the stiffness of the MCs and the effect can be of the order of the adsorption-induced frequency shifts. Even though several theoretical models are proposed in the literature [11–19], the origin of surface stress induced stiffness changes in MCs still remains elusive.

Curvature/surface stress induced stiffness change also critically depends on MC shape/ dimensions and only a few authors have addressed this problem. For example,

Lachut and Sader [14–16] found that compared to rectangular MCs, V-shaped MCs are more prone to surface stress induced stiffness changes [15]. While studying the non-linear effect of differential surface stress on the resonance frequency of MCs with high aspect ratios, Tamayo et al [17] concluded that the resonance frequency shift in these devices is always positive irrespective of the sign of the surface stress. Lakshmoji et al [20] studied the effect of adsorption induced surface stress vis-à-vis MC dimensions on the stiffness of uncoated Si MCs and found that the stiffness of MCs increases linearly with the surface stress scaled with the cube of width to thickness (W/T) ratio of MCs. Sohi et al [4] studied the role of microfabrication-induced biaxial curvature on the resonance frequency of gold-coated MCs with increasing W/T ratios. By performing strain analysis using their model, they concluded that, in the case of wider MCs, the observed frequency shift is mostly due to the increasing contribution of in-plane stretching displacement and not due to the flexural stretching mode coupling. The role of biaxial curvature leading to internal stresses and its consequences on the resonance frequency was demonstrated by Pini et al [18] in MC plates made of paper sheets. They showed that the internal stress couple with bending moments in these structures, which increases the magnitude of stiffness by several factors. Further pursuing the studies in ref. [18], Ruz et al [19] developed a theoretical framework to explain the role of width to length (W/L) and Poisson's ratios on eigen frequencies. They showed that when $W/L < 0.1$, eigenfrequencies are dominated by non-linear beam effect and are independent of MC width. In contrast to this, when $W/L > 0.2$, non-linear plate effect dominates, and frequency rapidly increases as $(W/L)^4$. They also pointed out that, Poisson's ratio can strongly influence the frequency response of wider MCs.

From the forgoing scan of literature, it is clear that most of the dimensional dependence studies are analytical in nature and exhaustive experimental investigation using a wide range of MC dimensions is still lacking. This will be the topic of the present

chapter, where we have studied the effect of fabrication induced biaxial curvature vis-à-vis MC dimensions on the stiffness of uncoated SiO₂ MCs. The idea of using as-fabricated MCs is novel because it provides insight on the role of curvature arising due to gradient residual stress inherently present in SiO₂ film and not influenced by any extraneous coating. The resonance frequencies of the released MCs were measured using a LDV and compared with FEM simulation results. The difference between the values obtained from the experiment and FEM simulation is attributed to the presence of biaxial curvature in these MCs. The curvature present in the MCs was measured independently using a 3D OM. The role of MC dimensions vis-à-vis curvature on the observed frequency shift is discussed in detail. Finally, the experimental data from the present work is compared with experimental works reported in the literature and various existing theoretical models.

4.1.2. Results and discussion

Resonance frequencies of the MCs of varying length were measured using LDV and its variation with MC length is shown in figure 4.1. It is evident from this figure that the resonance frequency variation has the expected $1/L^2$ dependence. Resonance frequency values of all the MCs were also estimated from FEM simulations, using commercial software package *Intellisuite* as shown in the inset of figure 4.1 and were compared with experimentally observed resonance frequency values.

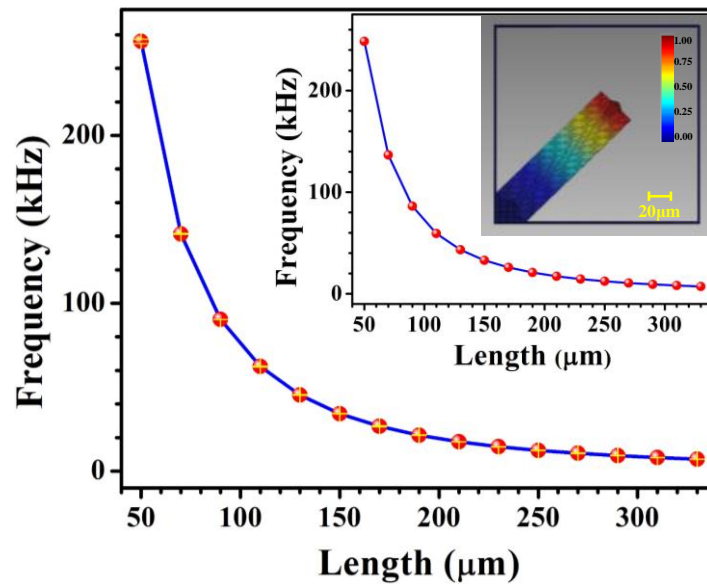


Figure 4.1. Experimentally measured resonance frequency of MCs versus their length. Here error bar is of the size of the symbol. Inset shows the similar plot with FEM simulated values. Inset also shows the snapshot of meshed ($1 \mu\text{m}^3$) MC structure used for simulations. In this figure, the color code represents the amplitude of vibration and it can be clearly seen that the amplitude is maximum at its free end.

Figure 4.2 shows the relative difference between the experimentally measured resonance frequencies of the MCs with the corresponding FEM simulated values with increasing W/L of MCs. From this figure, it is clear that the difference is positive and is $<1\%$ when $W/L < 0.16$ and thereafter it rapidly increases, reaching a maximum value of 5% at $W/L = 0.35$ and then it reduces again with a further increase in W/L value, upto $W/L \sim 0.7$.

The observed positive and complex frequency shift between experimental and FEM values can be due to the following reasons. 1) Variation in physical dimensions (length and thickness) of the MCs, 2) Details of the fixed end i.e. clamping conditions, 3) E , ρ values considered for FEM simulations, 4) Viscoelastic property of the medium (air) in which the MCs are immersed, and 5) Inherent curvature present in MCs increasing their

stiffness. We now analyze each of these cases to understand their contribution to the observed frequency shift.

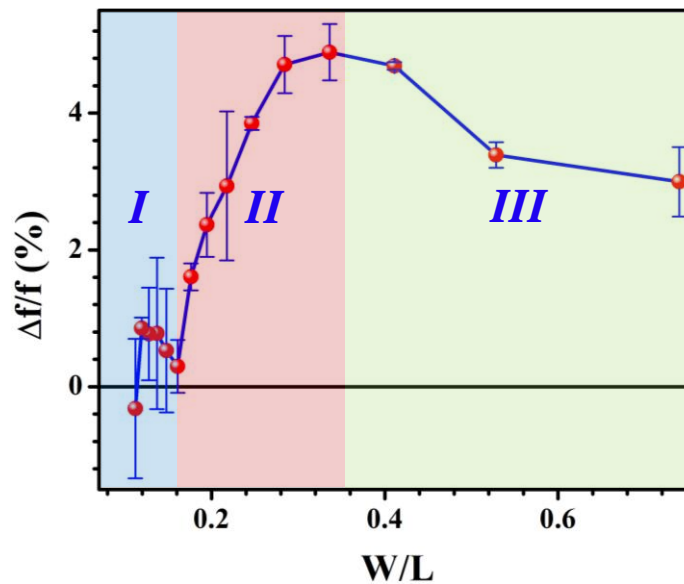


Figure 4.2. The relative difference between experimental (f_1) and FEM simulated (f_2) resonance frequency ($\Delta f/f = (f_1 - f_2)/f_1 \times 100$) plotted against W/L of MCs.

In chapter 3, the experimental resonance frequency values of similar devices were compared with analytically estimated ones and it was found that the major correction factor comes from the effective length introduced at the fixed end, due to undercutting [21]. However, it is interesting to note that this effective length would be the same in all the devices, as the SiO₂ MCs used in the present work were batch fabricated on a single Si<100>/SiO₂ wafer pieces using bulk micromachining techniques. This implies that the nature of fixed end (clamping conditions) would be identical in all the devices. Similarly, the thickness variation of the MC across the width at various places, along the MC length was measured using a profiler (prior to release) and was found to be ± 5 nm. Such a variation in thickness would result in a frequency shift of 0.5% and therefore do not explain the observed frequency shift in figure 4.2.

Material properties, such as E and ρ values were taken from the literature and were kept constant throughout the simulations i.e. for all the lengths of MCs studied. Moreover,

it is well known that the thickness and material properties of all MCs fabricated over a single wafer piece are typically constant [22]. With these conditions, one would expect $(\Delta f/f)\%$ to be zero or a constant value for all MCs, i.e., it should be independent of MC length.

Resonance frequency measurements were performed in air and the vibrational characteristics of MCs are known to depend on the viscoelastic property of the fluid in which the beam is immersed, i.e. air in the present work [23]. To estimate the frequency shift due to the surrounding air, resonance frequency values were estimated using Sader's model [23] and compared with FEM simulated values which can be considered equivalent to measurements in vacuum. By considering the FEM simulated values as the frequency of MCs in vacuum (f_{vac}), one can estimate the frequency of MCs oscillating in fluid/air (f_{air}) using Sader's model, which is given by,

$$f_{air} = f_{vac} \left(1 + \frac{\pi \rho_f W}{4 \rho_c T} \Gamma_r(\omega) \right)^{-1/2} \quad (4.1)$$

where, ρ_f and ρ_c are the density of air and mass density of SiO₂ respectively, W and T are the width and thickness of the MC and $\Gamma_r(\omega)$ is the real part of the hydrodynamic function. By substituting the known values ($\rho_f = 1.18 \text{ kg/m}^3$, $\rho_c = 2650 \text{ kg/m}^3$, $W = 37 \text{ }\mu\text{m}$, $T = 0.98 \text{ }\mu\text{m}$ and $\Gamma_r(\omega)$ estimated from Reynold's number [23]), f_{air} was estimated. The computed shift in frequency with respect to FEM simulated values ($(\Delta f/f) = ((f_{air} - f_{vac})/ f_{air}) \times 100$) is shown in figure 4.3 with increasing W/L ratio of MCs. It is evident from this figure that the frequency shift is negative (mass addition) and decreases with increasing W/L ratio, which is in sharp contrast to figure 4.2 where we see a positive frequency shift (stiffness increase) and it increases with increasing W/L ratio. Moreover, the estimated maximum frequency shift ($\sim 0.2\%$) is much lower than the experimental observations ($\sim 5\%$) shown

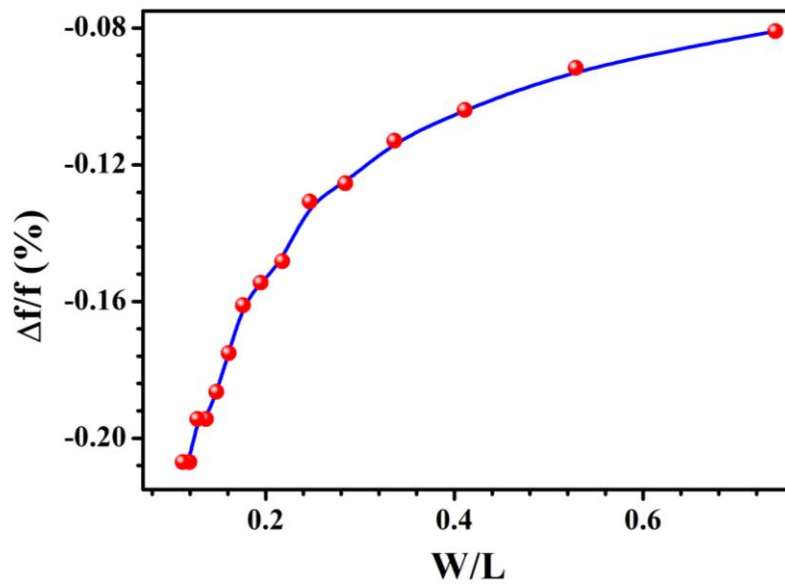


Figure 4.3. The relative shift in resonance frequency of MCs in air and vacuum (FEM) computed using Sader's model [23] as a function of W/L of MCs.

in figure 4.2. Therefore, one can conclude that the effect of the surrounding air does not explain the frequency shift observed in the present work. Therefore, we attribute the observed complex frequency shift in figure 4.2, to the *residual stress-induced biaxial curvature*, which was not included in FEM simulations.

4.1.3. Role of biaxial curvature on the resonance frequency of MCs

The biaxial curvature present in SiO₂ MCs was independently measured using a 3D OM on all the lengths of MCs fabricated. Figure 4.4 shows the variation of principal (K_x , along the length of MC) and transverse (K_y , along the width of MC) curvature values measured using a 3-D optical microscope, with W/L of MCs. From this figure, the following observations can be made.

K_x uniformly increases from 400 m⁻¹ to 600 m⁻¹ with increasing W/L. In contrast to this, K_y is initially low (~100 m⁻¹), increases rapidly to a value of 600 m⁻¹ with W/L, till 0.3 and thereafter the trend is similar to K_x , i.e., uniformly increases to a value of 800 m⁻¹. Similar W/L dependent increase in tip deflection and thus curvature was reported by several authors in bilayer MCs and attributed the same to the presence of *plain strain*

state [24,25]. For instance, Hou et al. [24], while studying the effect of width on the residual stress-induced out-of-plane deflection in bilayer MCs, found that the deflection increases with increasing width until the W/L reaches a critical value of 7. We now compare figures 4.2 and 4.4 to understand the role of biaxial curvature on the observed frequency shift by dividing them into three regions (shown by different shades in figure 4.2 and 4.4).

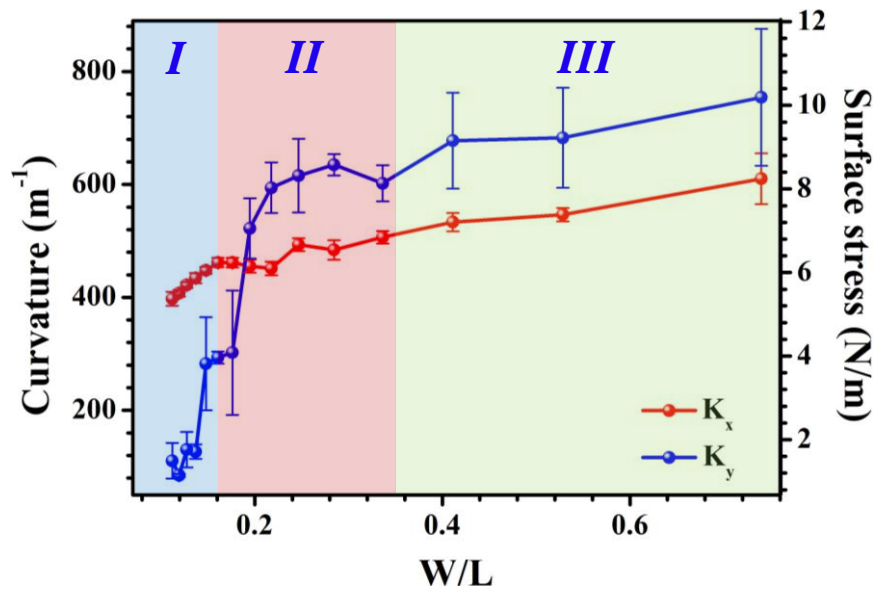


Figure 4.4. Variation of principal (K_x) and transverse (K_y) curvature values with the W/L ratio of MCs. Equivalent surface stress estimated using eq. 4.2 is shown on the right axis.

In region I, where $W/L < 0.16$, it is evident from figure 4.4 that K_x and K_y increase from 400 m^{-1} to 460 m^{-1} and $\sim 15 \text{ m}^{-1}$ to 300 m^{-1} , respectively. However, in this region, variation in $(\Delta f/f)$ is $< 1\%$ (figure 4.2) indicating that the influence of curvature on the resonance frequency is minimum. In this region, the *beam-like mechanism* ($W < L$, $T \ll L$) dominates where the curvature is known to have a negligible effect on the resonance frequency of the MCs, in accordance with the framework of linear elastic theory predicted by Gurtin et al [11]. In region II, where $0.16 < W/L < 0.35$, K_x and K_y increases from 420 m^{-1} to 500 m^{-1} and 300 m^{-1} to $\sim 620 \text{ m}^{-1}$, respectively. Interestingly, in this region,

$(\Delta f/f)$ was also found to increase from 1% to 5% and follows the trend similar to K_y . This is more clear from figure 4.5 (a) and (b), which shows the variation of $(\Delta f/f)$ with K_x and K_y , respectively. From this figure, it is clear that, unlike K_y , K_x does not show any clear dependence with $(\Delta f/f)$ in region-I and region-II indicating the predominant role of K_y on the observed frequency shift.

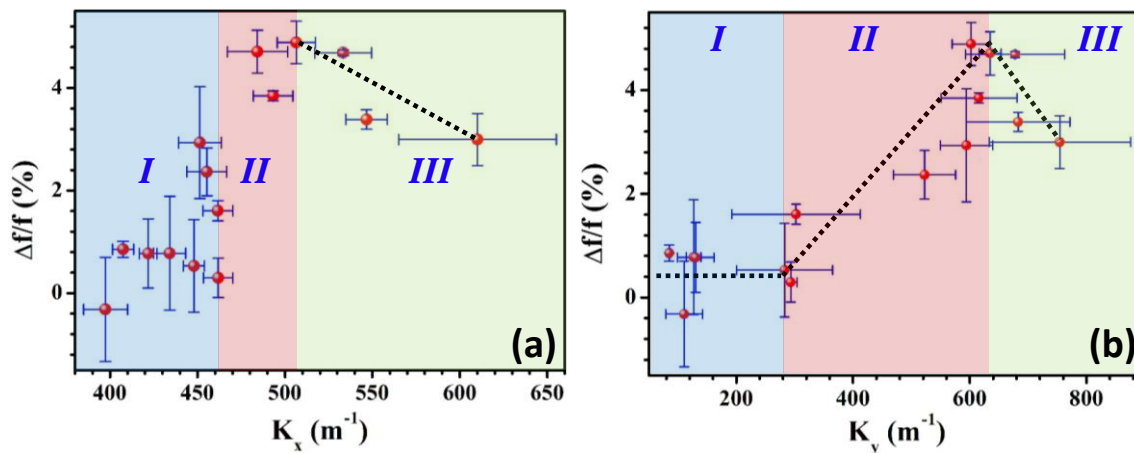


Figure 4.5. Variation of relative frequency shift with (a) longitudinal (K_x) and (b) transverse (K_y) curvature present in SiO_2 MCs. The dotted line is a guide to the eye. It is evident from (b) that in region-I, the frequency shift is independent of K_y whereas it linearly increases in region-II and reduces marginally in region-III.

In regions I and II, MC length becomes comparable to its width, leading to *non-linear plate stiffening* at the fixed end i.e., clamping effect. Clamping restriction exerts in-plane reaction forces to cancel out the bending moments introduced by K_y , which in turn increases the stiffness of MCs [18,19]. Also, the strain energy associated with the in-plane stretching is known to increase with increasing curvature (vis-à-vis W/L) [4]. With this argument, one would expect this effect to further increase with increasing W/L , i.e., in region III. However, in the region – III ($W/L > 0.4$), even though both K_x and K_y are increasing, $(\Delta f/f)$ was found to marginally reduce (see the negative slope in figure 4.5 (a) and (b)). This is attributed to the presence of a competing plate softening effect at these dimensions along with the *non-linear plate stiffening* effect. As W/L increases, non-linear

effects arise due to larger curvature values in this region. In this situation, the coupling between in-plane and out of plane strain is sufficiently high to give rise to an effective softening of MCs [17] leading to the reduction in $(\Delta f/f)$. These results clearly demonstrate that the gradient stress-induced biaxial curvature in SiO₂ MCs indeed increases the stiffness and this effect critically depends on MC dimensions. Also compared to K_x , K_y seem to have a dominant role on the observed frequency shift.

4.1.4. Comparison with previously reported experimental and theoretical studies

We now compare our results with various experimental studies reported in the literature on the curvature/surface stress induced frequency shift in MCs. Details about the MCs used, surface stress generation method and the observed frequency shift by various researchers along with our results are given in Table 4.1. It may be noted that in this table, curvature values were converted into surface stress values to maintain uniformity. From this table following observations can be made. 1) Most of the reported works are on bilayer MCs with W/L varying between 0.1 and 0.5 and for the generation of surface stress, no single method is adopted. 2) When $W/L < 0.2$, the observed frequency shift is zero or $\sim 1\%$ in most of the studies and is independent of the magnitude of surface stress. For example, Karabalin et al [10] reported a frequency shift of $\sim 1\%$ on their MCs with W/L of 0.15 for an applied surface stress of 5.75 N/m. For a similar W/L ratio, Sohi et al [4] reported a zero frequency shift for a much higher surface stress value of 10.1 N/m. This is similar to the observations made in the present work and is in accordance with the linear elastic theory that the effect of surface stress on the stiffness of MCs will be minimum, at these dimensions. 3) However, when $W/L > 0.2$, no such correlation exists across the studies. We have seen a frequency shift of $\sim 5\%$ for MCs with W/L between 0.16 and 0.35 for a maximum transverse surface stress of 8.7 N/m. Whereas for similar W/L and surface stress, Sohi et al [4] reported a frequency shift of only 0.25%, that too in the third mode.

Similar conclusions will be drawn by comparing the studies of Hwang et al [26]. These differences could be due to several reasons such as different methods adopted for generating surface stress, surface preparation methods followed by different groups, unspecified fabrication-induced curvature inherently present in MCs, etc. For example, in the case of gold-coated MCs, adhesion, surface morphology, and cleanliness of gold sensing surface is shown to have both qualitative and quantitative effects on the measured surface stress [27,28]. Similarly, in the case of uncoated MCs, surface morphology on opposite sides has a decisive role in the bending magnitude [20] and thus the generated surface stress. However, it is interesting to note that any potential experiment intending to relate the stiffness changes with surface stress needs physical/chemical modification of its surface and the associated artifacts are inevitable.

To understand the results better, we have compared our data with various available theoretical models relating the role of surface stress on the resonance frequency of MCs. For this purpose, the transverse curvature present in our devices was converted into an equivalent differential surface stress generated on their surface using Stoney's equation,

$$(\sigma_y) = \frac{ET^2}{6(1-\nu)}(K_y) \quad (4.2)$$

where, E , ν , and T are Young's modulus, Poisson's ratio of SiO₂, and thickness of MC, respectively.

Using the expression in Eq. (4.2), equivalent σ_y values were estimated and are shown on the right axis of figure 4.4. Table 4.2 shows various models considered in the present work along with the equations used for estimating the surface stress induced resonance frequency shift.

Table 4.1. Various experimental studies reported in the literature along with the present work for surface stress induced resonance frequency shifts.

| S.No. | Ref | MCs used and their physical dimensions | Surface stress ($\Delta\sigma_{max}$) generated | | Observed frequency shift ($\Delta f/f$)% in 1 st flexural mode |
|-------|-----------|---|---|---|---|
| | | | Mechanism | Value in (N/m) | |
| 1. | [7] | Gelatin coated V – shaped silicon MC - L =200 μm , k = 0.06 - 0.09 N/m | Moisture adsorption | 0.38 N/m | -1% |
| 2. | [8] | Si_3N_4 MC 193 x 20 x 0.6 μm^3 (W/L = 0.10) | Adsorption of Na ⁺ ions | 0.35 N/m | ~6% |
| 3. | [12] | Au/Ti/Si MC 499 x 97x 0.80 μm^3 (W/L = 0.19) | Amino ethane thiol adsorption | 0.59 mN/m | -0.2% to -0.9% |
| 4. | [26] | PZT MC functionalized with calix-crown SAM 150 x 50 x 2.18 μm^3 (W/L = 0.33) | Immobilization of antibodies | 2×10^{-2} N/m | ~-1% |
| 5. | [10] | AlN/Mo/AlN/Mo piezoelectric MCs L: 6 – 8 μm ; W:0.9 μm ; T: 0.32 μm (W/L = 0.11 – 0.15) | Surface stress in piezo layer due to applied electric field | 5.75 N/m | ~ 1% |
| 6. | [20] | Uncoated Si MC | Moisture adsorption | | |
| | | a. 450 x 40 x 2.5 μm^3 (W/L = 0.08) | | a. 0.02 N/m | a. Nil |
| | | b. 225 x 30 x 3 μm^3 (W/L = 0.13) | | b. 0.17 N/m | b. 0.05% |
| | | c. 125 x 35 x 4.5 μm^3 (W/L = 0.28) | | c. 0.35 N/m | c. 1% |
| 7. | [4] | Gold coated polysilicon MC | Thermal cycling induced curvature | | |
| | | a. 200 x 20 x (0.5+1.5) μm^3 (W/L =0.1) | | a. 10.1 N/m | a. Nil |
| | | b. 200 x 70 x (0.5+1.5) μm^3 (W/L = 0.35) | | b. 10.4 N/m | b. ~ 0.26%* |
| | | c. 200 x 100 x (0.5+1.5) μm^3 (W/L = 0.5) | | c. 10.6 N/m | c. ~ 0.65%* |
| 8. | [18] | Aluminium “macro” cantilever 29 x10 x 0.0645 cm^3 (W/L = 0.34) | Induced biaxial curvature | | |
| | | | a. K_x – Due to gravity | a. σ_x – value not specified | a.11% |
| | | | b. K_y - Manually pressing the cantilever plate | b. σ_y – 8.21 kN/m | b.90.9% |
| 9. | This work | Uncoated SiO_2 MC with varying (W/L) ratio between 0.11 and 0.74. | Fabrication induced biaxial curvature | $\Delta\sigma_x$ – 2.9 N/m $\Delta\sigma_y$ –8.7 N/m | <ul style="list-style-type: none"> • < 1% when W/L < 0.16 • ~5% when 0.16 < W/L < 0.35 • ~3% when W/L > 0.4 |

* The observed frequency shifts were in 3rd flexural resonance mode

By substituting the σ_y values along with other constants in these expressions, the relative frequency shift was estimated for all the MCs. We found that all these models either overestimated or underestimated the experimentally observed frequency shift by several orders. Similar large discrepancies between theoretical models and measurements are reported by several authors [4,15,16,29]. For example, Lachut and Sader [16] have compared their model with various experimental surface stress induced frequency shifts reported in the literature and concluded that their model under predicts the experimental observations by 3 orders. They opined that, “the observed changes in MC stiffness are due to the mechanism(s) unrelated to surface stress”. Karabalin et al [10] pointed out that such large discrepancies could be originating from other uncontrolled surface phenomena of MCs. Similar conclusions were drawn by Sohi et al [29], while comparing the curvature induced frequency shift with the models discussed above (see table 4 in ref [29]).

Taking a clue from this, it was decided to see whether the theoretical models at least capture the MC dimensional dependence observed in our experimental results. To do the same, the estimated frequency shift in each case was suitably scaled and is plotted against MC length along with our experimental data as shown in figure 4.6 (a). From this figure, it is clear that the Lagowski model predicts an increase in frequency shift with increasing MC length and does not follow the experimental data. This is because of the fact that the relaxation of the surface stress induced axial force at the free end of MCs is not taken into account in this model and is in direct violation of Newton’s third law.

Table 4.2. Various analytical models for estimating the surface stress induced resonance frequency shift. In this table, $\Delta f/f$ is the relative frequency shift, σ_y is the equivalent differential surface stress estimated from equation (2), ν and E are Poisson's ratio and Young's modulus of SiO_2 , respectively and L , W and T are the length, width and thickness of the MCs, respectively.

| S.No. | Model | Formula | Remarks |
|-------|-----------------------------------|---|--|
| 1. | Lagowski <i>et al</i> Model [6] | $\frac{\Delta f}{f} = 1.216 \left(\frac{(1-\nu)\sigma_y}{E} \right) \left(\frac{L^3}{WT^3} \right)$ | Axial force model - Failed to account for the relaxation of the applied force at the free end of MCs. Considered unphysical. |
| 2. | Lachut and Sader Model [14] | $\frac{\Delta f}{f} = -0.042 \frac{\nu(1-\nu)\sigma_y}{ET} \left(\frac{W}{L} \right) \left(\frac{W}{T} \right)^2$ | 3D model within the framework of linear elastic theory. Includes the unrelaxed in-plane stress at the immediate vicinity of the fixed-end. |
| 3. | Karabalin <i>et al</i> Model [10] | $\frac{\Delta f}{f} = \left[\frac{(1+2\nu)}{(1-\nu)} \right] \sigma_y$ | Extension to Lachut and Sader model. Considered the linear geometric effects. |
| 4. | Tamayo <i>et al</i> Model [17] | $\frac{\Delta f}{f} = 0.7 \left[\frac{(1-\nu)L\sigma_y}{ET^2} \right]^2$ | The shift in resonance frequency is always positive and is independent of the sign of differential surface stress. |

Whereas in the Lachut model, this discrepancy was removed and the non-uniform distribution of in-plane stress at the fixed end of the MCs was included and thus predicts an increasing frequency shift with reducing MC dimensions (see figure 4.6 (a)). However, this model does not explain the reduction in $(\Delta f/f)$ for MC length $<130 \mu\text{m}$. Similarly, Karabalin's model [10] which is an extension of Lachut's model, too does not predict the frequency shift at smaller lengths. In Tamayo's model, non-linear effects due to larger beam bending due to surface stress are considered and seem to predict a reduction in frequency shift at smaller lengths, but still, do not match completely with our experimental data.

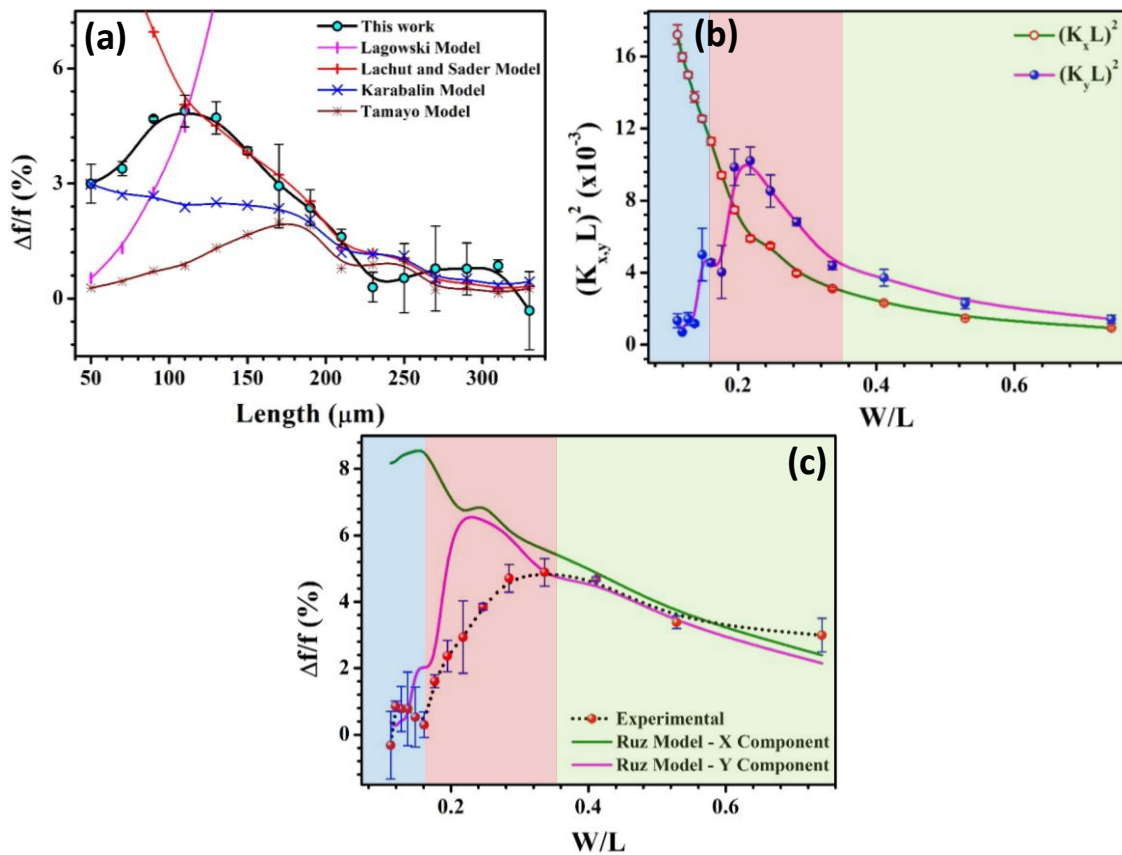


Figure. 4.6. (a) Comparison of the experimental frequency shift in the present work with various available theoretical models. Theoretical frequency shifts were suitably scaled to superimpose with our experimental data. (b) Square of dimensionless curvature $(K_{x,y}L)$ as a function of W/L . (c) Comparison of experimental frequency shift as a function of W/L along with Ruz et al [19] model for both x and y components of curvature.

In an effort to solve this long-standing problem, recently, Ruz et al [19] developed a theoretical framework to predict the effect of surface stress-induced curvature on stiffness and frequency of micro/nanocantilevers, by accounting for the biaxial curvature induced internal stresses, clamping restriction of bending moment and also the non-linear effects arising from large static deformations. From their detailed analytical and FEM simulation studies, they predicted the frequency shift due to surface stress-induced curvature as [19],

$$\frac{\Delta f_n}{f_n} = \left[\alpha_n + \frac{1}{120} \left(\frac{W^4 e^{-4c\frac{W}{L}}}{L^2 T^2} \right) \left(((1 - \nu^2) - 2\nu) + \lambda_n(\nu) \left(\frac{W^2 e^{-2c\frac{W}{L}}}{L^2} \right) \right) \right] (K_s L)^2 \quad (4.3)$$

where c and α_n are mode-dependent constant and coefficient which arises as a result of counterbalance between *non-linear stiffening* and *non-linear inertial* effects. For fundamental flexural mode, these constants are equal to 0.7745 and 0.02029, respectively. The function $\lambda_n(\nu)$ breaks the mode degeneration of *non-linear plate stiffening* coefficient and for fundamental flexural mode, $\lambda_n(\nu) = -0.33 + 8.82\nu - 29.31\nu^2$. All other constants in equation (4.3) has the same meaning as defined in the caption of Table 4.2. This model predicts that the relative shift in frequency is proportional to the square of dimensionless curvature ($K_s L$) accounting for *non-linear stiffening* and *clamping geometric* effect present in MCs ($e^{-4cW/L}$). Taking a clue from this, we have estimated the frequency shift using equation (4.3) by substituting the curvature values of our MCs along with other constants. We found that the above model underestimates the positive frequency shift by an order for the curvature present in our MCs. Therefore, it was decided to analyze the dimensional dependencies by scaling the estimated frequency shift. Initially, to understand the role of K_y and K_x on the resonance frequency shift, we have first estimated the dimensionless parameters $(K_y L)^2$ and $(K_x L)^2$ from equation 4.3, for our curvature values

and their variation with W/L is shown in figure 4.6 (b). From this figure, it is clear that $(K_x L)^2$ decreases exponentially with increasing W/L, whereas $(K_y L)^2$ initially increases, reaching a peak value at $W/L = 0.2$ and thereafter reduces, resembling the present experimental data. Now, by substituting $(K_y L)^2$ and $(K_x L)^2$ along with other constants in equation (4.2), we have estimated the resultant $(\Delta f/f)$ due to K_x and K_y , independently and superimposed on our experimental frequency data, as shown in figure 4.6 (c). From this figure, it is evident that K_y induced frequency shift is closer to the experimental data as compared to K_x . This indeed confirms the predominant role of K_y , as predicted in the present work, on the observed frequency shift in region II (figure 4.3).

From the foregoing discussion, we can conclude that biaxial curvature inherently present in SiO₂ MCs increases their stiffness and this effect critically depends on MC dimensions. We will now discuss the effect of high-temperature annealing on the static and dynamic properties of these devices.

4.2. Effect of high-temperature annealing on the bending properties of SiO₂ MCs

4.2.1. Introduction

SiO₂ MCs are generally exhibit upward bending, i.e., away from the wafer plane, when they are released from underlying Si by wet/dry chemical etching methods. This is attributed to the presence of compressive residual stress in the SiO₂ films which is mainly caused because of difference in thermal expansion coefficients between Si and SiO₂, resulting from the wafer being cooled from oxidation temperature to room temperature [1]. It is also well known that the uniaxial residual stress in a thin film has two main components namely, the mean and gradient residual stress components and that these components can be deduced from the out-of-plane deflection of MCs [1] (refer chapter 2

for more information). The presence of residual stress in MCs induces certain artifacts such as initial bending (in static mode) and stiffness changes (dynamic mode), when exploring them for sensing applications. Optimization of thin film growth parameters [30], post-deposition annealing [31], and laser heating of the released structures [32] are some of the methods reported in the literature to minimize the residual stress induced curvature. In the present work, the effect of post-release high-temperature annealing on the stress evaluation of SiO₂ MCs is studied.

For this purpose, four identical samples (wafer pieces) containing SiO₂ MCs were synthesized using DLW and wet chemical etching methods. These samples were annealed under different conditions as given in table 4.3. After the annealing process, samples were unloaded from the furnace and were carefully stored in a vacuum desiccator and were taken for characterization.

Table 4.3. Details of high-temperature annealing carried out on various samples.

| Sample Nomenclature | Annealing history | | | Annealing type |
|---------------------|-------------------|----------------|--------|------------------------|
| | Temperature | Atmosphere | Time | |
| S1 | 800°C | O ₂ | 1 hour | Post-release annealing |
| S2 | 1000°C | O ₂ | 1 hour | Post-release annealing |
| S3 | 1000°C | N ₂ | 1 hour | Post-release annealing |
| S4 | 800°C | O ₂ | 1 hour | Pre-release annealing |

4.2.2. Results and Discussion

4.2.2.1. Effect of annealing temperature

Figure 4.7 (a) shows the initial bending profiles across the length of the SiO₂ MCs (L = 90 μm), before and after annealing at 800°C (S1) and 1000°C (S2). It is evident from

this figure that the curvature and the corresponding peak bending magnitude (z_{\max}) increases with increasing annealing temperature. From these profiles, z_{\max} was extracted and found to be 2.57 μm , 7.71 μm , and 11.40 μm , respectively. However, no such significant increase in curvature was found in S4, which is pre-annealed i.e. prior to MC release at the same temperature (see figure 4.7 (b)). Therefore, the increase in curvature and z_{\max} values in post-release annealed sample is attributed to the onset of plastic deformation of the freestanding MCs when annealed at elevated temperatures [25,33]. It is well known that when the MCs are annealed at higher temperatures, they will expand and deform due to thermal stress. However, after a critical temperature, the accumulated stress crosses the elastic limit of the structural film (SiO_2) and the deformation becomes plastic leading to an irreversible increase in the curvature of the MCs, even after cooling. This also explains the increase in z_{\max} when annealing temperature was increased from 800°C to 1000°C. Similar plastic deformation in bi-material MCs during high temperature annealing was reported by several authors [25,34,35].

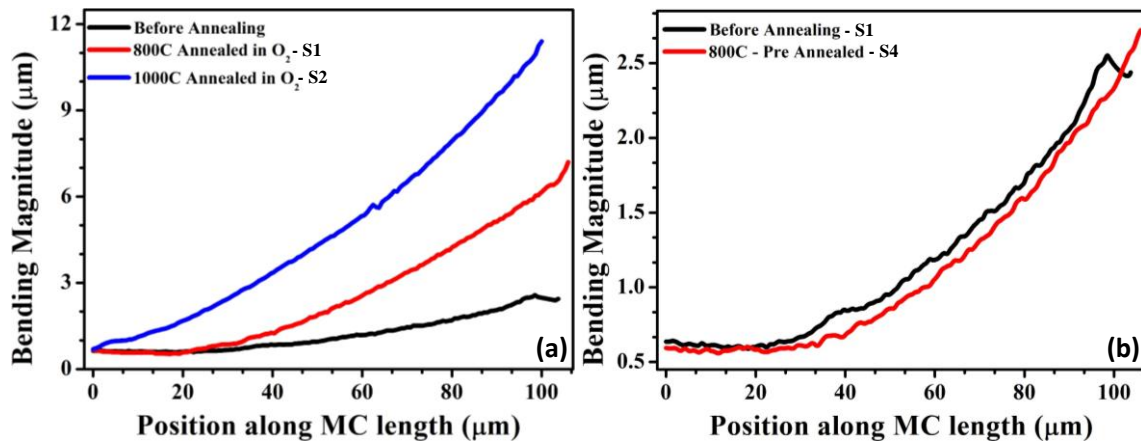


Figure 4.7. (a) Typical bending profiles of the MCs before and after annealing (at 800°C and 1000°C) in O_2 . (b) Typical line profiles of the MCs before and after pre-release annealing in O_2 at 800°C.

For example, while studying the effect of temperature on the curvature of Au/Si MCs, Gall et al., [34] found that the curvature of MCs either increase, decrease or remain

stable due to complex dependence of creep, recovery and microstructural coarsening, depending upon the annealing temperature and hold time. Kuo et al., [25] found that when high-temperature annealing is performed, the residual stress gets accumulated leading to plastic deformation of Au/ poly-Si MCs and that this effect critically depends on the annealing temperature and physical dimensions of the MCs. Similar conclusions were drawn by Lin et al., [35] while studying the thermomechanical behavior of alumina coated Au/SiN_x bilayer MCs. An increase in initial deflection due to high-temperature annealing was also reported in c-Si membranes [36].

4.2.2.2. Effect of annealing environment

In order to understand the role of annealing environment on the bending profile, S3 was annealed in N₂ at 1000°C, and the deflection profile along with S2 is shown in figure 4.8 (a). From this figure, it is evident that the curvature of the N₂ annealed sample is lower than that of the O₂ annealed sample. Also, the deflection profile at the fixed end of S2 is significantly different compared to that of S3. This is attributed to the stress accumulation resulting from the additional oxide layer growth at the SiO₂/Si interface below the fixed end of SiO₂ MCs, in O₂ environment at high temperature. However, more experiments are essential to validate the oxide growth at the fixed end of the MCs.

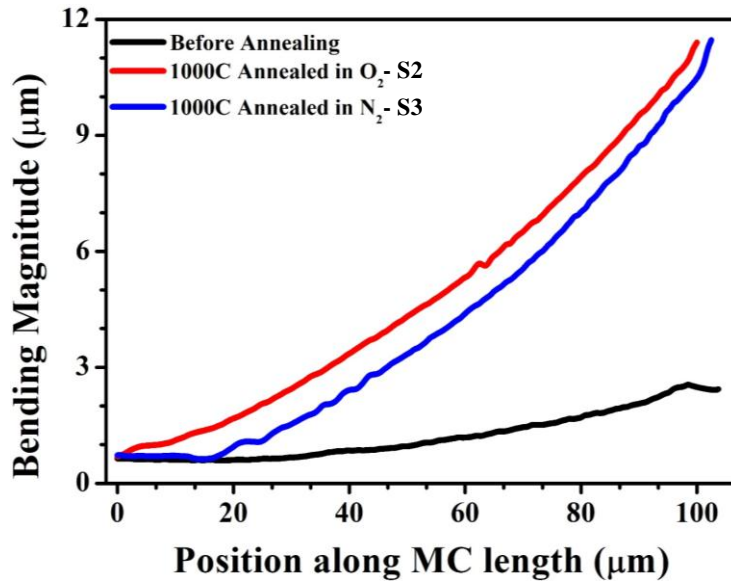


Figure 4.8. Typical line profiles of the MCs before and after annealing in O₂ and N₂ atmospheres at a constant temperature of 1000°C.

4.2.2.3. Effect of MC length

In order to understand the effect of MC length on the annealing induced plastic deformation, bending profiles of MCs of various lengths were recorded in each of the samples and the corresponding z_{\max} values were extracted. Figure 4.9 shows the variation of z_{\max} as a function of square of length (L^2) for S1 and S2 along with the data of MCs before annealing. Solid lines are linear fit of the experimental data and the extracted slope values are shown in Table 4.4. From this table, it is evident that with increasing annealing temperature slope increases which indicates the role of MC length on the bending.

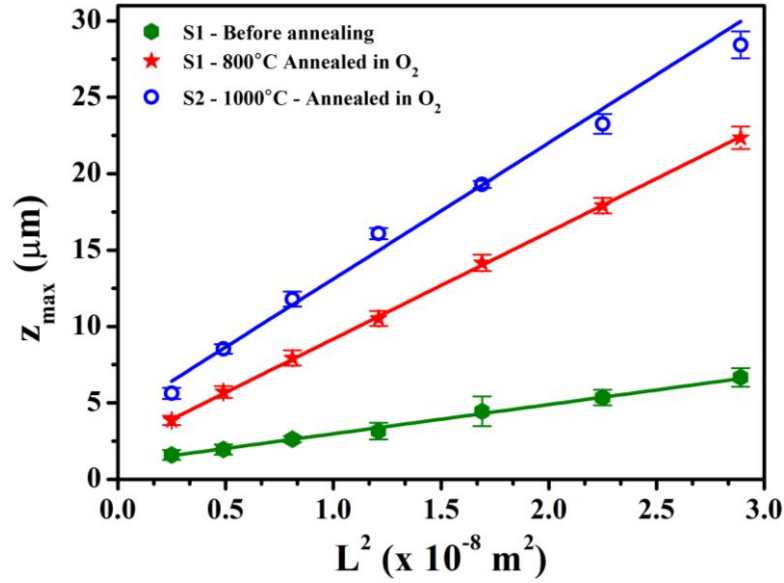


Figure 4.9. Peak deflection as a function of square of the length of the MCs before and after annealing at 800°C and 1000°C in O₂.

Table 4.4. The slope values extracted from z_{max} Vs. L^2 plot for the samples shown in table 4.3.

| Sample | Slope of z_{max} vs. L^2 (m^{-1}) |
|------------------|---|
| Before annealing | 191.31 ± 4.62 |
| S1 | 700.75 ± 5.41 |
| S2 | 891.71 ± 4.05 |

To understand these results better, the bending profiles of all the MCs were deconvoluted into mean (σ_0) and gradient (σ_1) residual stress values by the method described in chapter 2. The estimated σ_0 and σ_1 values for S1, before and after annealing at 800°C as a function of MC length are shown in figure 4.10 (a) and 4.10 (b), respectively. It is clear from these figures that σ_0 is negative whereas the σ_1 is positive, irrespective of the MC length, which would decide the nature of MC bending (in the present case it is upward bending) [1]. From figure 4.10 (a), it can be seen that prior to annealing, σ_0 remains nearly constant at 650 MPa. However, after annealing it is maximum for smallest MC,

decreases with increasing MC length till 90 μm and there after it remains constant. In the case of σ_1 , even though trend is similar to σ_0 , magnitude of increase in stress values after annealing at all the lengths is much higher. The enhanced stress levels at smaller lengths could be due to nature of clamping conditions.

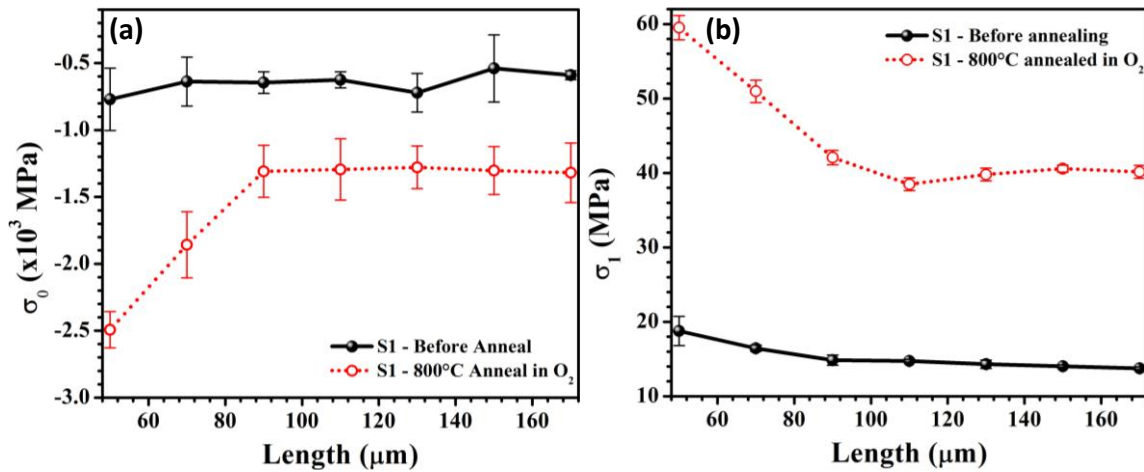


Figure 4.10. (a) Mean (σ_0) and (b) gradient (σ_1) residual stress values before and after 800°C annealing as a function of MC length. σ_0 , σ_1 values were estimated by fitting the corresponding line profiles of MCs to a second-order polynomial function.

4.2.2.4. Effect of annealing on the resonance frequency of MCs

In order to study the effect of annealing induced curvature on the resonance frequency of SiO₂ MCs, the resonance frequency of MCs was measured before and after annealing sample S1 using NVA. Figure 4.11 (a) shows the typical resonance spectrum of a 110 μm long MC before and after annealing. From this figure, it is evident that the resonance frequency increases from 63.05 kHz to 65.01 kHz and is attributed to the stress gradients induced by annealing and associated stiffness changes at the fixed end. The Q-factor was also estimated from the FWHM of the Lorentzian fit and it was found to increase by ~18% in all the MCs after annealing. This increase in Q-factor can be attributed to the surface smoothening of SiO₂ film with annealing leading to a reduction in surface losses. Similar measurements were repeated for MCs of all lengths and the relative shift

in resonance frequencies of the MCs before and after annealing were estimated and plotted as a function of MC length as shown in figure 4.11 (b). The relative resonance frequency shift between experimental and FEM simulated frequency values from figure 4.6 is also shown in this figure, for comparison. It may be noted, in longer MCs ($> 190 \mu\text{m}$) resonance frequency measurements could not be performed because of the presence of large curvature. From this figure, it is evident that the magnitude of the frequency shift is higher after annealing. However, frequency shift follows a similar trend with increasing MC length, validating our hypothesis of biaxial curvature induced frequency shift.

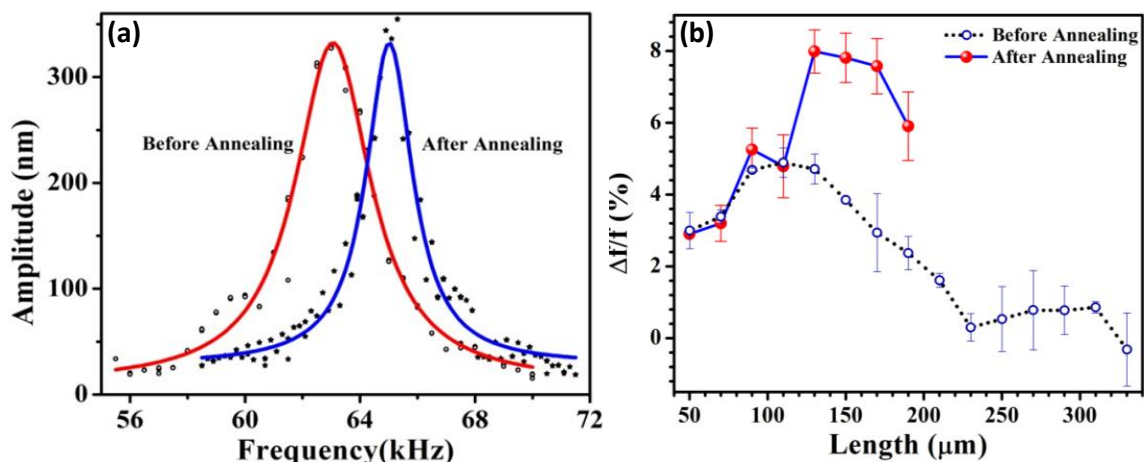


Figure 4.11. (a) Resonance spectrum of a typical 110 μm long MC before and after annealing along with Lorentzian fit. (b) Relative difference in resonance frequencies of MCs before and after annealing ($\Delta f/f$ %) plotted as a function of MC length.

From the foregoing discussion, we can conclude that even single layer MCs undergo an irreversible increase in deflection (plastic deformation) with high-temperature annealing and this effect is more when the annealing environment is O_2 . The resonance frequency of the MCs increases with annealing and the shift critically depends on the MC length, validating our hypothesis.

4.3. Summary

In summary, we have investigated the effect of biaxial curvature on the resonance frequency and the effect of high-temperature annealing on the residual stress evolution of as-fabricated MCs. The major conclusions from this chapter are summarized below.

a) Effect of biaxial curvature on the resonance frequency

Through systematic experiments, it is demonstrated that the presence of transverse curvature in uncoated MCs directly increases their stiffness when their W/L is between 0.16 and 0.35. Nonlinear stiffening and clamping geometric effect present in MCs indeed is the reason for the observed positive frequency shift in this region, and compared to K_x , K_y seems to play a dominant role on the observed frequency shift. Also, for the first time, it is shown that the competing plate softening effect due to the presence of unrelaxed transverse curvature along with the nonlinear plate stiffening effect as the reason for the decrease in frequency shift for MCs with $W/L > 0.35$, validating Ruz et al. model [19]. Comparison of various experimental studies and analytical models reported in the literature on the role of surface stress/ curvature on the resonance frequency of MCs revealed the following.

- ❖ When W/L of MCs is < 0.2 , the observed frequency shift is $< 1\%$ and is independent of the magnitude of surface stress. Whereas, when W/L ratio > 0.2 , no correlation exists between these two parameters.
- ❖ Most of the reported analytical models only predict the dimensional dependence and not the absolute value of the measured frequency shift.

This discrepancy is believed to be due to the presence of unspecified effects such as fabrication induced curvature and surface morphology of MCs and no single method being adopted for the generation of surface stress.

b) Annealing studies

It is shown that post-release high-temperature annealing of SiO₂ MCs increases their curvature and is attributed to the onset of plastic deformation of these structures at elevated temperatures. The mean and gradient residual stress for all the MCs were also deduced from the bending profiles of the MCs before and after annealing. They were found to increase by ~230% in smaller MCs. The curvature of MCs annealed in O₂ was higher than the samples annealed in N₂. This is attributed to the stress accumulation resulting from the additional oxide layer growth at the SiO₂/Si interface below the fixed end of SiO₂ MCs, in the former. The resonance frequency of the MCs increases with annealing and it depends on the MC length validating our hypothesis of biaxial curvature induced frequency shift.

4.4. References

- [1] W. Fang, J.A. Wickert, Determining mean and gradient residual stresses in thin films using micromachined cantilevers, *J. Micromechanics Microengineering*. 6 (1996) 301–309.
- [2] Z. Schumacher, Y. Miyahara, L. Aeschimann, P. Grütter, Improved atomic force microscopy cantilever performance by partial reflective coating, *Beilstein J. Nanotechnol.* 6 (2015) 1450–1456.
- [3] A. Boisen, T. Thundat, Design & fabrication of cantilever array biosensors, *Mater. Today*. 12 (2009) 32–38.
- [4] A.N. Sohi, P.M. Nieva, Frequency response of curved bilayer microcantilevers with applications to surface stress measurement, *J. Appl. Phys.* 119 (2016).

- [5] J. Tamayo, D. Ramos, J. Mertens, M. Calleja, Effect of the adsorbate stiffness on the resonance response of microcantilever sensors, *Appl. Phys. Lett.* 89 (2006) 2004–2007.
- [6] J. Lagowski, H.C. Gatos, E.S. Sproles, Surface stress and the normal mode of vibration of thin crystals: GaAs, *Appl. Phys. Lett.* 26 (1975) 493–495.
- [7] G.Y. Chen, T. Thundat, E.A. Wachter, R.J. Warmack, Adsorption-induced surface stress and its effects on resonance frequency of microcantilevers, *J. Appl. Phys.* 77 (1995) 3618–3622.
- [8] S. Cherian, T. Thundat, Determination of adsorption-induced variation in the spring constant of a microcantilever, *Appl. Phys. Lett.* 80 (2002) 2219–2221.
- [9] J. Tamayo, V. Pini, P. Kosaka, N.F. Martinez, O. Ahumada, M. Calleja, Imaging the surface stress and vibration modes of a microcantilever by laser beam deflection microscopy, *Nanotechnology.* 23 (2012).
- [10] R.B. Karabalin, L.G. Villanueva, M.H. Matheny, J.E. Sader, M.L. Roukes, Stress-induced variations in the stiffness of micro- and nanocantilever beams, *Phys. Rev. Lett.* 108 (2012) 1–5.
- [11] M.E. Gurtin, X. Markenscoff, R.N. Thurston, Effect of surface stress on the natural frequency of thin crystals, *Appl. Phys. Lett.* 29 (1976) 529–530.
- [12] A.W. McFarland, M.A. Poggi, M.J. Doyle, L.A. Bottomley, J.S. Colton, Influence of surface stress on the resonance behavior of microcantilevers, *Appl. Phys. Lett.* 87 (2005) 1–4.
- [13] P. Lu, H.P. Lee, C. Lu, S.J. O’Shea, Surface stress effects on the resonance properties of cantilever sensors, *Phys. Rev. B - Condens. Matter Mater. Phys.* 72 (2005) 1–5.

- [14] M.J. Lachut, J.E. Sader, Effect of surface stress on the stiffness of cantilever plates, *Phys. Rev. Lett.* 99 (2007) 1–4.
- [15] M.J. Lachut, J.E. Sader, Effect of surface stress on the stiffness of cantilever plates: Influence of cantilever geometry, *Appl. Phys. Lett.* 95 (2009).
- [16] M.J. Lachut, J.E. Sader, Effect of surface stress on the stiffness of thin elastic plates and beams, *Phys. Rev. B - Condens. Matter Mater. Phys.* 85 (2012) 1–11.
- [17] J. Tamayo, P.M. Kosaka, J.J. Ruz, Á. San Paulo, M. Calleja, Biosensors based on nanomechanical systems, *Chem. Soc. Rev.* 42 (2013) 1287–1311.
- [18] V. Pini, J.J. Ruz, P.M. Kosaka, O. Malvar, M. Calleja, J. Tamayo, How two-dimensional bending can extraordinarily stiffen thin sheets, *Sci. Rep.* 6 (2016) 1–6.
- [19] J.J. Ruz, V. Pini, O. Malvar, P.M. Kosaka, M. Calleja, J. Tamayo, Effect of surface stress induced curvature on the eigenfrequencies of microcantilever plates, *AIP Adv.* 8 (2018) 105213.
- [20] K. Lakshmoji, K. Prabakar, S. Tripura Sundari, J. Jayapandian, C.S. Sundar, Effect of surface stress on microcantilever resonance frequency during water adsorption: Influence of microcantilever dimensions, *Ultramicroscopy.* 146 (2014) 79–82.
- [21] S. Balasubramanian, K. Prabakar, Fabrication and characterization of SiO₂ microcantilevers by direct laser writing and wet chemical etching methods for relative humidity sensing, *Microelectron. Eng.* 212 (2019) 61–69.
- [22] J.E. Sader, I. Larson, P. Mulvaney, L.R. White, Method for the calibration of atomic force microscope cantilevers, *Rev. Sci. Instrum.* 66 (1995) 3789–3798.
- [23] J.E. Sader, Frequency response of cantilever beams immersed in viscous fluids with applications to the atomic force microscope, *J. Appl. Phys.* 84 (1998) 64–76.

- [24] M.T.K. Hou, R. Chen, Effect of width on the stress-induced bending of micromachined bilayer cantilevers, *J. Micromechanics Microengineering*. 13 (2003) 141–148.
- [25] Ju-Nan Kuo, Gwo-Bin Lee, Wen-Fung Pan, Stress-Induced Bending of Micromachined Bilayer Cantilever and Its Optical Application, (2005) 290–295.
- [26] K.S. Hwang, K. Eom, J.H. Lee, D.W. Chun, B.H. Cha, D.S. Yoon, T.S. Kim, J.H. Park, Dominant surface stress driven by biomolecular interactions in the dynamical response of nanomechanical microcantilevers, *Appl. Phys. Lett.* 89 (2006) 173905.
- [27] H.F. Ji, B.D. Armon, Approaches to increasing surface stress for improving signal-to-noise ratio of microcantilever sensors, *Anal. Chem.* 82 (2010) 1634–1642.
- [28] J. Mertens, M. Calleja, D. Ramos, A. Tarín, J. Tamayo, Role of the gold film nanostructure on the nanomechanical response of microcantilever sensors, *J. Appl. Phys.* 101 (2007).
- [29] A. Najafi Sohi, P.M. Nieva, Size-dependent effects of surface stress on resonance behavior of microcantilever-based sensors, *Sensors Actuators, A Phys.* 269 (2018) 505–514.
- [30] M. Kumar, A.K. Sigdel, T. Gennett, J.J. Berry, J.D. Perkins, D.S. Ginley, C.E. Packard, Optimizing amorphous indium zinc oxide film growth for low residual stress and high electrical conductivity, *Appl. Surf. Sci.* 283 (2013) 65–73.
- [31] X. Zhang, T.Y. Zhang, M. Wong, Y. Zohar, Residual-stress relaxation in polysilicon thin films by high-temperature rapid thermal annealing, *Sensors Actuators, A Phys.* 64 (1998) 109–115.

- [32] X.R. Zhang, X. Xu, Laser bending for high-precision curvature adjustment of microcantilevers, *Appl. Phys. Lett.* 86 (2005) 6–9.
- [33] D.E.J. Armstrong, E. Tarleton, Bend Testing of Silicon Microcantilevers from 21°C to 770°C, *Jom.* 67 (2015) 2914–2920.
- [34] K. Gall, N. West, K. Spark, M.L. Dunn, D.S. Finch, Creep of thin film Au on bimaterial Au/Si microcantilevers, *Acta Mater.* 52 (2004) 2133–2146.
- [35] I.K. Lin, X. Zhang, Y. Zhang, Inelastic deformation of bilayer microcantilevers with nanoscale coating, *Sensors Actuators, A Phys.* 168 (2011) 1–9.
- [36] J. Ren, P. Kinnell, M. Gear, M. Ward, R. Craddock, The creep behaviour of the microfabricated silicon diaphragms at 900 °C, *Microelectron. Eng.* 87 (2010) 1213–1216.

Chapter 5

Relative humidity sensing studies using SiO₂ microcantilevers

This chapter presents RH sensing studies on as fabricated and micro-patterned SiO₂ MCs. RH sensing experiments were performed by measuring the shift in resonance frequency of MCs using NVA while RH is varied between 20% and 90%. Experiments on as-fabricated SiO₂ MCs revealed that these devices can be effectively used as RH sensors in dynamic mode, without any functionalization, with maximum sensitivity and resolution of 4 Hz/%RH and < 1% RH, respectively. RH sensitivity of micro-patterned MCs was found to be significantly higher than the unpatterned ones, especially at higher RH values. With the help of a model, it is shown that the formation of gel-like water layer inside the micro-patterns which facilitates the enhanced uptake of water molecules, is the reason for the higher sensitivity. Micro-patterned MCs exhibited an unprecedented RH sensitivity (10.45 Hz/% RH), ultrafast response/recovery times (~ 1 s) and outstanding stability (variation <5%) along with low hysteresis error (<3 %RH). Finally, real-time monitoring of human respiration during normal and slow inhale/exhale breathing cycles is demonstrated using these sensors.

5.1. Introduction

Humidity is one of the commonly measured physical quantity, which gives the measure of water vapor present in the air [1]. In general, there are two parameters associated with humidity measurement, namely, Absolute Humidity (AH) and Relative Humidity (RH) [2]. AH is defined as the mass of water vapor present in a unit volume of

air and is often expressed as gram of water vapor per cubic meter of air (g/m^3). Whereas RH is defined as the ratio of the partial pressure of water vapor (P_p) to the saturation vapor pressure of the air (P_s) at a given temperature is generally expressed as [3],

$$RH = \frac{P_p}{P_s} \times 100\% \quad (5.1)$$

As the definition suggests RH is dependent on both temperature and pressure and is generally expressed as percentage. Implementation of RH sensing is much simpler when compared to AH sensing. Sustained real-time monitoring and active control of RH are of paramount importance in the semiconductor fabrication industry, atmospheric chemistry, breath monitoring, climatology, agriculture, food storage, and medical industries [4–7]. To suffice this broad range of applications, it is therefore, necessary to develop state-of-the-art RH sensors with high sensitivity, fast response/recovery times (time required for the sensor to reach 90% of the final value from 10% of its start value and vice-versa) and ease of integration with readout electronics. Typically, RH sensors are fabricated by integrating a moisture-absorbing/adsorbing material with a suitable transduction method which converts the RH change into an electrical signal.

Several RH sensing materials such as ceramics (Al_2O_3 , TiO_2 , ZnO , SiO_2 , LiCl) [2,8], polymers (polyvinyl alcohol, polypropylene, polyimide, PMMA, SU-8) [9–11], semiconducting materials (SnO_2 , BaMO_3 , In_2O_3) [12–14] and composites (ex. Vinyl functionalized mesoporous silica modified with sodium p-styrenesulfonate) [15,16] are extensively studied, in recent times. Various transduction mechanisms are also explored in the literature for measuring RH which include resistive [17,18], capacitive (electrical) [19–21], refractive index change (optical) [22], frequency shift (gravimetric) [23,24], piezoresistive [10,25] and magnetoelastic frequency shift [26]. Despite the diversity of sensing materials and mechanisms, most of the conventional RH sensors still

lack in their sensing performance and require substantial improvements to be qualified for real-time field applications. For example, resistive and capacitive RH sensors, in spite of their ease of fabrication, suffer from slower response/recovery times, short-term stability, and requirement of complex readout circuits for precision applications [10].

In recent times, gravimetric sensors like Quartz Crystal Microbalance (QCM) [[27]], Surface Acoustic Wave (SAW) devices [28], microbridges [29] and MCs [9,25,30] have gained much attention for RH sensing, owing to their superior characteristics. In these sensors, adsorption/desorption of water molecules on the sensor surface, during RH change, typically results in resonance frequency shift and is usually measured by optical or piezoresistive methods. It may be noted, measuring the resonance frequency shift with high precision is relatively easier when compared to accurate voltage/current measurements [25]. Among the gravimetric sensors, MCs are popular due to their unprecedented sensitivity and miniaturized size. MCs are usually coated with a moisture-sensitive layer such as metal oxides, organic polymers, or hybrid composite materials, whose purpose is to selectively adsorb the water molecules [24]. Subsequently, the adsorption of water molecules on the MC surface increases the effective mass and results in a resonance frequency shift.

Interestingly, SiO₂ MCs can be used for RH sensing [31] without any functionalization because of the presence of the hydroxyl groups on their surface which facilitates the water molecule adsorption through hydrogen bonding [32]. The greatest advantage of these sensors is that these are compatible with the current microelectronics industry and can easily be integrated with readout electronics. However, the RH sensitivity of as-fabricated SiO₂ MCs is low when compared to conventional sensors. To increase the RH sensitivity, as mentioned above, MCs are usually coated with moisture sensitive

materials. In recent times, nano structured materials are considered for this purpose, which further increases the effective surface area and thus the number of adsorption sites available for water molecules. Several orders of increase in RH sensitivity is reported while using nanomaterials. But, functionalizing MCs with nanomaterials is known to deteriorate other sensor characteristics such as response/recovery times. For example, S. Stassi et al. [33] showed that the RH sensitivity of Si MC can be enhanced by two orders by coating a mesoporous silica thin film on its surface. However, they reported a huge hysteresis error ($\sim 35\%$ RH) for their coated sensors and attributed the same to complex nanopore organization leading to condensation of water layers. J. Xu et al. [34] studied the humidity sensing performance of ZnO nano-rods coated piezoresistive Si MCs and reported a RH sensitivity of $4.4\text{ ppm}/\%RH$ along with a low hysteresis error of 2.1% . They also showed that when ZnO nano-rods are modified with chitosan self-assembled monolayers, the RH sensitivity of these sensors can be further enhanced to $16.9\text{ ppm}/\%RH$. However, compared to ZnO planar film coated MCs, the response and recovery times of ZnO nano-rods coated MCs were found to be much longer [25]. Similarly, X. Le et al. [35] proposed an interdigital transducer (IDT) actuated AlN MC with graphene oxide (GO) coating for humidity sensing and demonstrated a RH sensitivity of $84\text{ Hz}/\%RH$. They also pointed out that RH sensitivity can be further enhanced by increasing the thickness of GO film however at the cost of slower response and recovery times. As an alternative to this, in the present thesis, it is shown that the introduction of controlled micro-patterns on the MC surface will enhance the RH sensitivity without compromising other crucial characteristics.

The rest of the chapter is organized as follows. Firstly, RH sensing experiments on as fabricated MCs is presented. Followed by this RH sensing studies on micro-patterned

MCs is discussed in detail. Finally, real-time monitoring of human respiration during fast and slow cycles using micro-patterned MCs is demonstrated.

5.2. RH sensing using as-fabricated SiO₂ MCs

5.2.1. Sensitivity, Resolution and Hysteresis

Initially, RH sensing experiments on as fabricated SiO₂ MCs were performed by measuring the shift in resonance frequency while RH is varied between 44% and 58%. Figure 5.1 (a) shows the resonance frequency shift in a typical SiO₂ MC (L = 210 μm) as a function of time during one RH increase and decrease cycle. From this figure, it is clear that during the RH increase (decrease) cycle, the resonance frequency of MC is reducing (increasing) indicating mass loading (unloading) due to physisorption (desorption) of water molecules on its surface. These results are clearer from figure 5.1 (b), which shows the relative shift in the resonance frequency of MC as a function of RH. From this figure, the RH sensitivity (S) was estimated using the equation,

$$S = \frac{f_i - f_f}{RH_i - RH_f} \text{ (Hz/%RH)} \quad (5.2)$$

where, f_i and f_f , and RH_i and RH_f are initial and final resonance frequency values of the MCs and corresponding RH values, respectively. Using this equation, a maximum RH sensitivity of 4.08 Hz/%RH was estimated between 54% and 58% RH. Also, from figure 5.1 (b) the resolution (smallest change in RH that can be detected by the sensor) of the sensor was estimated and found to be < 1%. This demonstrates that these SiO₂ MCs can be effectively used as humidity sensors with good sensitivity and resolution, without any functionalization. This is attributed to the presence of silanol (–Si–OH) groups on the SiO₂ surface, which directly facilitates the adsorption of water molecules through hydrogen bonding [32]. Between the RH levels studied in the present work (~ 40% to 60%), adsorption also takes place in multilayers by forming stacks on top of the silanol groups

through hydrogen bonding and Van der Waals interactions ($\text{H}_2\text{O} - \text{H}_2\text{O}$ interactions) [36].

This process increases the mass loading on SiO_2 MC, leading to a negative resonance frequency shift, as seen in figure 5.1 (a).

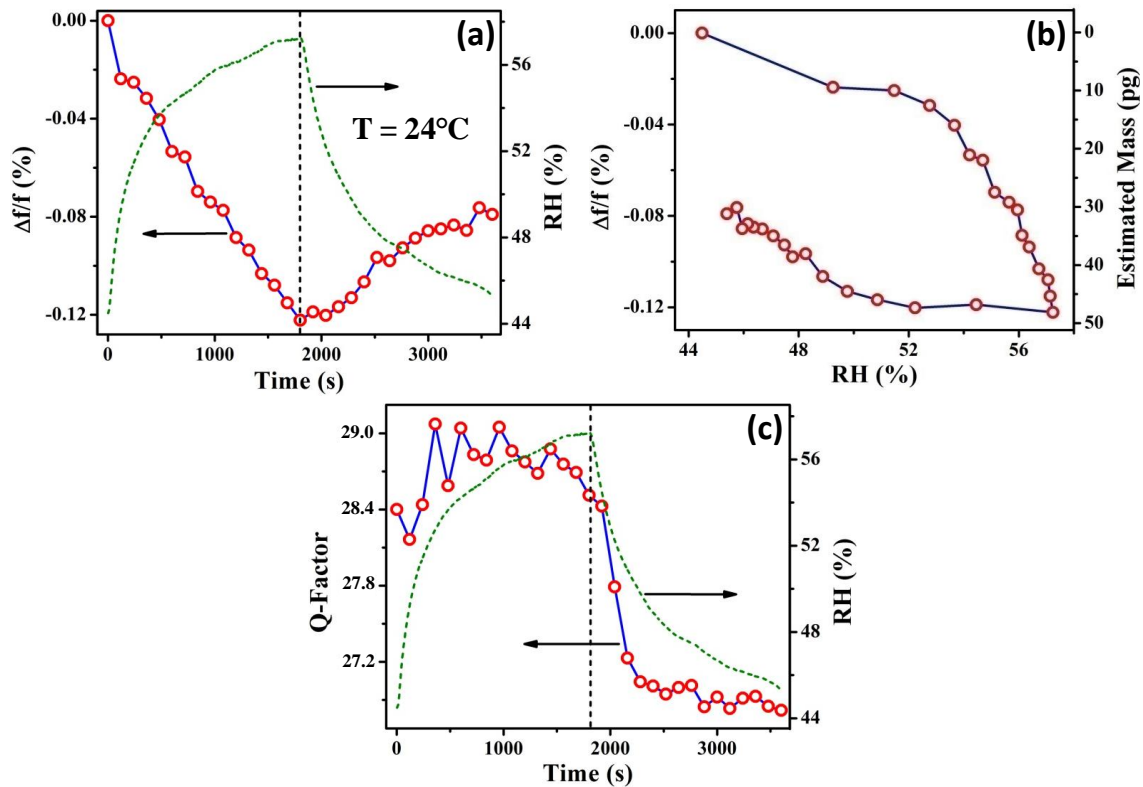


Figure 5.1. (a) Relative resonance frequency shift ($(\Delta f/f)\%$) in a typical SiO_2 MC ($210 \times 37 \times 0.98 \mu\text{m}^3$) and (c) estimated Q-factor as a function of time during one RH increase and decrease cycle between 44% to 58%. The green dotted line shows the variation in RH inside the chamber as a function of time, measured independently, keeping the temperature constant at 24°C . (b) The relative shift in the resonance frequency of MC as a function of RH. From the shift in frequency, the adsorbed/desorbed mass is estimated using equation 5.3 and is shown on the right axis.

These results can be further understood by estimating the added mass on the MC surface during adsorption. From the observed frequency shift (f_2) with increasing (reducing) RH values, with respect to its value at 44% RH (f_1), the adsorbed (desorbed mass) (Δm) can be estimated using the Eq. (1.21). The adsorbed (desorbed) mass was

estimated at each RH value, and total adsorbed (desorbed) mass was found to be ~ 50 pg (15 pg) (see figure 5.1 (b) right axis).

One can also estimate the adsorbed mass analytically from the number of monolayers adsorbed on the SiO₂ MC surface between the RH levels studied. The number of monolayers on SiO₂ surface between the RH levels of interest was taken from the work of Asay and Kim [36] and found to be ~ 1 monolayer. The mass of a single monolayer adsorbed uniformly on MC can be calculated using [38],

$$M_{ML} = \left(\frac{M_{H_2O}}{N_A} \rho_{H_2O}^2 \right)^{\frac{1}{3}} \cdot A_{MC} \quad (5.3)$$

where, M_{H_2O} and, ρ_{H_2O} are the molecular mass (18 g/mol) and density (1 g/cm³) of water, respectively, N_A is the Avogadro's number ($6.023 \times 10^{23} \text{ mol}^{-1}$) and A_{MC} is the MC surface area. The MC used in the present work had a total surface area of $1.62 \times 10^{-4} \text{ cm}^2$, implying a monolayer of water film on both sides of MC will weigh ~ 5 pg, which is one order lower than the experimentally obtained value. This difference is attributed to the presence of surface features on SiO₂, which increases the effective surface area and thus the number of adsorption sites [39,40].

Figure 5.1 (c) shows the variation of Q-factor value estimated from the resonance spectrum at every RH value, as a function of time along with the varied RH values on the right axis. From this figure, it is clear that Q-factor remains constant at ~ 29 during the RH increase cycle, whereas it marginally reduces to ~ 27 when RH is decreasing, which further indicates the role of complex nano features on the surface on the desorption [41].

Hysteresis characteristic (H) is an important parameter for evaluating the accuracy and efficiency of a RH sensor. It is a measure of the degree of uncertainty of a sensor and is given by [42],

$$H = \frac{\text{Max}|f_{ads} - f_{des}|}{S} \times 100 (\%RH) \quad (5.4)$$

where f_{ads} and f_{des} stand for the resonance frequencies of the MCs during adsorption and desorption cycles and S stands for the RH sensitivity of the MC in the given RH range. Using this equation, the maximum hysteresis was estimated and found to be 9 %RH, between 54% and 58% RH. The existence of hysteresis in these systems is known and is attributed to the complex nano features present on the MC surface which could hinder the desorption process. To verify the same, AFM measurements were performed on these SiO₂ MC surfaces which revealed the RMS roughness to be ~4.7 nm. This is evident from figure 5.1 (b) that during RH decrease cycle, frequency shift remains constant till ~50% RH, and thereafter it reduces, indicating that MC retains the adsorbed water molecules till this period, due to the presence of nano features on MC surface [41]. Further, from figure 5.1 (a) and (b), the response time of the sensor was estimated to be ~ 60 s.

From the foregoing discussions, it is clear that SiO₂ MCs can be effectively used for RH sensing without any functionalization. To enhance the sensitivity of these sensors, controlled micro-patterns are introduced on their surface and is discussed in detail in the following section.

5.3. RH sensing experiments using micro-patterned SiO₂ MCs

Details about the fabrication and characterization of micro-patterned MCs are discussed in chapter 3, section 3.3. It may be noted, for these experiments, SiO₂/Si wafers with RMS roughness < 2 nm were used and it was decided to perform RH sensing measurements on 15 nm deep surface micro-patterned MCs. Figure 5.2 shows the standard deviation in the resonance frequency values of unpatterned and micro-patterned MCs, independently measured on 15 different devices. From the figure, it is clear that the presence of micro-patterns only marginally reduces the resonance frequency of SiO₂ MCs.

It may be noted, both unpatterned and micro-patterned MCs were batch fabricated on a single wafer piece. This ensures that except for the presence of micro-patterns on 50% of the devices, all other parameters such as physical dimensions, clamping conditions and the material properties, such as Young's Modulus and mass density of all the tested devices remain same. Also, RH sensing experiments in both the cases were performed under identical experimental conditions. Therefore, as a first-order approximation, any comparison between unpatterned and patterned MCs can be attributed to the presence of micro-patterns.

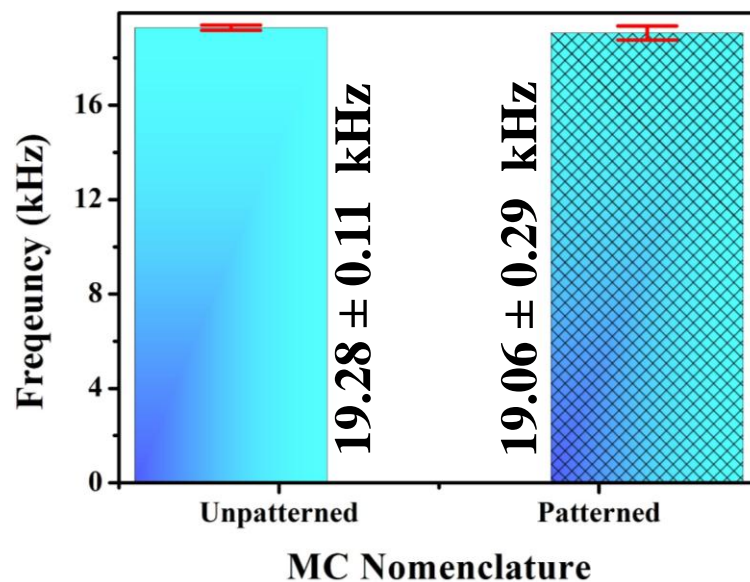


Figure 5.2. The statistical data of resonance frequency values independently measured on unpatterned and 15 nm deep micro-patterned MCs.

5.3.1. Sensitivity

The RH sensing experiments were performed on unpatterned and micro-patterned ($4 \times 4 \times 0.015 \mu\text{m}^3$) MCs ($210 \times 37 \times 0.98 \mu\text{m}^3$) sequentially by measuring the resonance frequency using NVA (see Chapter 2). Fig. 5.3 (a) shows the relative resonance frequency shift ($\Delta f/f$)% in a typical micro-patterned and unpatterned MC when the RH is increased from 20% to 90%. From this figure following observations can be made:

1) The resonance frequency of both micro-patterned and unpatterned MC reduces with increasing RH, indicating the physisorption of water molecules on their surface. As explained earlier, this is attributed to the presence of silanol ($-\text{Si}-\text{OH}$) groups on the SiO_2 surface, which directly facilitates the adsorption of water molecules through hydrogen bonding [32]. Moreover, from the observed frequency shift, one can estimate the added mass on the MC surface, using Eq. (1.21). Using this equation the adsorbed mass at each RH level was estimated and is shown on the right axis of Fig. 5.3 (a).

2) The maximum relative shift in resonance frequency for the micro-patterned MC (2.1%) is more than two times as compared to unpatterned MC (0.95%) which corresponds to a total adsorbed mass of 856 pg and 357 pg in these MCs, respectively. However, the responses of both micro-patterned and unpatterned MCs show three different slopes for the RH range studied, and as a consequence, they have three different RH sensitivity values in these regions. RH sensitivity (S) in these regions was estimated using the Eq. (5.2). Table 5.1 shows the estimated RH sensitivity along with the corresponding mass sensitivity in three regions shown in Fig. 5.3 (a).

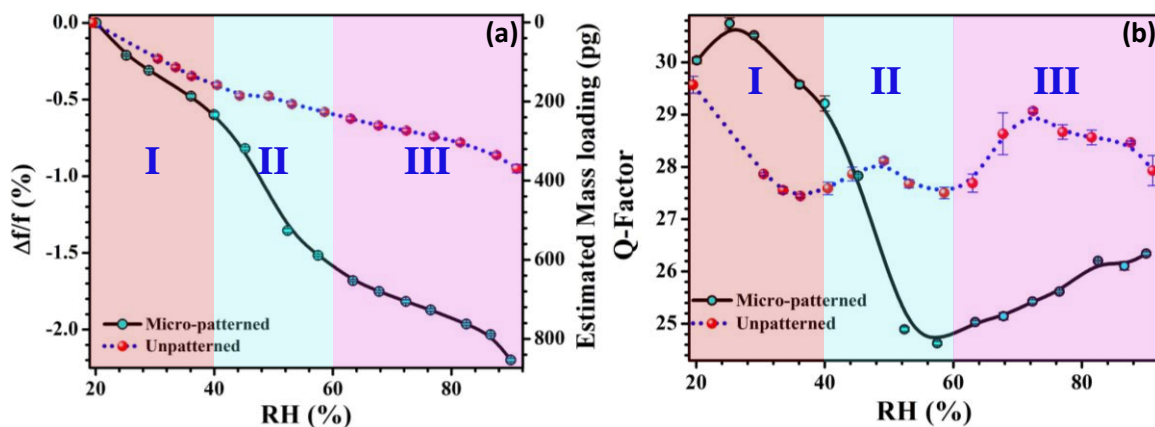


Figure 5.3. (a) Relative resonance frequency shift ($(\Delta f/f)\%$) and (b) Q-factor of typical micro-patterned and unpatterned MCs when RH is increased from 20 % to 90 %, respectively. From the shift in frequency, adsorbed mass is estimated using Eq. (1.21) and is shown on the right axis of (a). In these graphs, the error bar is of the size of the symbol used.

Table 5.1. RH and mass sensitivities of unpatterned and micro-patterned MCs in three different RH regions shown in Fig. 5.3 (a).

| MC Nomenclature | Sensitivity | | | | | |
|--------------------|------------------------------|--------|-------------------------------|--------|--------------------------------|--------|
| | Region - I 20% < RH < 40% | | Region - II 40% < RH < 60% | | Region - III 60% < RH < 90% | |
| | Hz/%RH | pg/%RH | Hz/%RH | pg/%RH | Hz/%RH | pg/%RH |
| Unpatterned MC | 3.82 | 7.28 | 1.42 | 3.34 | 1.82 | 3.73 |
| Micro-patterned MC | 5.73 | 11.23 | 10.45 | 21.39 | 3.11 | 6.9 |

The observed trend in the variation of RH sensitivity can be attributed to three different adsorption mechanisms. For low RH values (<40% - Region - I), water molecules adsorb on the exposed hydroxylated (Si – OH) SiO₂ surface following BET isotherm [36] and are similar for both unpatterned and micro-patterned MCs as shown in Fig. 5.4 (a).

Between 40 to 60% RH (Region - II), sensitivity in patterned MC is higher than the unpatterned MC, by an order. This indicates that, compared to the unpatterned surface, more water molecules are adsorbed on the micro-patterned surface. The resultant increase in added mass can be estimated theoretically, from the number of monolayers adsorbed on the patterned SiO₂ surface between these RH levels using Eq. 5.3. From this estimation, the total mass adsorbed on the patterned MC surface in the region - II was estimated to be ~ 21.89 pg. This value is significantly lower than the experimentally observed value which is around 600 pg between 40 and 60% RH. Since the size of micro-patterns in our experiment is much larger than the Kelvin radius, capillary condensation will not take place inside them at these RH levels [19], and therefore cannot explain the additional added mass. This is also confirmed by the lower hysteric behavior in our sensors when subjected to increasing and decreasing RH cycles (discussed later in section 5.3.4). It may be noted,

the difference in sensitivity values for unpatterned MCs shown in figure 5.1 (a) and 5.3 (a) in region-II is due to the presence of surface features on the former explaining its inferior hysteresis characteristics.

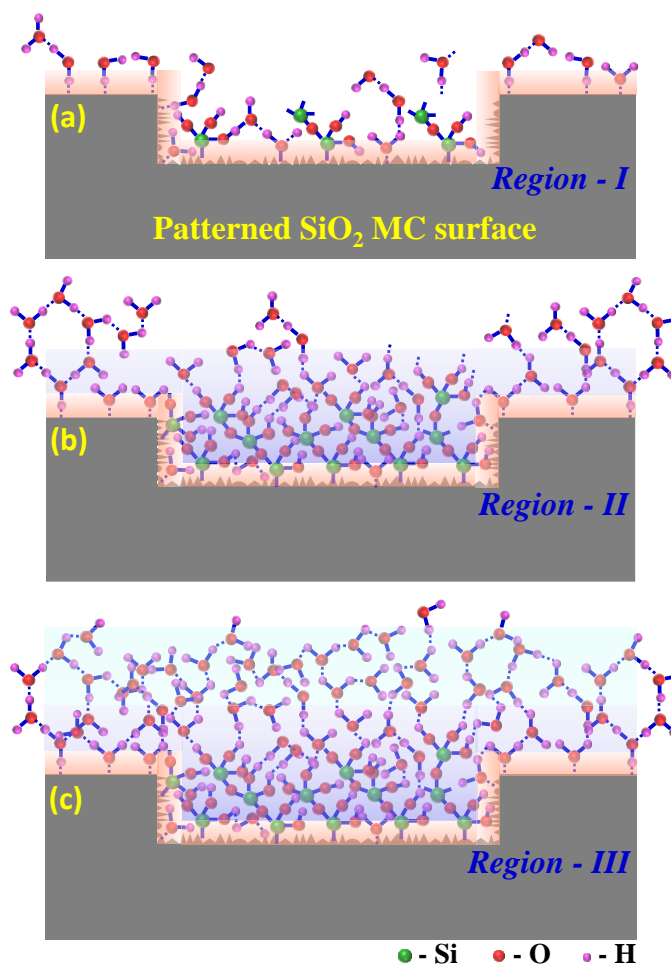


Figure 5.4. Mechanism of water adsorption on micro-patterned MC surface in three different regions shown in figure 5.2. (a) In Region – I (i.e. $20\% < RH < 40\%$), the water molecule adsorption occurs on exposed hydroxylated SiO₂ surface (b) In region – II ($40\% < RH < 60\%$), presence of gel-like structure of water molecules in the micro-patterned regions increases the effective uptake of water by several times and (c) In Region- III ($RH > 60\%$), closed water films are formed due to random hydrogen bonding between the water molecules as shown by light cyan region on top.

Interestingly, surface stress generated during adsorption of water molecules can also influence the resonance frequency of MCs. In the case of unpatterned MCs, this effect was found to be negligible [43]. However, Duan et al. [44] in a recent study showed that the surface patterns/surface morphology can enhance, reduce or annul the effect of surface stress on the resonance frequency of the MCs depending upon their surface inclination angle and Poisson's ratio of the material under consideration. It is to be noted that the presence of micro-patterns on the MC surface can act as stress concentration regions which can increase the differential surface stress and complement the frequency shift during adsorption of water molecules. The shift in the resonance frequency of MCs due to the presence of surface features and surface stress is given by the relation [44],

$$\frac{\Delta f}{f_0} \approx \frac{3(2\mu^s + \lambda^s)}{2E_s T(1 + g^2)^{3/2}} \left(1 - \frac{\nu}{1 - \nu} g^2\right)^2 \quad (5.5)$$

where, $E_s = E / (1 - \nu^2)$, E , μ^s , λ^s , and ν are the Young's Modulus, isotropic surface moduli, and Poisson's ratio of SiO₂, T is the thickness of the MC and g is the average surface slope. By approximating the square patterns as surfaces with inclination angle $\sim 85^\circ$ and by substituting the other values ($E = 73$ GPa, $\nu = 0.17$, $T = 0.98$ μm , $\mu^s = -2.6$ N/m, $\lambda^s = -2.7$ N/m) [44] in Eq. 5.5, the maximum $\Delta f/f$ for the entire RH range studied was estimated to be $\sim 0.1\%$. Hence this effect alone cannot explain the enhancement in RH sensitivity of micro-patterned MCs in region – II, by an order.

Recently, while studying the water adsorption on Si wafers, Chen et al. [45], proved that the Si wafers oxidized in water uptook significantly more water from humid air than the fully hydroxylated surface. They found that wafer aged in water formed *gel-like* structure (intermediate structure of water i.e. between self-associated stable '*ice-like*' and highly disordered '*liquid-like*' structures) which enhanced the water uptake

significantly and facilitated the growth of ‘ice-like’ structure on these surfaces. It is possible that the presence of micro-patterns in the present work, modifies the surface termination of the SiO₂ surface inside the micro-patterns, allowing the formation of *gel-like* layer during adsorption in Region – II (figure 5.4 (b)). However, any such transitions should increase the viscous damping and reduce the Q-factor value [46]. To verify the same, we have estimated the Q-factor values from the resonance spectrum and its variation with increasing RH for both unpatterned and micro-patterned MCs are shown in figure 5.3 (b). From this figure, it is evident that unlike unpatterned MC, a clear reduction in Q-value is seen in micro-patterned MC in the region - II. This is attributed to the gradual increase in the molecular moment within the water layer which maximizes the viscous damping. When RH is > 60%, Q - value starts recovering and is attributed to the reduction in mechanical strength of the *gel-like* water layer due to further adsorption of water molecules on its surface. In the case of unpatterned MCs, no such clear trends are seen in Q-factor values with increasing RH, which indicates a negligible change in resonator damping and thus the absence of *gel-like* layer. These results clearly demonstrate that the presence of micro-patterns facilitates the formation of multilayers of water molecules through the formation of *gel-like* structures inside the cavities in Region - II.

However, in Region - III i.e. when RH value is > 60%, sensitives in both unpatterned and micro-patterned MCs are comparable indicating adsorption mechanism is similar on both the surfaces. In this region, water adsorption takes place on already adsorbed water layers, which is dominated by hydrogen bonding between H₂O molecules and depends only on the concentration of water molecules in the chamber (figure 5.4 (c)). From the foregoing discussions, it is clear that micro-patterned SiO₂ MCs can be effectively used as RH sensors with enhanced sensitivity especially at higher RH values (i.e. in Region – II and III).

The effect of pattern depth on the RH sensitivity of the MCs was also investigated. Figure 5.5 shows the relative resonance frequency shift of the MCs with 15 nm (MC_{15}) and 75 nm (MC_{75}) deep surface micro-patterns. From this figure it is clear that in region I, the sensitivity of MC_{75} is higher by $\sim 51\%$ ($S_I = 8.66 \text{ Hz}/\%RH$) than MC_{15} and is attributed to the increase in effective surface area due to higher pattern depths. However, in region II, the sensitivity is nearly 49% ($S_{II} = 5.29 \text{ Hz}/\%RH$) lower for MCs with 75 nm deep patterns. Interestingly, in region III, after 70% RH, sensitivity of MC_{75} is greater than MC_{15} and the reason for which can be understood as follows. Deeper the micro-patterns, higher is their influence on the mechanical characteristics, especially the resonance frequency and Q-factor of the MCs. For example, a maximum of 2.7% and 15% reduction in base resonance frequency and Q-factor, respectively was observed for MCs with 75 nm deep micro-patterns compared to unpatterned MCs (refer chapter 3) which could play a major role in enhanced sensitivity in region III for MCs with 75 nm deep micro-patterns.

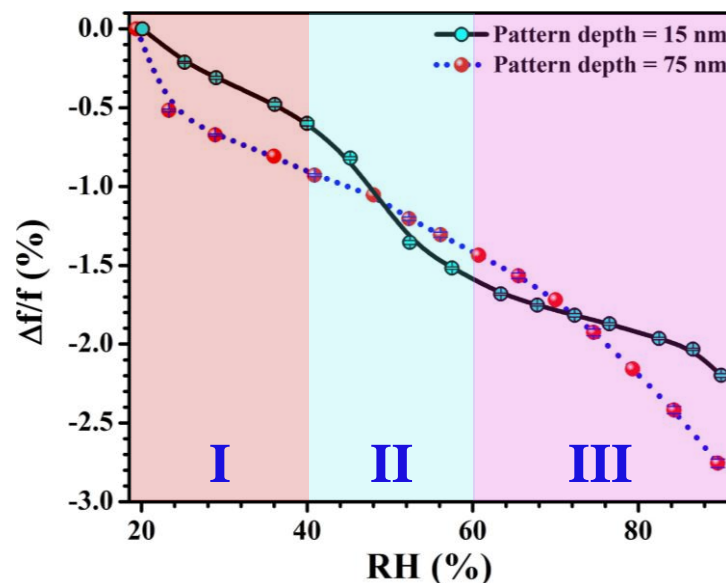


Figure 5.5. Relative resonance frequency shift ($(\Delta f/f)\%$) of 15 and 75 nm deep surface micro-patterned MCs when the RH is increased from 20% to 90%. In this graph, the error bar is of the size of the symbol used.

From the foregoing discussions, it is clear that the role of micro-pattern depth on RH sensitivity is more complex and warrants more systematic studies. Based on these inputs, it was decided to study the other sensor characteristics of MCs only on MCs with 15 nm deep micro-patterns.

5.3.2. Response/recovery times

Response/recovery time of the micro-patterned MCs was studied by recording the shift in peak amplitude at their resonance while RH inside the chamber was rapidly switched between 23% and 56%. Figure 5.6 (a) shows a typical sensor response as a function of time for two consecutive RH increase/decrease cycles. From this figure, the response and recovery times of the sensor were estimated and found to be ~20 s (figure 5.6 (b)) and ~30 s (figure 5.6 (c)), respectively. These values are much better than the values reported for polymer/metal oxide coated MCs [see table 5.2]. It may be noted, the actual response and recovery times of these sensors are significantly faster and are limited only by our experimental setup used for varying the RH. To validate the same, human respiratory monitoring experiments, where it is possible to achieve much faster RH variations readily, are undertaken on these devices.

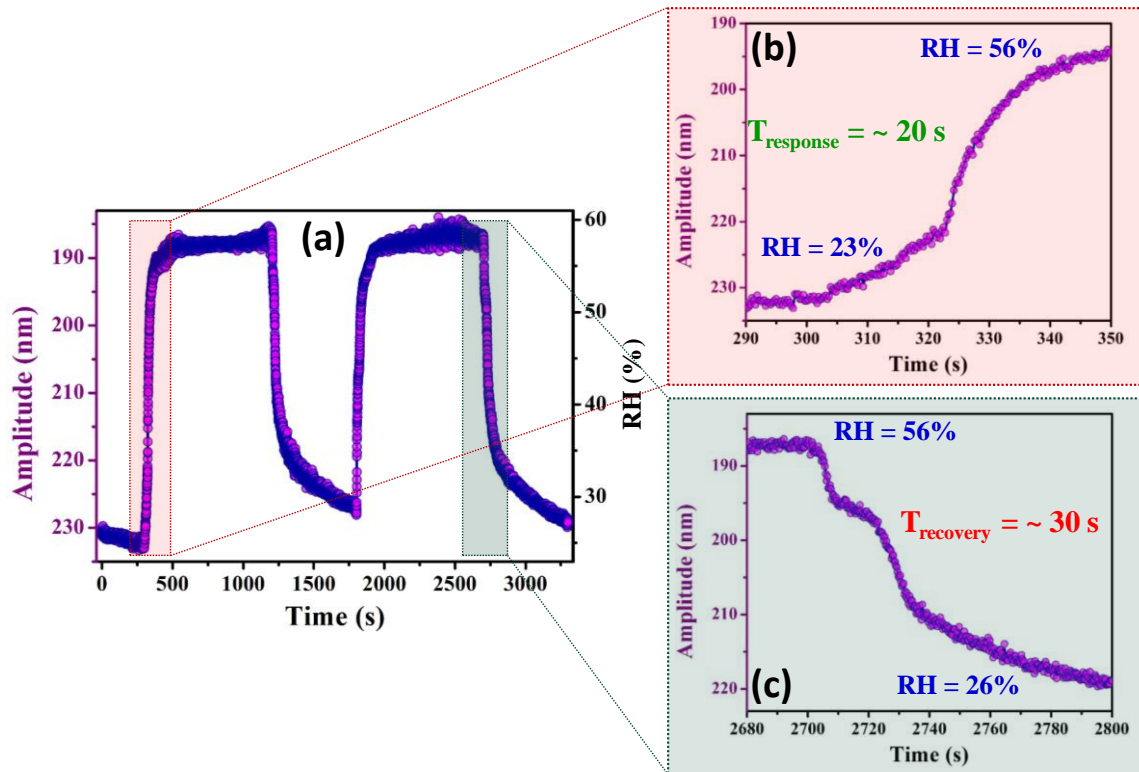


Figure 5.6. (a) The shift in peak amplitude at resonance as a function of time when RH is switched between $\sim 23\%$ and 57% , on a typical micro-patterned MC. From this data (b) response and (c) recovery times of these devices were estimated.

5.3.3. Human respiration monitoring

To further test the response time of our micro-patterned MCs, RH variation during the human respiratory cycles was monitored. Breath monitoring experiments were performed by exposing MCs to inhale and exhale breath cycles of a healthy adult (male) and by continuously measuring the shift in peak amplitude at the resonance of these devices using NVA. The complete details about the experimental setup used for this purpose is given in chapter 2.

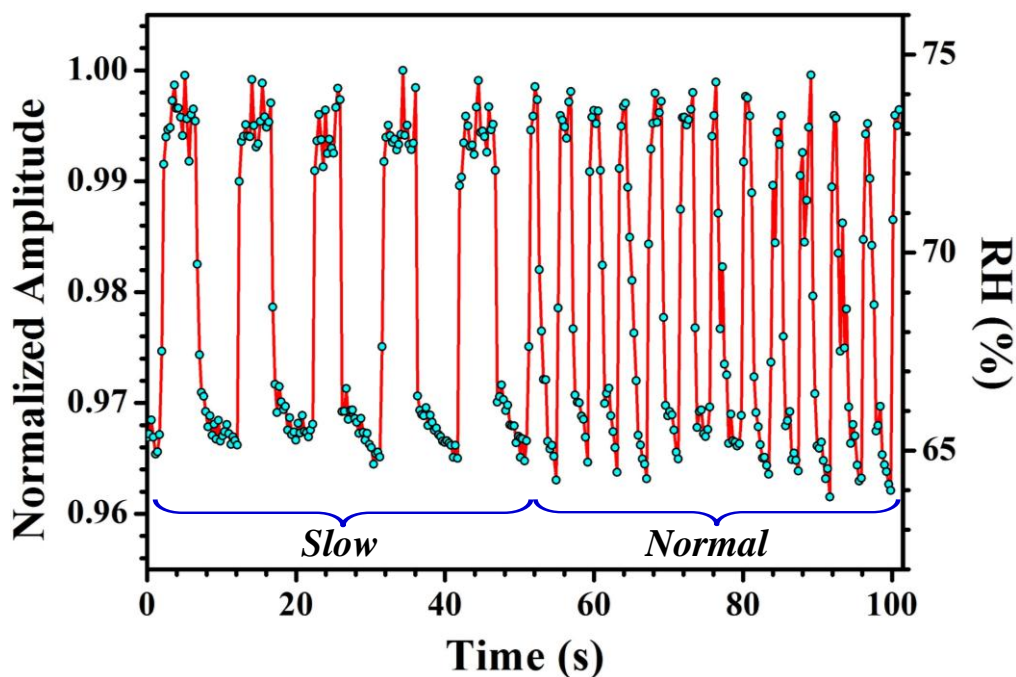


Figure 5.7. Response of a typical micro-patterned MC for slow and normal breathing inhale-exhale cycles of a healthy male adult. The right axis shows the variation in RH during breath cycles.

Figure 5.7 shows the recorded variation in peak amplitude at the resonance of a typical micro-patterned MC during slow (inhale-exhale cycle ~ 10 s) and normal (inhale-exhale cycle ~ 4 s) breathing cycles. From this figure, it is evident that the micro-patterned MC could efficiently follow the breathing cycle irrespective of breathing rate with a fast response and recovery times. Response and recovery times from this graph were estimated and found to be ~ 1 s. This value is significantly faster than the response times reported for nanomaterial coated MC based RH sensors (see table 5.2).

Interestingly, the commercial RH sensor used in the present work along with MCs could not follow the RH variation during the normal breathing cycles as shown in figure 5.8. From this figure, it is clear that RH sensitivity is completely lost during the normal breath cycles and the finer aspects of RH variation during the slow breath cycle are compromised. This clearly implies that the micro-patterned SiO_2 MCs as breath monitor

provides much superior characteristics in terms of response times and repeatability than the commercial RH sensors for detailed medical diagnosis.

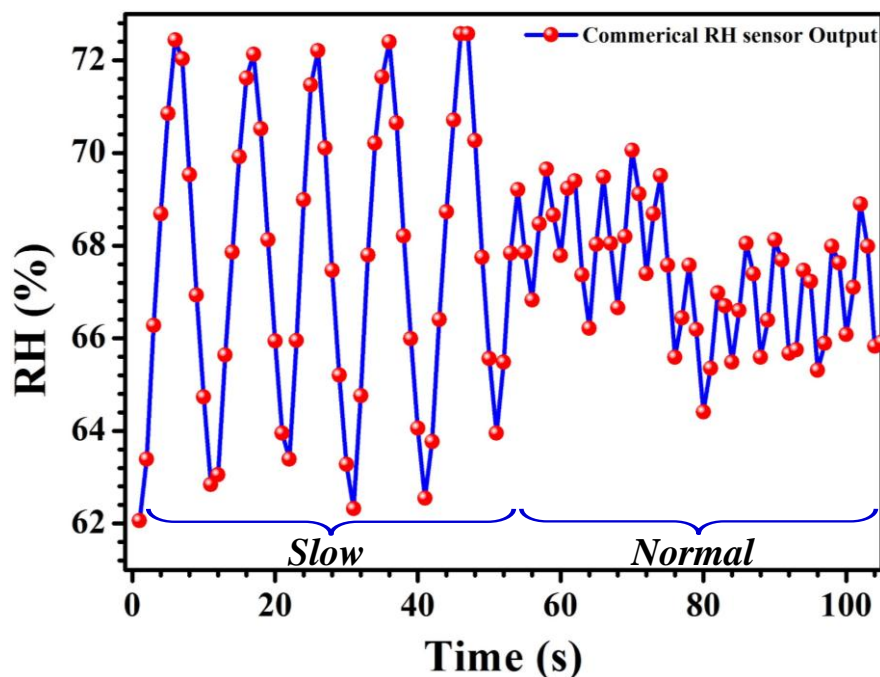


Figure 5.8. Response of commercial RH sensor which is placed inside the environmental chamber during the human breath monitoring experiment.

5.3.4. Hysteresis and Stability

To study the hysteresis response of micro-patterned MCs, experiments were performed by measuring the resonance frequency shift during repeated adsorption and desorption cycles. Figure 5.9 shows a typical sensor response during one RH increase and decrease cycles between 20% and 90%. From this figure, the hysteresis was estimated using Eq. 5.4 and found to be 2.5, 2.9, and 2.6 %RH for all the three regions, as defined in figure 5.3, respectively.

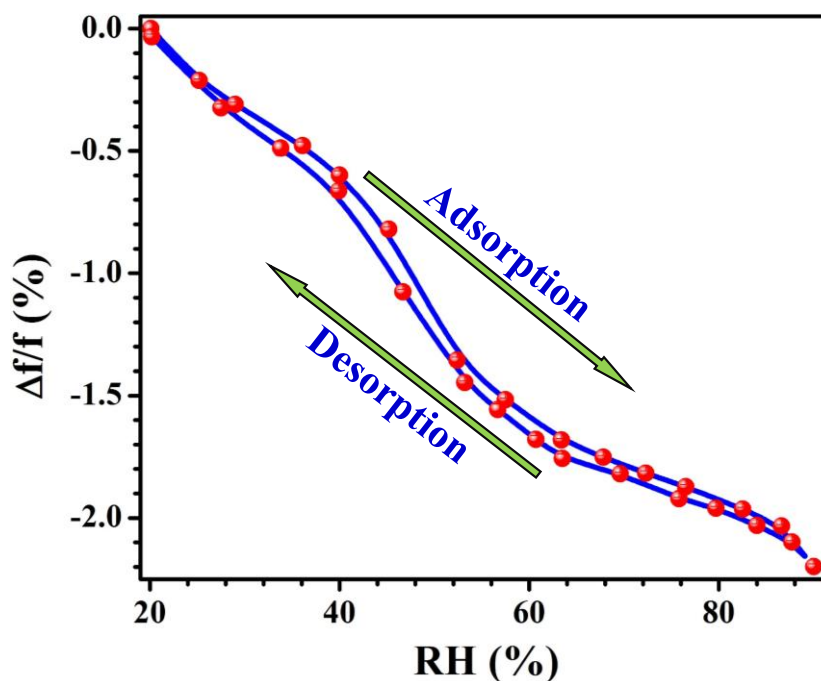


Figure 5.9. Relative resonance frequency shift of a typical surface micro-patterned MC during one RH increase and decrease cycle from 20% to 90%. From this figure, hysteresis value was estimated to be <3 %RH for all the three RH regions defined.

These values are significantly lower than the values reported for the MC based sensors with moisture sensitive nano-porous/nanostructured films on their surface (see table 5.2). For example, in mesoporous silica-coated MCs, Stassi et al. [33] reported a hysteresis value of 35 %RH which is between 30 to and 80% RH values. Similarly, J. Xu et al. [25] reported a hysteresis value of ~14 %RH in their piezoresistive MC based RH sensors coated with ZnO nano-rods/chitosan self-assembled monolayer. Higher hysteresis in these sensors is usually attributed to the capillary condensation of water molecules in nano-porous structures at higher RH levels which require additional energy for desorption and thus resulting in hysteresis. In contrast to this, the desorption activation energy for SiO₂ MC surface used in this study is significantly lower than any other known water adsorbing oxides [32]. Also, as mentioned earlier, the micro-patterns studied in the present work are significantly larger compared to the Kelvin radius, and no capillary condensation

is expected at higher RH levels, which facilitates faster desorption rates leading to better hysteresis value. Similarly, the presence of micro-patterns on the MC surface may modify the hydrophilicity of the SiO₂ surface, i.e. wettability, which may facilitate the rapid desorption of water molecules during RH decrease cycle, thereby reducing the hysteresis [47]. These results indicate that the introduction of micro-patterns on the MC surface enhances the RH sensitivity, without compromising the hysteresis.

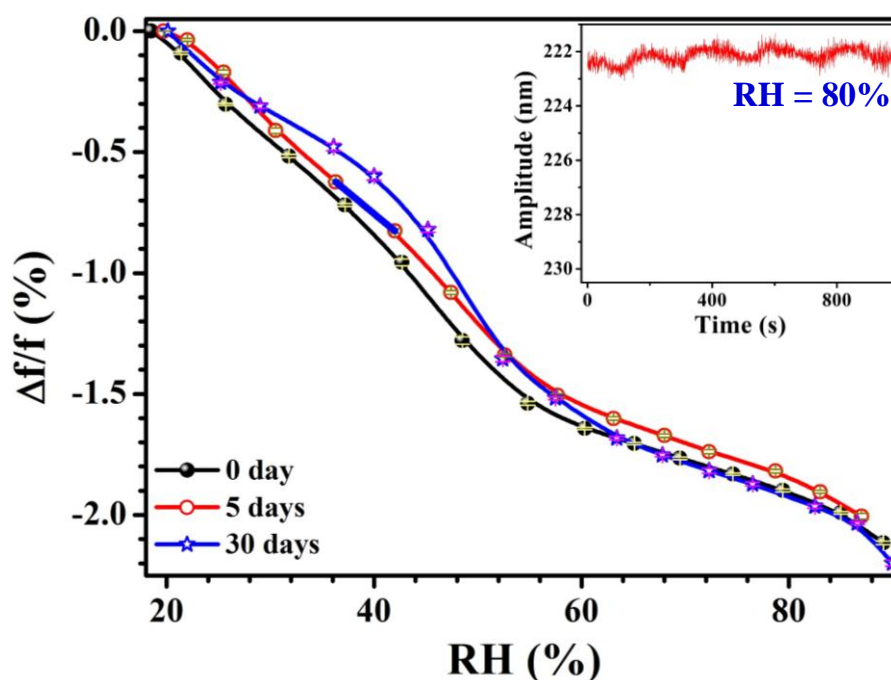


Figure 5.10. Relative resonance frequency shift of a typical surface micro-patterned MC when the RH is varied from 20% to 90 % after 1 day, 5 days, and 30 days of device fabrication. From this figure, the long term stability of the MCs and the degree of fluctuation was estimated to be < 5% for the entire RH range studied. Inset shows the variation in sensor response over a period of time when RH is maintained at 80%.

Stability of any RH sensor is another crucial parameter while considering them for practical applications. In the present work, the long-term stability of micro-patterned MCs was studied by exposing them in the open air for 30 days. Figure 5.10 shows the representative RH sensitivity of a typical sensor measured after 1 day, 5 days, and 30 days. Inset shows the variation in sensor response at a given RH over a time period of ~15

minutes. From this figure, it is evident that the frequency shift exhibit a small degree of fluctuation ($< 5\%$) over 30 days in the entire RH range studied. Similarly, it is clear that the variation in sensor output is < 2 nm over the entire time period indicating the good stability of these sensors. The results demonstrate that the micro-patterned MCs exhibit high stability and can be effectively used for real-time RH sensing applications.

5.4. Discussion

From the foregoing discussions, it is clear that micro-patterned MCs can be effectively used as RH sensors with high sensitivity, fast response times, and low hysteresis error, over a wide RH range. We now compare the performance of our sensor with various MC based sensors reported in the literature. MCs are usually coated with nanostructured materials to increase the effective surface area i.e. adsorption sites for water molecules. Table 5.2 shows the sensitivity, response time, hysteresis values reported in the literature for various nanomaterial coated sensors along with the results obtained in the present work. For comparison, the RH range, moisture sensing material used, and the mode of detection employed in these reports, are also included. From this table, it is evident that the presence of nanostructured materials such as porous alumina, graphene oxide, mesoporous silica, and zinc oxide nano-rods on the MC surface offers unprecedented RH sensitivity. However, enhancement in the sensitivity of these sensors is at the cost of a reduction in response time or an increase in hysteresis error. For example, in the case of Si MC coated with ZnO oxide nano-rods modified with Chitosan self-assembled monolayers (SAM), J. Xu et al. [25] reported much slower response/recovery times of 46 s / 167 s with a hysteresis value of 14 %RH (see table 5.2). Interestingly, when only ZnO nano-rods were coated, the hysteresis value was low (2%) but, sensitivity was found to be two orders lower than the chitosan SAM modified ones. Similar conclusions could be drawn from the work of S. Stassi et al. [33] on the mesoporous silica-coated Si MCs for

humidity detection where a hysteresis value of 35 %RH was reported. However, as an exception, in the case of Graphene oxide coated MCs, higher RH sensitivity is achieved over a wide dynamic range, with reasonable response time and hysteresis error [35]. Similarly, in the case of static measurements [9–11], RH sensitivities are reported either in nm/%RH or mV/%RH and cannot be compared directly with our results. However, it is interesting to note that the hysteresis values reported in static mode sensors are generally superior to dynamic mode sensors.

The slower response times and higher hysteresis values in nano sensors are generally attributed to the complicated desorption kinetics nanostructured materials used for RH sensing [34]. An alternative to this, in the present work, it is shown that the introduction of ordered micro-patterns on MC surface can enhance the RH sensitivity of MCs without compromising their response/recovery times and hysteresis. Moreover, these devices are made of single-layer SiO₂ (i.e. no metal coating), avoiding the temperature-induced bimetallic effect. We believe the RH sensitivity of micro-patterned MCs can be further improved by carefully modifying the physical dimensions of surface patterns. If piezo resistors are introduced at the fixed end of these devices, readout electronics can be readily incorporated on the same chip [10,25,34]. However, these sensors being uncoated, suffer from an intrinsic disadvantage of being non-selective. Lack of selectivity becomes acceptable in scenarios where higher sensitivity and fast response time are crucial simultaneously. For example, uncoated MCs can be effectively used in environments, where prior knowledge of the gas is already known, such as for accurate monitoring of cover gas in a nuclear reactor environment [48].

Table 5.2. Comparison of RH sensing characteristics of various nanostructured materials coated on MCs reported in the literature along with the present work.

| S.No | Reference | Device | Mode of detection | Sensitivity | RH range (%) | Response / Recovery time | Hysteresis (%RH) |
|------|--------------|--|-------------------|-----------------------|--------------|--------------------------|------------------|
| 1. | [11] | Poly-aniline (PANI) nanofibers functionalized SU-8 nano-composite MCs | Static | 64 μ V / 0.1 %RH | 28 – 93 | 8 s / 10 s | 1–2 |
| 2. | [9] | Si/ Polyaniline (PANI) MCs | Static | 39.37 - 177.58 nm/%RH | 20 – 70 | Not reported | 4.18 |
| 3. | [10] | CMOS MEMS piezoresistive humidity sensor – Polyimide coated piezoresistive MCs | Static | 7 mV/%RH | 20 – 80 | -/85 s | 3.2 |
| 4. | [49] | Porous anodic alumina MC | Dynamic | ~ 100 Hz/%RH | 10 – 22 | Not reported | Not reported |
| 5. | [33] | Mesoporous silica-coated Si MCs | Dynamic | 0.009 - 0.026 %/%RH | 5 – 80 | Not reported | 35 |
| 6. | [25,34] | Si MCs with ZnO nano-rods/Chitosan-SAMs | Dynamic | 3.35 - 15 Hz/%RH | 30 – 70 | 46 s / 167 s | 14 |
| 7. | [35] | Interdigital transducers (IDTs) excited AlN/Si MCs coated with Graphene oxide | Dynamic | 84.41 Hz/%RH | 10 – 90 | 10 s / - | <3 |
| 8. | [25] | ZnO nanorods coated piezoresistive Si MCs | Dynamic | 0.72 Hz/%RH | 30 – 80 | Not reported | 2 |
| 9. | Present work | Controlled micro-patterned SiO ₂ MCs | Dynamic | 3.11 - 10.45 Hz/%RH | 20 – 90 | 1 s | < 3 |

5.5. Summary

It is shown that as-fabricated SiO₂ MCs can be effectively used as RH sensors in dynamic mode, without any functionalization, with maximum sensitivity and resolution of 4.08 Hz/%RH and < 1% RH, respectively. It is also shown that, the introduction of controlled micro-patterns on the MC surface provides a simple and efficient way to enhance the sensitivity of MC based sensors without compromising other sensor characteristics such as response and recovery times. Micro-patterned sensors were found to have an unprecedented RH sensitivity (10.45 Hz/% RH), very low hysteresis value (< 3 %RH), fast response/recovery times (~1 s) and excellent stability (variation <5%) over a wide range of RH from 20% to 90%. The enhancement in RH sensitivity in the case of micro-patterned MCs is explained with a model, where it is shown that the formation of *gel-like* water layer inside the cavities facilitates enhanced uptake of water molecules. From the comparison with the studies in the literature it is found that the nanostructured material coated MCs offer enhanced sensitivity, but at the cost of reduction in response/recovery time or increase in hysteresis error which can be attributed to their complicated desorption kinetics. Finally, the micro-patterned MCs are demonstrated for human breath monitoring with excellent response and recovery times during both slow and fast breath cycles.

5.6. References

- [1] H. Farahani, R. Wagiran, M.N. Hamidon, Humidity sensors principle, mechanism, and fabrication technologies: A comprehensive review, 2014.
- [2] Z. Chen, C. Lu, Humidity Sensors: A Review of Materials and Mechanisms, Sens. Lett. 3 (2005) 274–295.
- [3] G. Korotcenkov, Handbook of Humidity Measurement, 2020.
- [4] C.Y. Lee, G. Bin Lee, Humidity sensors: A review, Sens. Lett. 3 (2005) 1–15.

- [5] Y. Yao, X. Chen, H. Guo, Z. Wu, X. Li, Humidity sensing behaviors of graphene oxide-silicon bi-layer flexible structure, *Sensors Actuators, B Chem.* 161 (2012) 1053–1058.
- [6] U. Mogera, A.A. Sagade, S.J. George, G.U. Kulkarni, Ultrafast response humidity sensor using supramolecular nanofibre and its application in monitoring breath humidity and flow, *Sci. Rep.* 4 (2014) 1–9.
- [7] S. Borini, R. White, D. Wei, M. Astley, S. Haque, E. Spigone, N. Harris, J. Kivioja, T. Ryhänen, Ultrafast graphene oxide humidity sensors, *ACS Nano.* 7 (2013) 11166–11173.
- [8] J. Huang, Q.-A. Huang, *Micromachined Humidity Sensors*, (2018) 787–816.
- [9] C. Steffens, A. Manzoli, F.L. Leite, O. Fatibello, P.S.P. Herrmann, Atomic force microscope microcantilevers used as sensors for monitoring humidity, *Microelectron. Eng.* 113 (2014) 80–85.
- [10] J.Q. Huang, F. Li, M. Zhao, K. Wang, A surface micromachined CMOS MEMS humidity sensor, *Micromachines.* 6 (2015) 1569–1576.
- [11] S.J. Patil, A. Adhikari, M.S. Baghini, V.R. Rao, An ultra-sensitive piezoresistive polymer nano-composite microcantilever platform for humidity and soil moisture detection, *Sensors Actuators, B Chem.* 203 (2014) 165–173.
- [12] G. Korotchenkov, V. Brynzari, S. Dmitriev, Electrical behavior of SnO₂ thin films in humid atmosphere, *Sensors Actuators, B Chem.* 54 (1999) 197–201.
- [13] T. Kuse, S. Takahashi, Transitional behavior of tin oxide semiconductor under a step-like humidity change, *Sensors Actuators, B Chem.* 67 (2000) 36–42.
- [14] M. Viviani, M.T. Buscaglia, V. Buscaglia, M. Leoni, P. Nanni, Barium perovskites as humidity sensing materials, *J. Eur. Ceram. Soc.* 21 (2001) 1981–1984.

- [15] H. Zhao, T. Zhang, R. Qi, J. Dai, S. Liu, T. Fei, G. Lu, Organic-inorganic hybrid materials based on mesoporous silica derivatives for humidity sensing, *Sensors Actuators, B Chem.* 248 (2017) 803–811.
- [16] K.P. Yoo, L.T. Lim, N.K. Min, M.J. Lee, C.J. Lee, C.W. Park, Novel resistive-type humidity sensor based on multiwall carbon nanotube/polyimide composite films, *Sensors Actuators, B Chem.* 145 (2010) 120–125.
- [17] Y. Zhang, K. Yu, D. Jiang, Z. Zhu, H. Geng, L. Luo, Zinc oxide nanorod and nanowire for humidity sensor, *Appl. Surf. Sci.* 242 (2005) 212–217.
- [18] D. Zhang, J. Tong, B. Xia, Humidity-sensing properties of chemically reduced graphene oxide/polymer nanocomposite film sensor based on layer-by-layer nano self-assembly, *Sensors Actuators, B Chem.* 197 (2014) 66–72.
- [19] Y. Wang, S. Park, J.T.W. Yeow, A. Langner, F. Müller, A capacitive humidity sensor based on ordered macroporous silicon with thin film surface coating, *Sensors Actuators, B Chem.* 149 (2010) 136–142.
- [20] D. Zhang, H. Chang, P. Li, R. Liu, Q. Xue, Fabrication and characterization of an ultrasensitive humidity sensor based on metal oxide/graphene hybrid nanocomposite, *Sensors Actuators, B Chem.* 225 (2016) 233–240.
- [21] D. Zhang, X. Zong, Z. Wu, Y. Zhang, Hierarchical Self-Assembled SnS₂ Nanoflower/Zn₂SnO₄ Hollow Sphere Nanohybrid for Humidity-Sensing Applications, *ACS Appl. Mater. Interfaces.* 10 (2018) 32631–32639.
- [22] S. Mehrabani, P. Kwong, M. Gupta, A.M. Armani, Hybrid microcavity humidity sensor, *Appl. Phys. Lett.* 102 (2013).
- [23] P. Kapa, L. Pan, A. Bandhanadham, J. Fang, K. Varahramyan, W. Davis, H.F. Ji, Moisture measurement using porous aluminum oxide coated microcantilevers, *Sensors Actuators, B Chem.* 134 (2008) 390–395.

- [24] J. Xu, M. Bertke, X. Li, A. Setiono, M. Fahrbach, A. Schmidt, E. Peiner, Silicon Microcantilevers with ZnO Nanorods/Chitosan-SAMs Hybrids on Its Back Surface for Humidity Sensing, *Proceedings. 2* (2018) 838.
- [25] J. Xu, M. Bertke, H.S. Wasisto, E. Peiner, Piezoresistive microcantilevers for humidity sensing, *J. Micromechanics Microengineering. 29* (2019) 053003.
- [26] C.A. Grimes, D. Kouzoudis, E.C. Dickey, D. Qian, M.A. Anderson, R. Shahidain, M. Lindsey, L. Green, Magnetoelastic sensors in combination with nanometer-scale honeycombed thin film ceramic TiO₂ for remote query measurement of humidity, *J. Appl. Phys. 87* (2000) 5341–5343.
- [27] Z. Yuan, H. Tai, Z. Ye, C. Liu, G. Xie, X. Du, Y. Jiang, Novel highly sensitive QCM humidity sensor with low hysteresis based on graphene oxide (GO)/poly(ethyleneimine) layered film, *Sensors Actuators, B Chem. 234* (2016) 145–154.
- [28] H.S. Hong, G.S. Chung, Humidity sensing characteristics of Ga-doped zinc oxide film grown on a polycrystalline AlN thin film based on a surface acoustic wave, *Sensors Actuators, B Chem. 150* (2010) 681–685.
- [29] D.R. Southworth, L.M. Bellan, Y. Linzon, H.G. Craighead, J.M. Parpia, Stress-based vapor sensing using resonant microbridges, *Appl. Phys. Lett. 96* (2010).
- [30] Z. Shen, W.Y. Shih, W.H. Shih, Self-exciting, self-sensing PbZr_{0.53}Ti_{0.47}O₃/SiO₂ piezoelectric microcantilevers with femtogram/ Hertz sensitivity, *Appl. Phys. Lett. 89* (2006) 2004–2007.
- [31] S. Balasubramanian, K. Prabakar, Fabrication and characterization of SiO₂ microcantilevers by direct laser writing and wet chemical etching methods for relative humidity sensing, *Microelectron. Eng. 212* (2019) 61–69.

- [32] P. Raghu, C. Yim, F. Shadman, E. Shero, Susceptibility of SiO₂, ZrO₂, and HfO₂ dielectrics to moisture contamination, *AIChE J.* 50 (2004) 1881–1888.
- [33] S. Stassi, V. Cauda, S. Fiorilli, C. Ricciardi, Surface area enhancement by mesoporous silica deposition on microcantilever sensors for small molecule detection, *J. Mater. Chem. C.* 3 (2015) 12507–12513.
- [34] J. Xu, M. Bertke, X. Li, H. Mu, H. Zhou, F. Yu, G. Hamdana, A. Schmidt, H. Bremers, E. Peiner, Fabrication of ZnO nanorods and Chitosan@ZnO nanorods on MEMS piezoresistive self-actuating silicon microcantilever for humidity sensing, *Sensors Actuators, B Chem.* 273 (2018) 276–287.
- [35] X. Le, L. Peng, J. Pang, Z. Xu, C. Gao, J. Xie, Humidity sensors based on AlN microcantilevers excited at high-order resonant modes and sensing layers of uniform graphene oxide, *Sensors Actuators, B Chem.* 283 (2019) 198–206.
- [36] D.B. Asay, S.H. Kim, Evolution of the adsorbed water layer structure on silicon oxide at room temperature, *J. Phys. Chem. B.* 109 (2005) 16760–16763.
- [37] G.Y. Chen, T. Thundat, E.A. Wachter, R.J. Warmack, Adsorption-induced surface stress and its effects on resonance frequency of microcantilevers, *J. Appl. Phys.* 77 (1995) 3618–3622.
- [38] H.S. Wasisto, S. Merzsch, A. Waag, E. Uhde, T. Salthammer, E. Peiner, Airborne engineered nanoparticle mass sensor based on a silicon resonant cantilever, *Sensors Actuators, B Chem.* 180 (2013) 77–89.
- [39] K. Lakshmoji, K. Prabakar, S. Tripura Sundari, J. Jayapandian, A.K. Tyagi, C.S. Sundar, Origin of bending in uncoated microcantilever - Surface topography?, *Appl. Phys. Lett.* 104 (2014) 2–5.

- [40] J. Mertens, M. Calleja, D. Ramos, A. Tarín, J. Tamayo, Role of the gold film nanostructure on the nanomechanical response of microcantilever sensors, *J. Appl. Phys.* 101 (2007).
- [41] M. Raghuramaiah, K. Prabakar, S. Tripura Sundari, J. Jayapandian, Role of surface morphology on desorption kinetics of water molecules from uncoated silicon microcantilever, *Sensors Actuators, B Chem.* 223 (2016) 35–39.
- [42] M.Q. Liu, C. Wang, N.Y. Kim, High-sensitivity and low-hysteresis porous mim-type capacitive humidity sensor using functional polymer mixed with TiO₂ microparticles, *Sensors (Switzerland)*. 17 (2017).
- [43] S. Balasubramanian, K. Prabakar, Aditi, R. Mukhiya, S. Tripura Sundari, Effect of biaxial curvature on the resonance frequency of uncoated microcantilevers, *Sensors Actuators, A Phys.* 304 (2020) 111857.
- [44] H. Duan, Y. Xue, X. Yi, Vibration of cantilevers with rough surfaces, *Acta Mech. Solida Sin.* 22 (2009) 550–554.
- [45] L. Chen, D. Ngo, J. Luo, Y. Gong, C. Xiao, X. He, B. Yu, L. Qian, S.H. Kim, Dependence of water adsorption on the surface structure of silicon wafers aged under different environmental conditions, *Phys. Chem. Chem. Phys.* 21 (2019) 26041–26048.
- [46] L.Q. Nguyen, P.E. Larsen, T. Larsen, S.B. Goswami, L.G. Villanueva, A. Boisen, S.S. Keller, Pyrolytic carbon resonators for micromechanical thermal analysis, *Microsystems Nanoeng.* 5 (2019).
- [47] M. Björkqvist, J. Paski, J. Salonen, V.P. Lehto, Studies on hysteresis reduction in thermally carbonized porous silicon humidity sensor, *IEEE Sens. J.* 6 (2006) 542–546.

- [48] I. Dufour, F. Josse, S.M. Heinrich, C. Lucat, C. Ayela, F. Ménil, O. Brand, Unconventional uses of microcantilevers as chemical sensors in gas and liquid media, *Sensors Actuators, B Chem.* 170 (2012) 115–121.
- [49] O. Boytsova, A. Klimenko, V. Lebedev, A. Lukashin, A. Eliseev, Nanomechanical humidity detection through porous alumina cantilevers, *Beilstein J. Nanotechnol.* 6 (2015) 1332–1337.



Homi Bhabha National Institute

Report of Ph.D. Viva-Voce

Board of Studies in Physical Sciences

A. General Details:

1. **Name of the Constituent Institution:** Indira Gandhi Centre for Atomic Research

2. **Name of the Student:** Balasubramanian. S

3. **Enrolment Number:** PHYS02201504018

4. **Date of Enrolment in HBNI:** 01/08/2015

5. **Date of Submission of Thesis:** 10/09/2020

6. **Title of the Thesis:** Fabrication and characterization of SiO₂ microcantilevers for Relative Humidity sensing

7. **Number of Doctoral Committee Meetings held with respective dates:** 5

| Review Period | Date | Review Period | Date |
|--|------------|-----------------------------|------------|
| 1. 01/08/2015 to 31/07/2016 | 31/08/2016 | 2. 01/08/2016 to 31/07/2017 | 28/08/2017 |
| 3. 01/08/2017 to 31/07/2018 | 06/08/2018 | 4. 01/08/2018 to 25/07/2019 | 25/07/2019 |
| 5. 26/07/2019 to 28/05/2020 (pre-synopsis – viva) | 28/05/2020 | | |

8. **Name and Affiliation of the Thesis Examiner 1:**

Dr. Isabelle Dufour, Professor of Electrical Engineering, Leader of the Organic Electronics and Microsystems Research Group, University of Bordeaux, France.

Recommendations of the Examiner 1 (Thesis Evaluation) - Accepted after revisions.

9. **Name and Affiliation of the Thesis Examiner 2:**

Prof. K. N. Bhat, Centre for Nano Science and Engineering, Indian Institute of Science, Bangalore -560012.

Recommendations of the Examiner 2 (Thesis Evaluation): Accepted.

B. Record of the Viva-Voce Examination

1. Date of Viva Voce Examination: 15 December 2020 at 14:00 Hrs

2. Name and affiliation of External Examiner:

Dr. Isabelle Dufour, Professor of Electrical Engineering, Leader of the Organic Electronics and Microsystems Research Group, University of Bordeaux, France.

3. Whether there were other experts / faculty/students present?

Yes (Soft copy of the attendance sheet attached)

4. Recommendations for the award of the Ph.D. degree: Recommended / ~~Not Recommended~~

(If Recommended, give summary of main findings and overall quality of thesis)

(If Not Recommended, give reasons for not recommending and guidelines to be communicated by Convener of the Doctoral committee to the student for further work)

In the present thesis, Mr. Balasubramanian has fabricated SiO₂ microcantilevers (MCs) of various dimensions using direct laser writer and wet chemical etching methods and tested them for relative humidity (RH) sensing. He has extensively characterized the released MCs using optical profiler, NVA and LDV. Ahead of RH sensing studies, he has addressed certain important aspects of MC based sensors, such as the effect of biaxial curvature on the resonance frequency of the MCs and high-temperature annealing on the residual stress evolution. Finally, as fabricated SiO₂ MCs are tested for RH sensing and an innovative method to enhance the RH sensitivity of these devices by introducing controlled surface micropatterns on their surface is proposed. Micropatterned devices were also successfully put to use for human breath monitoring study/application.

The work presented in the thesis is inter-disciplinary in nature and is commendable. Thesis is divided into six chapters and is well written. In chapter-1, a general introduction to MC based sensors, their working modes, literature survey on the influence of surface modification of MCs and the motivation of the thesis are clearly presented. Followed by this, details about various experimental setups used for MC fabrication and characterization along with FEM simulation details are given in chapter -2. In chapter -3, details about various microfabrication process optimizations carried for the successful release of SiO₂ MCs are presented. An effective method to avoid stiction in SiO₂ MCs while releasing them by wet chemicals, is proposed. It is shown that introduction of a sharp convex tip at the free end of the MC along with a post-etch rinsing in boiling DI water, reduces the stiction substantially, even in the longest MCs. He has also estimated the residual stress in SiO₂ film from MC bending measurements and studied the role of undercutting on the measured resonance frequency.

As a precursor to RH sensing studies, Mr. Balasubramanian has studied the effect of biaxial curvature on the resonance frequency of SiO₂ MCs, in chapter -4. Major findings from this chapter are: 1) Presence of biaxial curvature in as-fabricated MCs directly increases their stiffness when their Width to Length ratio is between 0.16 and 0.35. Nonlinear stiffening and clamping geometric effect present in MCs are shown to be the reasons for the observed positive frequency shift and compared to principal curvature, transverse curvature seems to play a dominant role on the frequency shift. 2) Post-release high-temperature annealing of SiO₂ MCs increases their curvature and is attributed to the onset of plastic deformation of these structures at elevated temperatures.

In chapter-5, for RH sensing studies, Mr. Balasubramanian has indigenously designed an air-tight chamber and studied the RH sensitivity of SiO₂ MCs in the RH range of 20 to 80%. Main findings from this chapter are, 1) As fabricated SiO₂ MCs can be effectively used as RH sensors, in dynamic mode, without any functionalization, with maximum sensitivity and resolution of 4.08 Hz/%RH and < 1% RH, respectively. 2) Introduction of controlled micro-patterns on the MC surface provides a simple and efficient way to enhance the sensitivity of MC based sensors without compromising other sensor characteristics such as response and recovery times. 3) Finally, micro-patterned MCs are demonstrated for human breath monitoring with excellent response and recovery times during both slow and fast breath cycles.

Mr. Balasubramanian has incorporated all the changes suggested by thesis examiners and submitted the revised thesis along with list of corrections. Overall quality of thesis is good and it is recommended for the award of Ph.D. degree in Physics by HBNI.

5. Attendance at Viva Voce (Doctoral Committee, External Examiner, others):

| Sr No | Composition | Name | Attended in person or through video; if in person, signature |
|--------------------------------|----------------------------------|--|--|
| 1. | Chairman | Dr. M. Kamruddin | <i>M Kamruddin</i> 15/12/2020 |
| 2. | Convener (Guide) | Dr. K. Prabakar | <i>K Prabakar</i> 15/12/20 |
| 3. | Co-Guide/External Guide (if any) | --- | |
| 4. | External Examiner | Prof. Isabelle Dufour, University of Bordeaux, France. | By VC <i>P. Raji</i> (Dean, IPS) |
| 5. | Member | Dr. T. R. Ravindran | <i>T R Ravindran</i> |
| 6. | Member | Dr. V. Jayaraman | <i>V Jayaraman</i> |
| 7. | The Technology Adviser, if any | Sri. R. Baskaran | <i>R Baskaran</i> 15/12/20 |
| Others: list in separate sheet | | | |
| 8. | | | |
| 9. | | | |

K Prabakar 15/12/20
(Convener, Viva Voce Board)

Student answered all qns asked by Viva examiners, DC members and other participants. Viva committee recommended for the award of Ph.D.

P. Raji 15/12/2020
(Dean, P.S.)

Thesis Highlight

Name of the Student: **Balasubramanian. S**

Name of CI: **Indira Gandhi Centre for Atomic Research Enrolment No.: PHYS02201504018**

Thesis Title: **Fabrication and characterization of SiO₂ microcantilevers for Relative Humidity sensing**

Discipline: **Physical Sciences** Sub-Area of Discipline: **Experimental Microcantilever based sensors**

Date of viva voce: **15/12/2020**

In the present work, SiO₂ MCs of various dimensions ((length (L) = 50 – 330 μm; width (W) = 37 μm; thickness (T) = 0.98 μm)) were fabricated using mask-less Direct Laser writer and wet chemical etching methods (Fig. 1a). An effective two-step process to avoid stiction in SiO₂ MCs released by TMAHw solution is proposed. The released MCs were thoroughly characterized using 3D optical microscope and Nano Vibration Analyzer (NVA). From initial bending measurements on MCs, gradient residual stress in SiO₂ film was estimated and found to be 15.14 (± 0.32) MPa. Further, the experimentally measured resonance frequency values were compared with analytically estimated ones from classical beam theory and the discrepancy in resonance frequency between them is explained on the basis of the increase in the effective length of MCs due to undercutting. As a prelude to RH sensing studies, the effect of i) inherent biaxial curvature on the resonance frequency and ii) high-temperature post-release annealing on the residual stress evolution of SiO₂ MCs, are studied. It is shown experimentally that the presence of biaxial curvature in SiO₂ MCs directly increases their resonance frequency when their Width to Length ratio (W/L) is between 0.16 and 0.35. Similarly, post-release high-temperature annealing (800°C and 1000°C in O₂ and N₂) studies on SiO₂ MCs revealed that these devices undergo an irreversible increase in static deflection with annealing. Based on these studies, it was decided to use as-fabricated SiO₂ MCs with W/L < 0.16, in dynamic mode, for RH sensing studies.

RH sensing experiments were performed on as-fabricated SiO₂ MCs by measuring the shift in their resonance frequency using NVA while RH is varied between 20 and 90%. These experiments revealed that the as-fabricated SiO₂ MCs had a maximum sensitivity and resolution of 4 Hz/%RH and < 1% RH, respectively. To increase the RH sensitivity, an innovative method by introducing controlled micro-patterns (4 x 4x0.015 μm³) on the MC surface without compromising their response/recovery times and hysteresis is proposed. Micro-patterned MCs exhibited an unprecedented RH sensitivity (10.45 Hz/%RH) (see Fig. 1b), ultrafast response/recovery times (~ 1 s) and outstanding stability (variation < 5%) along with low hysteresis error (< 3%RH). Finally, real-time monitoring of human respiration during fast and slow cycles of healthy male adult using micro-patterned MCs is demonstrated as shown in Fig. 1c.

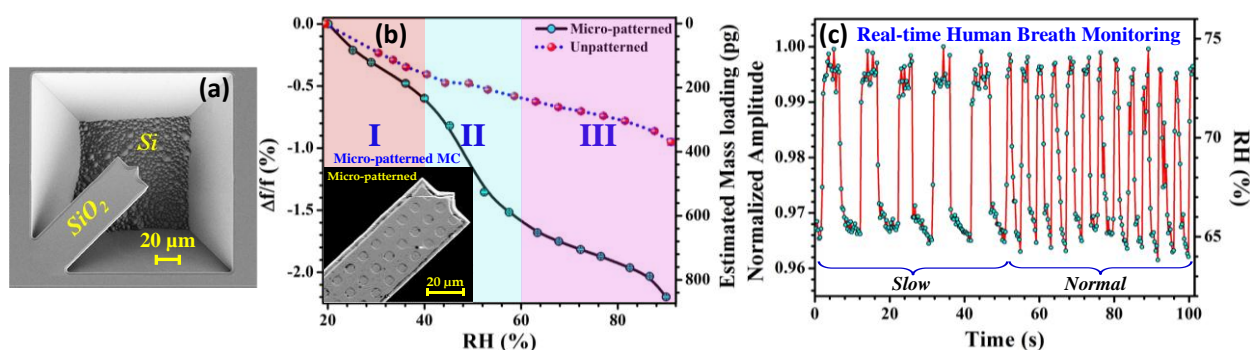


Fig. 1. (a) Typical FESEM image of the released as-fabricated SiO₂ MC. (b) Relative resonance frequency shift (($\Delta f/f$)%) of typical micro-patterned and unpatterned MCs when RH is increased from 20 % to 90 %, respectively. The inset shows the FESEM image of the free-end of a typical surface micro-patterned SiO₂ MC. (c) Response of a typical micro-patterned MC for slow and normal breathing inhale-exhale cycles of a healthy male adult. The right axis shows the independent RH measurement using a commercial RH sensor.